وزارة التعليم العالي والبحث العلمي
Ministère de l'Enseignement Supérieur et de la Recherche Scientifique

جامعة البليدة 1
UNIVERSITE BLIDA 1

University of Blida 1 Saad Dahled
Institute of Aeronautics and Space Studies
Aeronautical Construction Department

End of Study Thesis

In order to obtain the diploma of

Master's Degree in Aeronautics

Specialty: Aeronautical Structures

Subject

Analytical solutions for bending and buckling of an advanced FGM composite plate reinforced by graphene nano-platelets.

Proposed and supervised by :

Dr. MAHI Amale

Submitted by :

Mr. KADRI Mohamed

Co-supervised by :

Dr. HASSAINE Abdellah

2023 / 2024

ABSTRACT

To meet regulatory and economic requirements, the aerospace, naval, and civil engineering industries are constantly looking for structures that are both strong and lightweight. The rapid advances in nanoscience and nanotechnology have gone a long way towards meeting this demand. Theoretical and experimental studies are converging on the development of new high-tech composites, such as FGMs (Functionally Graded Materials) and advanced composites, reinforced with graphene nano-platelets. These nano-platelets are proving promising, offering optimized mechanical, thermal, and electrical properties, and electrical properties with significant weight savings.

This study aims to contribute to this development by examining the influence of graphene nano-platelet reinforcement on the bending and buckling response of an advanced composite plate. An adapted high-order shear deformation theory will be used to carry out this parametric study.

Keywords: bending, buckling, analytical method, advanced composites, graphene nano-platelets.

ملخص

تبحث صناعات الطيران وبناء السفن وصناعة السيارات والهندسة المدنية باستمرار عن هياكل قوية وخفيفة الوزن لتلبية المتطلبات التنظيمية والاقتصادية. وقد تم تلبية الكثير من هذا الطلب من خلال التقدم السريع في علوم النانو وتكنولوجيا النانو. وتركز الأبحاث التجريبية والنظرية على إنشاء مركبات جديدة عالية التقنية مثل المواد المتدرجة الوظيفية والمركبات المتقدمة المعززة بصفائح نانوية من الجرافين.
وتعد هذه الصفيحات النانوية واعدة لأنها توفر خصائص ميكانيكية وحرارية وكهربائية محسّنة مع توفير كبير في الوزن.
تهدف هذه الدراسة إلى المساهمة في هذا التطور من خلال فحص تأثير تقوية صفائح الجرافين النانوية على استجابة الانحناء والالتواء للوحة المركبة المتقدمة. لإجراء هذه الدراسة الوسيطية، سيتم استخدام نظرية تشوه عالي الدرجة للقص.

الكلمات المفتاحية: الانحناء، الالتواء، طريقة تحليلية، مركبات متقدمة، صفائح الجرافين النانوية.

Résumé

Les industries aérospatiale, navale, automobile et du génie civil recherchent constamment des structures à la fois résistantes et légères pour répondre aux exigences réglementaires et économiques. En grande partie, cette demande a été satisfaite grâce aux progrès rapides dans les domaines des nanosciences et de la nanotechnologie. Les recherches expérimentales et théoriques se concentrent sur la création de nouveaux composites de haute technologie tels que les matériaux à gradient fonctionnel (FGM) et les composites avancés renforcés par des nano-plaquettes de graphène. Ce sont des nano-plaquettes prometteuses car elles offrent des propriétés mécaniques, thermiques et électriques optimisées tout en offrant un gain de poids considérable.

En examinant l'impact du renforcement en nano-plaquettes de graphène sur la réponse de flexion et de flambage d'une plaque composite avancée, cette étude vise à contribuer à ce développement. Pour mener cette étude paramétrique, une théorie de déformation d'ordre supérieur en cisaillement appropriée sera utilisée.

Mots Clés : flexion, flambage, méthode analytique, composites avancés, nano-plaquettes de graphène.

Acknowledgments

First and foremost, Alhamdulillah to the Almighty Allah for giving me the strength and the ability to understand, learn, and complete this thesis. Thank you Allah for everything, Alhamdulillah.

It would not have been possible to write this master thesis without the help and support of the kind people around me, only some of whom it is possible to give a particular mention here.

I would like to express my deepest gratitude to my parents, whose unwavering support and encouragement have been the cornerstone of my academic journey. Their belief in my abilities and their endless patience has provided me with the strength to persevere through the challenges and uncertainties of this process. Your sacrifices and unwavering faith in my potential have been an unfailing source of motivation and inspiration, for which I am eternally grateful.

This thesis would not have been possible without the advice, help, support, and patience of my supervisor, Mrs. Mahi, who has the attitude and substance of a genius. She has continuously motivated me with her wise and intelligent advice since I started working under her supervision. The good advice, support, and respect of Doctor Abdellah Hassaine, have been invaluable on both academic and personal levels, for which I am extremely grateful.

I am also immensely thankful to my brother and sisters. Your understanding, patience, have been invaluable to me. You have been my constant pillar of support, always ready to listen, advise, and cheer me on, even when the demands of my studies took time away from our family moments. Your love and solidarity have made a significant difference in my life, and I am truly blessed to have you as my siblings.

To my entire family, including my extended relatives, I extend my heartfelt appreciation. Your collective support and encouragement have been instrumental in helping me reach this milestone. The warmth of your love and the strength of your belief in me have been a continuous source of comfort and reassurance. You have all played a vital role in shaping my journey, and for that, I am profoundly grateful.

I want to acknowledge all the professors and staff of the institute of aeronautics and the space studies and Saad Dahleb University, who helped me or encouraged me. I also extend my sincere thanks to my friends for their moral encouragement and support.

Finally, to everyone who has supported me in one way or another throughout this journey, whether through words of encouragement, acts of kindness, or simply by believing in me, thank you. This thesis is not just a culmination of my hard work but also a testament to your unwavering support and love.

Table of content

List of tables

List of figures

List of symbols and abbreviations

SYMBOLS:

u, v, w	Displacement along the directions of the coordinates (x,y,z)
ϕ_x, ϕ_y	Rotations around the axes x and y
$u_0, v_0, w_0, \phi_x, \phi_y$	Generalized rotations and displacements
$\varepsilon_{xx}, \varepsilon_{yy}$	Axial strains (x and y)
$\gamma_{xy}, \gamma_{yz}, \gamma_{xz}$	Shear strains
σ_{xx}, σ_{yy}	Axial stresses (x and y)
$\tau_{xy}, \tau_{yz}, \tau_{xz}$	Shear stresses
Q_{ij}	Stiffness coefficient
N_x, N_y, N_{xy}	Membrane resultant (normal and shear)
Q_x, Q_y	Transverse load resultants
M_x, M_y	Bending moment around the axes x and y respectively
M_{xy}	Twist moment
$A_{ij}, B_{ij}, D_{ij}, A^{a}_{ij}$	Tension, Coupling, Bending, and transverse shear stiffnesses
$M^{a}{}_{x}, M^{a}{}_{y}$	Higher order bending moment around the axes x and y respectively
$M^{a}{}_{xy}$	Higher order twist moment
E_U, E_k, W	Strain energy, kinetic energy, Work of external loads
δE_U	Virtual of strain energy
δ W	Virtual work
J_{mn},K_{mn} , L_{mn}, M_{mn}, N_{mn}	Arbitrary parameters
ν	Poisson coefficient
ρ	Volumetric density

E	Young's modulus
G	Shear moduls
$\mathbf{V_{gpl}}$	Volume fraction of graphene nano platelets
$\mathbf{A_{GPL}}$	Mass fraction of graphene nano platelets
$\boldsymbol{\lambda_1}$, $\boldsymbol{\lambda_2}$	Buckling parameters
$\boldsymbol{P_x}$,$\boldsymbol{P_y}$, $\boldsymbol{P_{xy}}$	Compression loads
$\boldsymbol{P_{cr}}$	Critical buckling load
$\bar{\boldsymbol{P}}_{\boldsymbol{cr}}$	Dimensionless Critical buckling load
$\boldsymbol{\varphi(z)}$	Shape function
q	Transvers load applied to the plate
$\bar{\mathbf{w}}$	Dimensionless transverse displacement
$\bar{\sigma}_{xx}$, $\bar{\sigma}_{xy}$, $\bar{\sigma}_{xz}$	Dimensionless stresses
$\boldsymbol{K}$	Bending stiffness matrix
$\boldsymbol{K'}$	Buckling stiffness matrix
d	Displacment vector
[ ]	Matrix
{ }	Vector

Abbreviation:

FGM	Functionally Graded Materials
GPL	Graphene nanoplatelets
FG-GPLRC	Functionally Graded Graphene nanoplatelets reinforced composite
UD	Uniform distribution
FG-X, FG-O	Patterns of distribution of GPLs in polymer matrix

CPT	Classical plate theory
FSDT	First order shear deformation theory
HSDT	Higher order shear deformation theory
RPT	Refined Plate theory
VD	Vapour deposition
SFF/AM	Solid Free Form/Additive manufacturing

GENERAL INTRODUCTION:

Composite materials, made up of multiple materials, offer superior properties such as stiffness, fatigue resistance, corrosion resistance, wear resistance, and weight reduction. However, conventional composite materials often face discontinuity in properties and stresses at interfaces, leading to high stress concentrations, matrix cracking, and delamination problems. Functionally Graded Materials (FGMs) can overcome these issues by continuously changing material properties, resulting in a smooth transition from one material to another. FGMs can also be tailored for specific applications, such as using graphene nano-platelets to enhance mechanical, thermal, and electrical properties while reducing structure weight.

In this project, the primary objective is to delve deeply into the intricate characteristics and behavior of a functionally graded material (FGM) plate that has been ingeniously fortified with graphene nano-platelets. The focus of the investigation centers around examining and understanding the plate's static response as well as its stability under various loading conditions, with a special emphasis on analyzing its resistance to bending and buckling. The study aims to unravel the unique mechanical properties exhibited by this innovative composite structure, shedding light on how the incorporation of graphene nano-platelets influences the overall performance and durability of the FGM plate. The plate's response to external forces and evaluating its structural integrity when subjected to different stress levels, this research seeks to contribute valuable insights to the field of materials science and engineering. With a comprehensive analysis of the plate's mechanical behavior, the project aims to provide a foundation for further advancements in FGM technology, paving the way for the development of new and improved materials that offer enhanced strength, stiffness, and resilience for various engineering applications. Through this detailed exploration, the study endeavors to advance our understanding of material design and optimization strategies, ultimately aiming to foster innovations in the realm of composite materials and structural engineering.

Previous studies:

Several studies have been carried out on FGM plates and their characteristics of bending and buckling behavior. Shen et al modeled and analyzed the thermal bending and post-buckling of GRNC laminated plates resting on an elastic foundation and subjected to in-plane temperature variation. Song et al, presented bending and buckling analyses of multilayer FG-

GRNC polymer composite plates using the first-order shear deformation theory. Daikh and Megueni, investigated the influence of plate aspect ratio, gradient index and the thermal loading conditions on the buckling of FGM sandwich plates modeled by the higher-order shear deformation plate theory. Thai et al studied mechanical behavior of multilayer FG-GRNC plates based on the four-variable refined plate theory and modified couple stress theory. Song et al also studied the free and forced vibration, buckling and postbuckling of multilayer graphene nanocomposite plates in which graphene platelets (GPLs) were nonuniformly distributed in a layer-wise manner. Wu et al, examined the thermal buckling and postbuckling of functionally graded multilayer GPL reinforced composite (GPLRC) plates and suggested that whether the thermal buckling and postbuckling resistance increases or decreases is highly dependent on the GPL distribution pattern. Iurlaro et al, carried out bending and free vibration FG sandwich plates using a refined zigzag theory and finite element method. Thai et al, examined bending, buckling and vibration of FG sandwich plates with various boundary conditions using a new FSDT. Mahi et al, proposed a new hyperbolic shear deformation theory for the bending of FG sandwich plates. Wang and Shen, analyzed a nonlinear bending of FG sandwich plate resting on elastic foundations using a two-step perturbation method.

These studies have contributed to a better understanding of the static response and the stability characteristics of a FG plates under different conditions and have explored various theoretical approaches and to analyze their behavior.

Thesis contribution:

Our thesis involves a parametric study that aims to understand how the reinforcement in graphene nano-platelets affects deflection and stresses for bending and the critical buckling load for buckling, of an FGM plate. For this, we will use an adapted shear deformation theory, which will allow us to precisely analyze the effects of this reinforcement on the bending and buckling characteristics of the plate.

This parametric study will allow us to explore different configurations of graphene nano-platelets in the FGM plate. We will also examine factors such as the size and distribution of graphene nano-platelets to determine the optimal combinations that optimize the static response and stability performance. These results will provide valuable information on how to improve the performance of graphene-reinforced composites. By applying this knowledge, industries will be able to design lighter, stronger and more durable structures, which will promote innovation and efficiency in these key areas.

The modelling of the properties of the GPL-reinforced FGM plate will be based on the Halpin-Tsai model and and Mahi's hyperbolic HSDT. The programming language adopted in this research work is Python, from which we essentially used the functions of eigenvalues and matrix system computation to obtain the buckling loads and displacement field.

Thesis organization:

This master thesis is divided into four chapters:

Chapter 1 provides a literature review of functionally graded materials, their characteristics, development history, fabrication techniques and application areas. Also, it provides a literature review on nanomaterials, their characteristics, and their role in improving...

Chapter 2 presents an in-depth literature review on the distribution laws and shear deformation theories applied to reinforced FGM structures. We will examine the mathematical models and the theoretical approaches used to describe the mechanical behavior of these structures, with an emphasis on the shear deformation phenomena.

Chapter 3 is devoted to the modeling and energy formulation of functionally graduated plates reinforced by graphene nano-platelets (FG-GPLRC). We will develop mathematical equations based on variational principles to describe the behavior of FG-GPLRC plates.

Chapter 4 is dedicated to the interpretation of the results by linking them to the theories shear deformation, the properties and distribution of the reinforcements used as well as the boundary conditions. We will also discuss the implications of these results for the design and optimization of reinforced FGM composite structures.

Finally, the work ends with a general conclusion summarizing our objectives and obtained results, followed by some perspectives.

CHAPTER 1

LITERATURE REVIEW ON REINFORCED FGM COMPOSITES STRUCTURES

1. Introduction:

During the lifetime of the human the different kind of materials was considered as a huge part of keeping him in existence, he used wood for making fire, making weapons…etc. He also used stone, bronze, iron, and other different materials to meet his daily needs. The different eras in the timeline of the human being were named according to what the human could use as an invention of a material that had been used in that time.

The Stone Age marks a period of prehistory in which humans used primitive stone tools. Lasting roughly 2.5 million years, the Stone Age ended around 5,000 years ago when humans in the Near East began working with metal and making tools and weapons from bronze [1]. Bronze Age, third phase in the development of material culture among the ancient peoples of Europe, Asia, and the Middle East, following the Paleolithic and Neolithic periods (Old Stone Age and New Stone Age, respectively). The term also denotes the first period in which metal was used. The date at which the age began varied with regions; in Greece and China, for instance, the Bronze Age began before 5000 years ago, whereas in Britain it did not start until about 3900 years ago.[2] The Iron Age was a period in human history that started between 1200 B.C. and 600 B.C., depending on the region, and followed the Stone Age and Bronze Age. During the Iron Age, people across much of Europe, Asia and parts of Africa began making tools and weapons from iron and steel. For some societies, including Ancient Greece, the start of the Iron Age was accompanied by a period of cultural decline [1].

Materials are continuously developed from iron, pure metals to composite materials which are in use today [3] and always been upgraded because of the engineering. The composite materials are one of the most genius and sophisticated materials was engineered to be very light (reducing weight) and at the same time very strong that can resist to the critical stresses.

The composite material is made of two or more constituents assembled to each other, and the choice of this constituents depends on what it will be used for. The conventional composite materials have a several advantages for example high strength to stiffness ratio, grater resistance to fatigue, wear and corrosion, high reliability…etc [3]. But in the other side we face a crucial disadvantage which called delamination. It serves for the separation of the different constituent of the composite material caused by the singularity in term of stresses in the interface of the constituents. For that reason, researchers invented an advanced composite material which called FGMs.

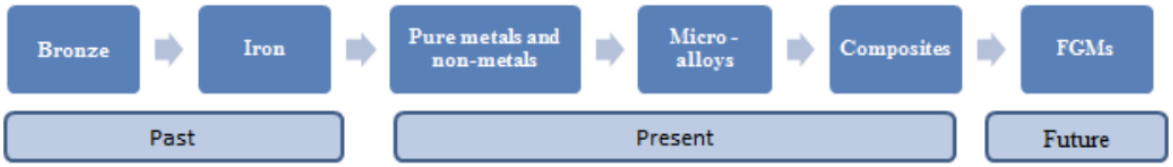

Figure 1: Continuous material development from bronze to FGMs

2. Functionally graded materials:

FGMs stands for functionally graded materials, it is the new generation of the composite materials made with two or more constituents (the most famous are ceramic and metal) where we find in a side is 100 percent made of ceramic, and through the thickness a gradual variation between ceramic and metal, till the other side which is made with 100 percent of metal. These materials are specially made to solve the famous problem of the conventional composite materials which is the delamination.

FGMs replace the sharp transition of properties with smooth and continuous varying properties of the material such as physical, chemical, and mechanical like Young's Modulus, Poisson's ratio, Shear Modulus, density, and coefficient of thermal expansion in a desired spatial direction (Figure 1). The gradual changes in volume fraction of constituent and non-identical structure at preferred direction give continuous graded properties like thermal conductivity, corrosion resistivity, specific heat, hardness, and stiffness ratio. All these advantages made FGMs far better than homogenous composite material to use in multiple applications. [4]

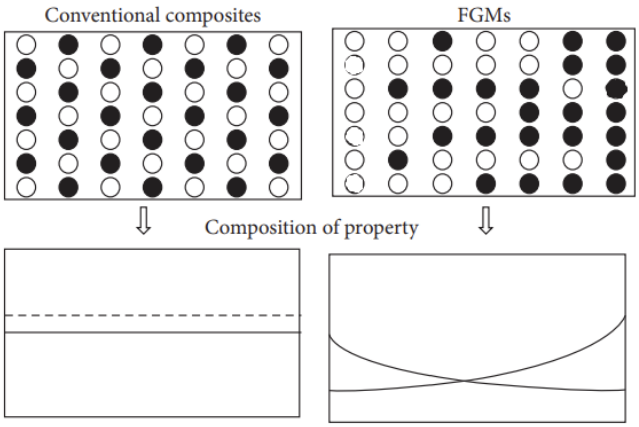

Figure 2: Variation of properties in conventional composites and FGM

The table below illustrate the properties variation depending to constituents of a ceramic metal FGM [9]

Table 1: Properties variation of a ceramic-metal FGM

Layers	Materials	Mechanical propreties
High temperature face	Ceramic	• Good thermal resistance • Good oxidation resistance • Low thermal conductivity
Intermediate layers	Ceramic-metal	• Interface problem eliminated • Thermal stresses relaxation
Low temperature face	**Metal**	• Good mechanical resistance • High thermal conductivity

2.1 Evolution of FGMs:

A new breed of composite materials named functionally graded materials (FGMs) was first invented in 1984 by Japanese researchers for the core purpose of their aerospace project that required thermal barrier with the outside temperature of 2000 k and inside 1000 k within 10 mm thickness. A decade before, Shen and Bever also worked on graded structure composite materials, but it was delayed due to unsophisticated fabrication equipment [4]. Soon, the importance of FGMs was realized, and to promote research in this area, a five-year research based national project with a cost of $11 Million was started as “Research on the basic Technology for the development of FGM for relaxation of thermal stress” (FGM PART 1). At the end of this project, researchers were able to develop 300 mm square shell and 50 mm hemispherical bowl for SiC-C FGM nose cones. Another 5-year-project that was a consequence of FGM PART 1 was started in 1992 with a cost of $9 Million called “Research on Energy Conversion Materials with Functionally Graded Structures” (FGM part 2). This project was focused to enhance energy conversion efficiency using functionally graded structure technology. Furthermore, in April 1996, the New Energy and Industrial Technology Department Organization (NEDO) funded a project with a budget of $2.5 million known as “Precompetitive Processing and characterization of Functionally Graded Materials.” The project was continued until March 2000. The purpose of the project was to develop metal-ceramic FGM on an

industrial level using spark plasma sintering (SPS) technique. Polyamide/Cu was one of the FGMs successfully manufactured by SPS technique. Most of the research was conducted on the grading of mechanical and thermal properties. However, it was needed to work on basic properties like physical and chemical. In order to fill this gap, the Ministries of Education, Science, Sports and Culture granted a research program in April 1996 entitled, "Physics and Chemistry of FGMs" that was continued for the next three years until 1999. Physics, Chemistry, Biology, and Agriculture, etc., were the fields investigated in this project. Figure 3 represents the hierarchy of modern material [4].

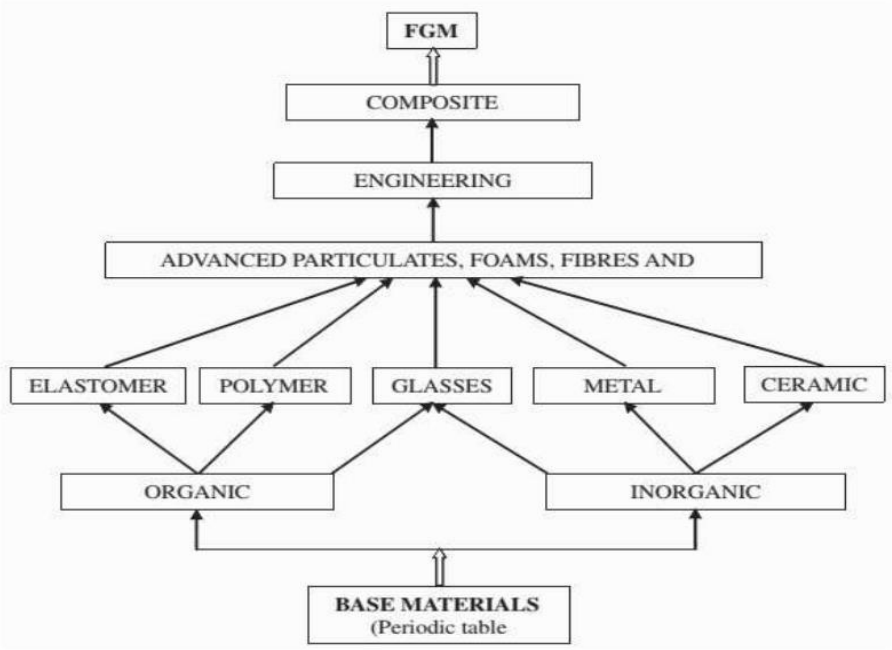

Figure 3: Representation of modern material hierarchy

2.2 FGMs classification:

To classify the functionally graded materials researchers identified a numerous criterion:

2.2.1 Based on the FGM graduation process:

2.2.1.1 Composition gradient:

The composition type of FGM gradient depends on the composition of the material, which varies from one substance to another, leading to different phases with different chemical structures. These different phases of production depend on the synthetic quantity and the conditions under which the reinforced materials are produced [5].

2.2.1.2 Microstructure gradient:

During the solidification process,the microstructure type of the FGM gradient can be achieved so that the surface of the material is extinguished. In this type, the core of the same material can cool slowly, helping generate different microstructures from the surface to the inside of the material [5].

2.2.1.3 Porosity gradient:

With the changes in the spatial location in the bulk material, the porosity type of FGM gradient in the material changes. Powder particle sizes can be measured by varying the pore particle sizes used during gradation at different positions in the bulk material [5].

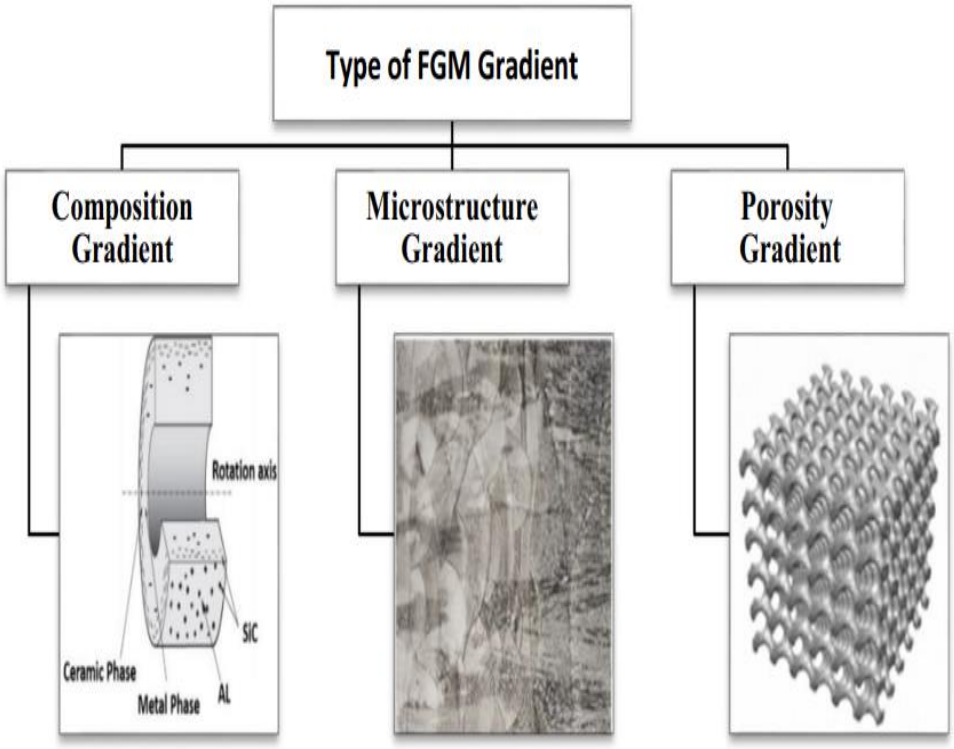

Figure 4: Typical example of three different types of FGM gradient

2.2.2 Based on the FGM structure:

FGMs can be generally classified into two main groups: continuous and discontinuous graded material as shown in Fig5. In the first group, no clear zones or separation cut lines can be observed inside the material to distinguish the properties of each zone. In the second group, the material ingredients change in a discontinuous stepwise gradation which is known as layered or discrete FGM. Continuous and discrete can further be classified into three types: composition gradient (Fig. 5c, f), orientation gradient (Fig. 5d, g), fraction gradient (Fig. 5e, h). [5]

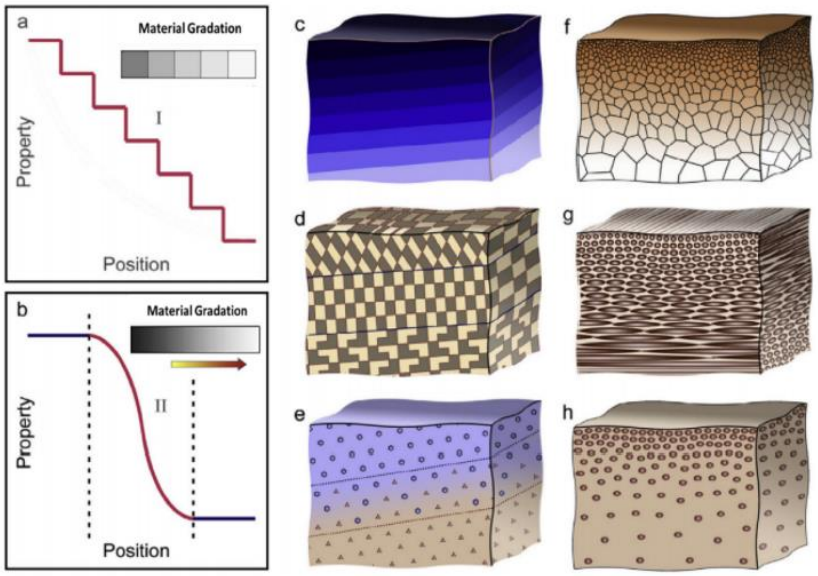

(a) Discrete/Discontinuous FGMs with interface (b) Continuous FGMs with no interface
(c , f) Composition Gradient (d , g) Orientation Gradient (e , h) Fraction Gradient

Figure 5: Structural classification of FGMs

2.2.3 Based on FGM thickness:

According to the size of the FGM, it could be classified to: thin FGMs and bulk FGMs. Thin FGMs ranges between 5 nm and 500 nm and may be extended to the micro-meter range (e.g. 1–120 μm thick deposited layers). In bulk FGMs, gradients can cover 5–350 mm. [5]

2.3 FGMs manufacturing:

As much being sophisticated the FGMs are, as much developed the elaboration methods are, to create an FGM, in the following we cite several methods used to create a gradual structure:

- **Vapour Deposition Technique**:

The following diagram gives different types of vapour deposition techniques:

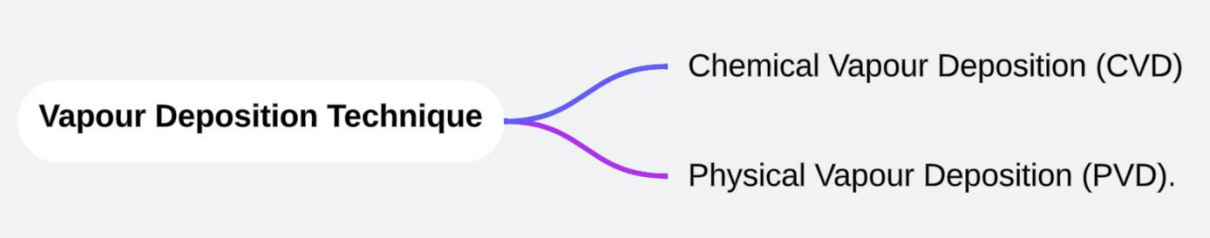

Figure 6: Different types of VD

These vapour deposition methods are used to deposit functionally graded surface coatings and they give excellent microstructure, but they can only be used for depositing thin surface coating. They are energy intensive and produce poisonous gases as their byproducts [6].

- **Powder metallurgy :**

Powder metallurgy-based technique can be used to produce bulk type FGMs with discontinuous (stepwise) structure [3]. PM is used to produce functionally graded material through three basic steps namely: weighing and mixing of powder according to the pre-designed spatial distribution as dictated by the functional requirement, stacking and ramming of the premixed-powders, and finally sintering [6].

- **Centrifugal Method :**

In the centrifugal casting method, the functionally graded material is produced by spinning the mold using gravitational force [4] to form bulk functionally graded material [6]. There are two disadvantages of this method are this method can produce only cylindrical shaped FGMs and there is limit to which type of gradient can be produced [3].

- **Solid free form fabrication/additive manufacturing (AM) techniques:**

Solid freeform fabrication (SFF)/Additive manufacturing (AM), also known as 3D printing, is a process of joining materials to make objects from 3D model data [3]. Here some types of SFF/AM techniques:

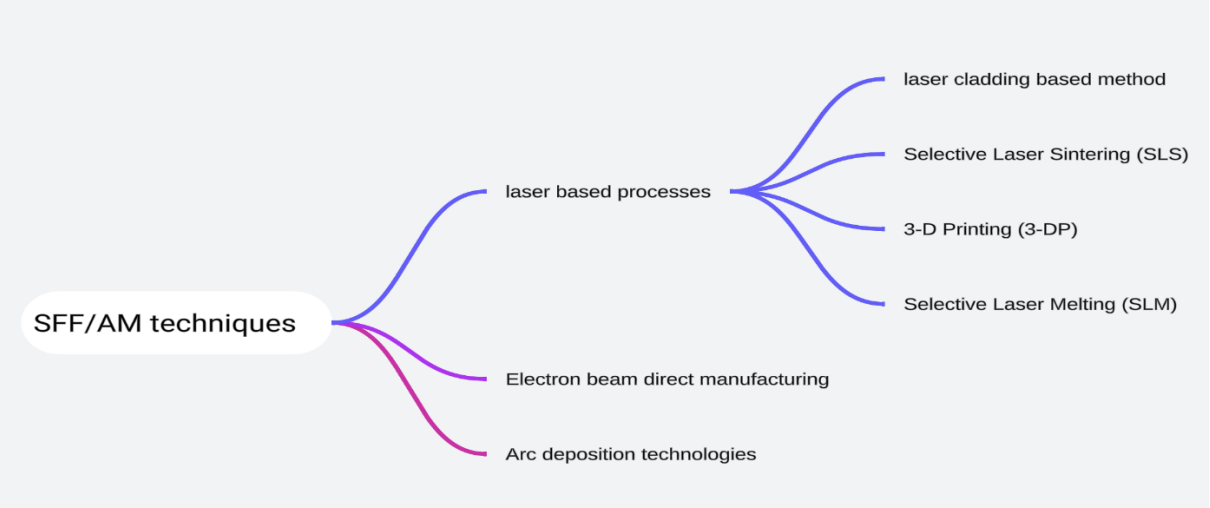

Figure 7: Different types of SFF/AM techniques

After familiarizing ourselves with different techniques to produce an FGM, we can find another classification to the functionally graded materials which is the complexity of the produced shape, each technique is specialized to produce the FGM shape depending on the order of complexity, and the following diagram gives the order of complexity and the techniques it belongs:

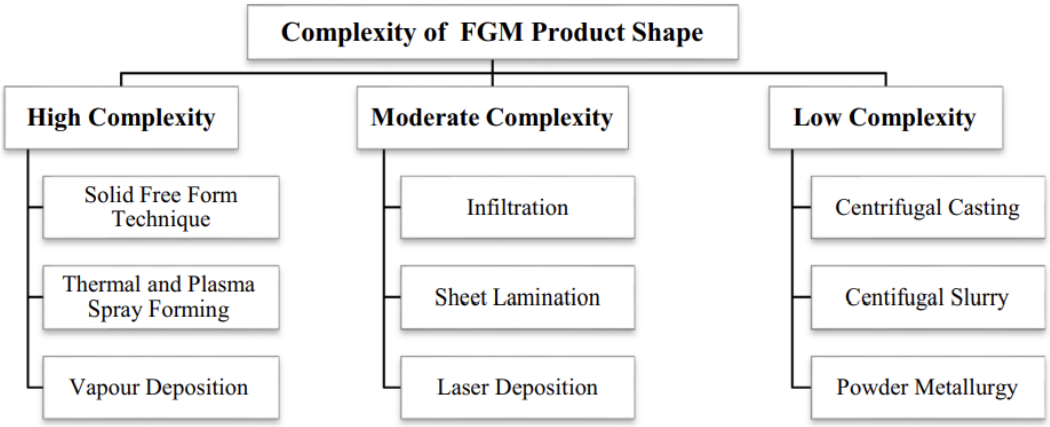

Figure 8: Classification of FGMs according to product complexity

2.4 Aeras of application of FGMs:

Functionally graded materials are designed to optimize the performance for different applications. Some of the domains where FGMs are used or have potential to be used are:

- Aerospace: FGMs can be used for thermal protection systems, rocket nozzles, turbine blades, and other components that are exposed to high temperatures and thermal stresses.
- Automobile: FGMs can be used for brake discs, pistons, cylinders, and other parts that require high wear resistance, friction reduction, and thermal stability.
- Optoelectronics: FGMs can be used for optical fibers, waveguides, lasers, and other devices that require tailored optical properties, such as refractive index, absorption, and emission.
- Energy: FGMs can be used for solar cells, fuel cells, batteries, and other devices that require efficient conversion and storage of energy, as well as corrosion resistance and durability.
- Biomedical: FGMs can be used for implants, prostheses, scaffolds, and other devices that require biocompatibility, bioactivity, and mechanical matching with the host tissue.

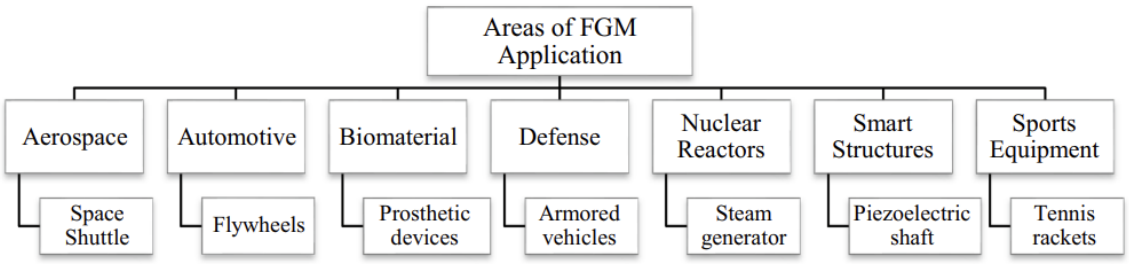

Figure 9: Functionally graded materials: field of application and examples [5]

These are some of the common domains of application of FGMs, but there are also other fields, such as civil engineering, defense, and sports, that can benefit from the use of FGMs.

3. Nanoworld:

“There's Plenty of Room at the Bottom”

-Richard Feynman-

After this announcement from Sir **Richard Feynman,** rooms at the bottom had known a huge development, or in another way a new field of science had been discovered which is nanoscience. Nanoscience focuses on investigating material phenomena at the nanoscale (10^{-9}m). So, certainly we need certain techniques to handle this specific type of materials.

Nanotechnologies are all tools, instruments and techniques for manipulating and manufacturing materials at the nanoscale (10^{-9}m).

3.1 Nanomaterials:

The basic and the key elements of nanotechnology are the "nanomaterials". The nanomaterials are the materials with less than 100 nm size ones at least in one dimension. That means they have very less size than that of microscale. The nanomaterials are usually 10−9 nm in size that means it is one billionth of a meter. The nanomaterials show different physicochemical properties than the bulk material which inherently depends on their size and shape. Surprisingly the nanomaterials produce a unique character with new characteristics and capabilities by modifying the shape and size at the nanoscale level. Nanomaterials may be of different shapes like nanorods, nanoparticles, nanosheets which can be characterized based on their dimensionality. Nanomaterials with zero-dimensional are nanoparticles, one dimensional is nanorods or nanotubes and two dimensional are generally films and layers type one. These are categorized mainly for the single isolated nanomaterials [8].

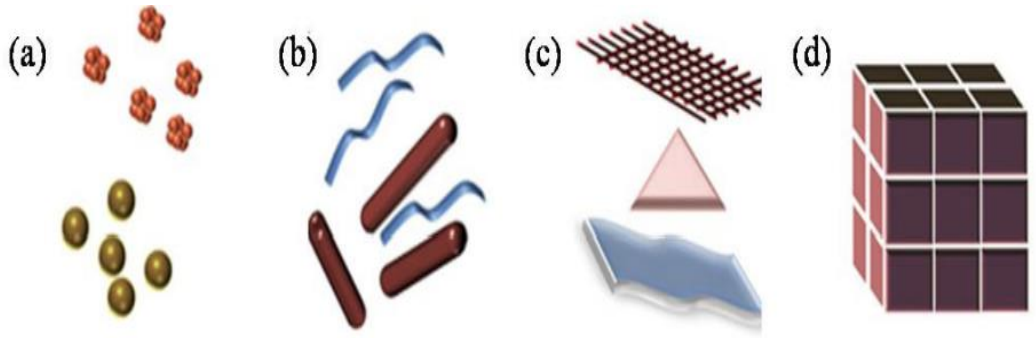

Figure 10: Classification of Nanomaterials (a) 0D spheres and clusters; (b) 1D nanofibers, nanowires, and nanorods; (c) 2D nanofilms, nanoplates, and networks; (d) 3D nanomaterials.

Nanomaterials have two significant families: the nano-objects, like nanoparticles, nanofiber, nanorods, nanoplatelets and nanosheets. The other one is the nanostructured materials such as nanocomposites, nanoporous… etc.

In this study, we are about specially to focus on some types of nano-objects.

3.1.1 nanoplatelets:

Nanosheets, nanoplatelets are a nano-objects that have one of the three spatial external dimensions belongs to the nanoscale (1-100 nm), and the other two dimension are significantly greater.

3.1.1.1 Graphene nanoplatelets:

Graphene is a single freestanding monolayer of graphite. It is the first 2D-material ever manufactured by mankind, having a thickness of one atom (0.34 nm), and lateral size orders of magnitudes larger [10]. Its synthesis is complex and cannot be mass-produced yet. For this reason, graphene nanoplatelets (GPLs) have become an alternative, with a low cost and exciting properties, and the potential for large-scale production. GPLs have few graphite layers, varying in thickness from 0.7 to 100 nm [11].

Their main properties are light weight, high aspect ratio with planar shape, good mechanical properties [11] It has a tensile strength of 125 GPa and an elastic modulus of 1.1 TPa, compared to an elastic modulus of 200 GPa for the most common steel. Its breaking strength is 42 N/m, thus graphene has 100 times better mechanical strength than steel [13], and excellent thermal and electrical conductivities, together with low cost and easy manufacture. GNPs have numerous applications as isolated materials, neat coatings and fillers of composites. This Special Issue is focused on the use of graphene nanoplatelets as nanofillers [11].

3.1.1.2 Graphene structure:

Graphene is a two-dimensional carbon allotrope. It is composed of carbon atoms positioned in a hexagonal design, Graphene can be a parent form for many carbon structures, like the above-mentioned graphite, carbon nanotubes (which can be viewed as rolled-up sheets of graphene formed into tubes) and buckyballs (spherical structures with a cage-like structure made from graphene only with some hexagonal rings replaced by pentagonal rings) [12].

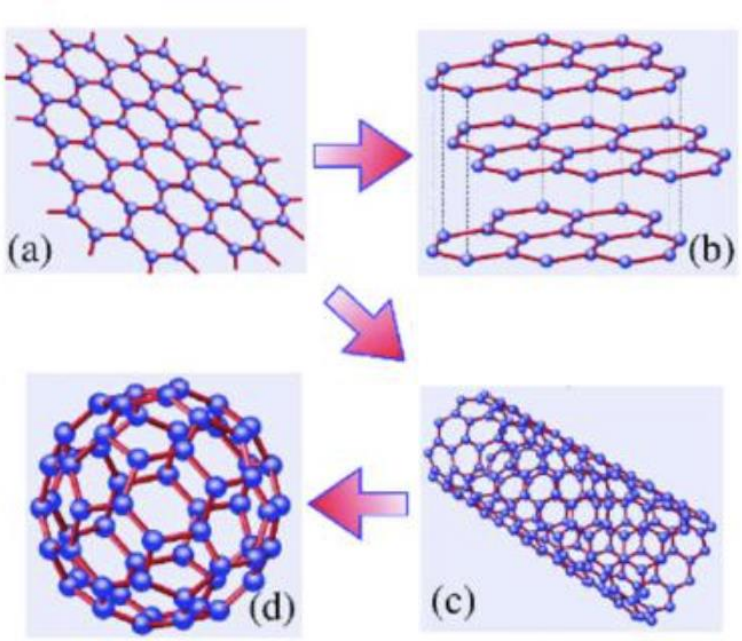

Figure 11: Different structures of carbon

3.1.1.3 Areas of application:

Graphene nanoplatelets have many applications in various fields, such as:

- Coating: Graphene nanoplatelets can improve the corrosion resistance, wear resistance, and anti-fouling properties of coatings [14] [15].
- Polymer composites: Graphene nanoplatelets can enhance the mechanical, thermal, electrical, and barrier properties of polymers, such as thermoplastics, thermosets, rubber, and elastomers [14] [15].
- Energy conversion and storage: Graphene nanoplatelets can be used as electrodes, catalysts, and additives for batteries, supercapacitors, fuel cells, and solar cells [14] [16].
- Sensing: Graphene nanoplatelets can be used as sensors for detecting gases, biomolecules, strain, pressure, and temperature [14] [16].
- Biomedicine: Graphene nanoplatelets can be used as drug delivery agents, bioimaging agents, antibacterial agents, and tissue engineering scaffolds [14] [10].

3.1.2 Nanotubes:

Materials such as carbon nanotubes, polyester nanofibers, bore nanotubes, and so on that are related to nano-objects having two exterior dimensions on the nanometer scale and a third dimension that is substantially greater. These concepts describe long-line nano-objects that have lengths of 500–10,000 nm and sections of 1and a few hundred nm.

- Rigid nanofibers: These are nanofibers that have a solid cross-section and a high aspect ratio. They can be used as building blocks for nanodevices, nanosensors, and nanocomposites [17]. Examples of rigid nanofibers are nanorods and nanowires.
- Hollow nanofibers: These are nanofibers that have a hollow core and a thin wall. They can be used as drug delivery vehicles, catalyst supports, and gas separation membranes [17]. Examples of hollow nanofibers are nanotubes and nanohorns.
- Electrically conductive nanofibers: These are nanofibers that have a high electrical conductivity and can be used as electrodes, interconnects, and transistors [17]. Examples of electrically conductive nanofibers are carbon nanotubes, metal nanowires, and graphene nanoribbons.

3.1.2.1 Carbon nanotubes:

CNTs, also called buckytubes, are cylindrical carbon molecules with unique properties that make them potentially useful in a wide variety of applications. CNTs exhibit extraordinary strength as well as unique electrical, mechanical and thermal properties. CNTs are the members of the fullerene family, which was discovered by Kroto et al. in 1985. Buckyballs are spherical fullerenes, whereas CNTs are cylindrical, with at least one end typically capped with a hemisphere with the buckyball structure. The name CNT derives from the size, as the diameter of a nanotube is on the order of a few nanometers. Iijima first synthesized multi-walled carbon nanotubes (MWNTs) in 1991 using a simple arc-evaporation method. However, CNTs were discovered long before researchers even imagined that carbon may exist in such a diverse allotropic form [18]. CNTs, also known as tubular fullerenes, are cylindrical graphene sheets of sp^2 -bonded carbon atoms. In CNTs the graphene sheet is rolled upon itself to form different allotropes of carbon, including graphite, fullerenes and CNTs [18].

CNTs reportedly have extremely high surface areas, large aspect ratios, and remarkably high mechanical strength. The tensile strength of CNTs is 100 times greater than that of steel, and the electrical and thermal conductivities approach those of copper. These unique properties

make CNTs good candidates as fillers in different polymers and ceramics to realize desirable consumer products. It has also been predicted that CNT-based field-effect transistors (FETs) will soon supplant their silicon-based analog counterparts. CNTs are also good incorporating agents due to their unique electrical, mechanical and thermal properties [18].

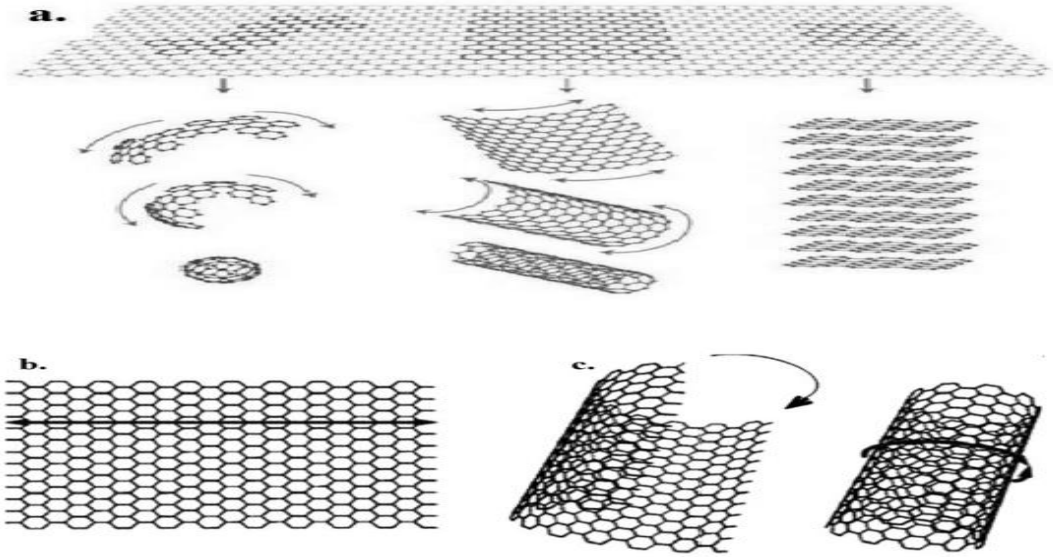

Figure 12: (a) Formation of graphene derivatives. (b) Graphene sheet. (c) Graphene sheets rolled into carbon nanotubes.

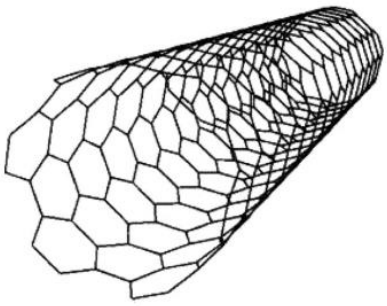

Figure 13: single wall carbon nanotube

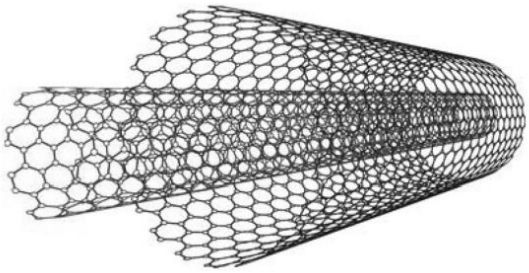

Figure 14: multi wall carbon nanotube

3.1.3 Nanoparticles:

Nanoparticles are a zero-dimensional nanomaterial where all three external spatial dimensions belongs to the nanoscale. It means the length, breadth and height is fixed at a single point for example nano dots.

Nanoparticles could be classified to organic nanoparticles and non-organic nanoparticles.

3.2 Methods of manufacturing of Nanomaterials:

The nanoparticles are synthesized by various methods that are categorized into bottom-up or top-down method.

3.2.1 Bottom-up method :

Bottom-up or constructive method is the build-up of material from atom to clusters to nanoparticles. Sol-gel, spinning, chemical vapour deposition (CVD), pyrolysis and biosynthesis are the most commonly used bottom-up methods for nanoparticle production [20].

3.2.2 Top-down method :

Top-down or destructive method is the reduction of a bulk material to nanometric scale particles. Mechanical milling, nanolithography, laser ablation, sputtering and thermal decomposition are some of the most widely used nanoparticle synthesis methods[20].

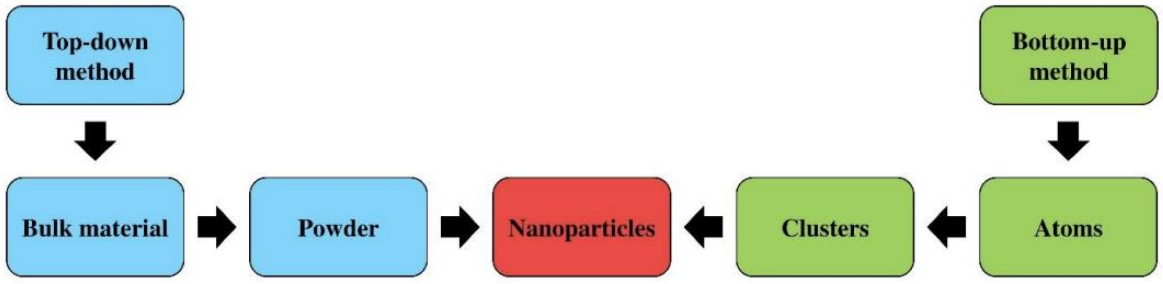

Figure 15: Synthesis proccess

Table 2: Categories of the nanomaterial synthesized from the various methods [20]

Category	Method	Nanoparticles
Bottom-up	Sol-gel	Carbon, metal and metal oxide based
	Spinning	Organic polymers
	Chemical Vapour Deposition (CVD)	Carbon and metal based
	Pyrolysis	Carbon and metal oxide based

	Biosynthesis	Organic polymers and metal based
Top-down	Mechanical milling	Metal, oxide and polymer based
	Nanolithography	Metal based
	Laser ablation	Carbon based and metal oxide based
	Sputtering	Metal based
	Thermal decomposition	Carbon and metal oxide based

3.3 Areas of application of nanomaterials:

Nanomaterials are of great interest because they have a lot of potential to create new and innovative products across many areas. By more directly steering the reactions and interactions between atoms at the nanoscale, nanomaterials can be produced and their properties can be steered in unusual ways [19].

Table 3: Different type of nanomaterials and their application areas [7]

Nanoceramic	• Structural composite materials • Anti-UV components • Mechano-chemical polishing of substrate (wafers) in microelectronics • Photocatalytic applications
Nanometallic	• Antimicrobial and/or catalysis sectors • Conductive layers of screens, sensors or energy materials
Nanoporous	• Aerogels for thermal insulation in the fields of electronics, optics and catalysis • Biomedical field for vectorization or implant applications
Nanotubes	• Electrical conductive nanocomposites • Structural materials • Single wall nanotubes for applications in the field of electronics, screens
Massive Nanomaterials	• Hard coatings • Structural components for aviation, automotive, pipelines for oil and gas industries • Sports • Anti-corrosion sector

Dendrimers	• Medical field (medication administration, rapid detection) • Cosmetic field
Quanta dots	• Optoelectronic applications (screens) • Photovoltaic cells • Inks and paints for anti-counterfeiting marking applications
Fullerenes	• Sports sectors (nanocomposites) • Cosmetics
Nanowires	• Conductive layers of the screens or solar cells the electronic devices

4. Conclusion:

This chapter has introduced us to functionally graded materials, their effective properties, and its creativeness. It has also familiarized us with the nanoworld, the particular kind of material that falls under it, its characteristics, and its many elaboration techniques.

We also gained an understanding of the kinds of materials that bulk materials referred to in our work as "functionally graded materials" may be reinforced with. We are going to strengthen a functionally graded material by using graphene nanoplatelets as nanofillers.

The study of reinforced functionally graded materials is novel, any logical concept might be deemed innovative. That's what we decided to aim for in the long run.

CHAPTER 2

LITERATURE REVIEW ON DISTRIBUTION LAWS AND PLATE THEORIES APPLICABLE ON FGM PLATE

1. Introduction:

The study of functionally graded materials has become increasingly important in the world of materials science. These materials are unique in that their mechanical properties can be distributed in a way that optimizes their performance for a specific application. This means that engineers can tailor materials to meet the exact needs of a particular project, resulting in improved efficiency and effectiveness.

To fully understand how functionally graded materials perform, it is important to look at their mechanical properties. These properties include factors such as strength, stiffness, toughness, and ductility. By carefully controlling the distribution of these properties, engineers can create materials that are optimized for a specific application.

As we embark on this journey of understanding the complexities of plate behavior, it is imperative that we delve into the various theories that have been put forth by experts in the field. These theories aim to explain the behavior of plates when subjected to deformations, and provide us with a comprehensive understanding of the underlying mechanics at play.

2. Laws governing property distribution:

It is beneficial to use homogenization schemes for the graded materials that contain parallel homogeneous layers with definite elastic moduli. The properties of each layer are assessed with appropriate averaging methods. The thickness of layer and the volume fractions of phase constituents contained in the layer are chosen to approximate the substantial variation in a phase volume fraction of graded materials. Some of the homogenization models are discussed below [21].

2.1 Gradation Laws :

2.1.1 Power law Model (P-FGM):

Power law is found to be most cited and accepted model in the scientific literature. The material properties are varied in specific direction (unidirectional) which is given by [21] equation (2-1)

$$P(z) = (Pc - Pm)\,Vf + Pm \qquad \textbf{(2-1)}$$

Here P represent the general material properties such as Elastic modulus, Pc and Pm symbolize the properties of ceramic and metal faces of functionally graded structure and V_f denote volume fraction.

Properties of P-FGMs depends on the volume fraction (V_f) that follow a law given by equation **(2-2)**

$$Vf = \left(\frac{1}{2} + \frac{z}{h}\right)^n \quad , \quad -\frac{h}{2} \geq z \geq \frac{h}{2} \qquad \textbf{(2-2)}$$

Here n is termed as power-law index that indicates the level of material inhomogeneity in FGMs. If $n=0$ then FGM plate is fully ceramic, whereas n= ∞ indicate a fully metallic plate.

The boundary conditions define the properties at bottom surface of the plate which are given by the, P(z) = Pm for $\frac{z}{h}$ **= -1/2**; hence. V_f =**0** At the top surface, properties are P(z) = Pc, for $\frac{z}{h}$ **= 1/2 [21]**

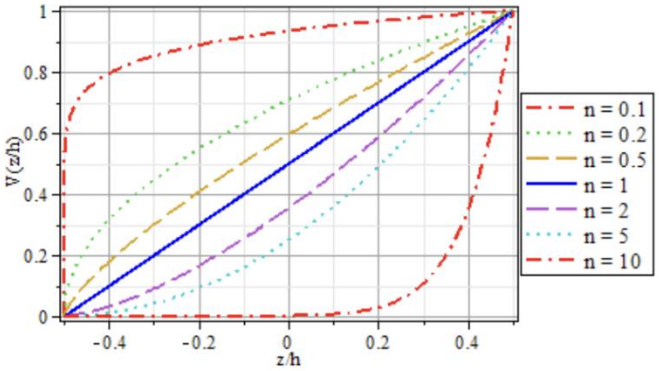

Figure 16: volume fraction variation [22]

2.1.2 Exponential law Model (E-FGM):

This model is widely used to study the fracture mechanics. Researchers have implemented this law in analyzing the static and dynamic performance of FGM structures. The properties of one/uni-directional (UD) FGMs are given by [21] equation **(2-3)**

$$P(z) = \mathrm{P_t}.e^{(1/h).h.(P_t/P_b).(z+h/2)} \qquad \textbf{(2-3)}$$

The terms P, P_t, and P_b are the properties along the Z-direction, bottom and top surface respectively.

In the case of a thermal effect, we face another model:

$$P(z,T) = P_b(T).e^{(z/h+1/2).\ln(P_t(T)/P_b(T))} \quad , \quad -\frac{h}{2} \geq z \geq \frac{h}{2} \qquad \textbf{(2-4)}$$

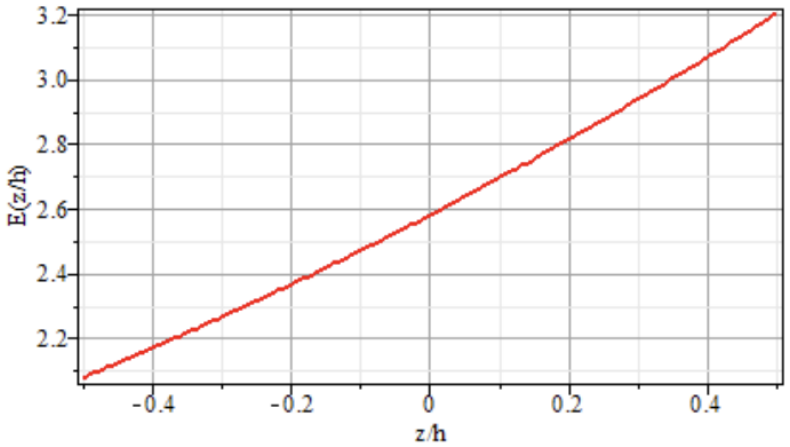

Figure 17: Young modulus variation ([Pa] x 10-11) of an E-FGM (SUS304-Al2O3) (presence of a thermal effect) [22]

2.1.3 Sigmoid law Model (S-FGM):

This model is designed by using a FGM of single power law model to the multi-layered composites. As reported by Chi and Chung the volume fraction is determined using two power law functions. This law provides a smoother distribution of stresses at every interface. For uni directional FGMs this law is given by [21] (2-5) and (2-6)

$$V(z) = \frac{1}{2}\left(\frac{\frac{h}{2}+z}{\frac{h}{2}}\right)^n \quad , \quad -\frac{h}{2} \leq z \leq 0 \qquad \textbf{(2-5)}$$

$$V(z) = 1 - \frac{1}{2}\left(\frac{\frac{h}{2}+z}{\frac{h}{2}}\right)^n \quad , \quad 0 \leq z \leq \frac{h}{2} \qquad \textbf{(2-6)}$$

n is the index of the volume fraction of the S-FGM [22].

The property of the S-FGM is written according to the volume fraction as follows [22]:

$$P(z) = (Pt - Pb)V(z) + Pb \quad , \quad -\frac{h}{2} \leq z \leq 0 \qquad \textbf{(2-7)}$$

$$P(z) = (Pt - Pb)V(z) + Pb \quad , \quad 0 \leq z \leq \frac{h}{2} \qquad \textbf{(2-8)}$$

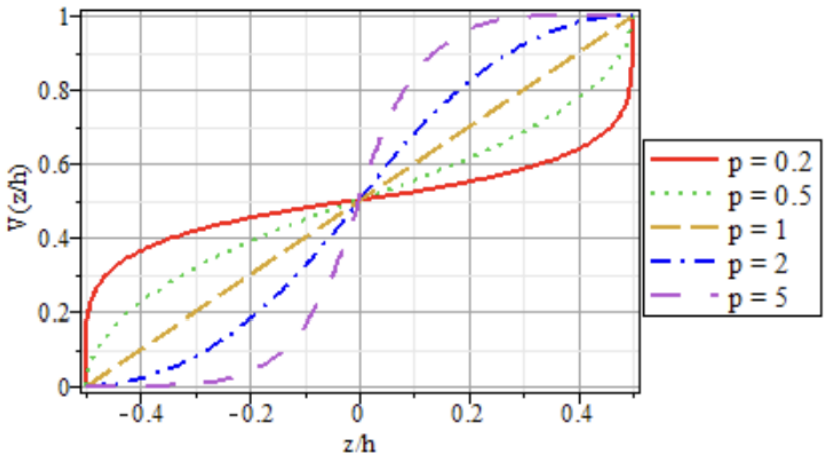

Figure 18: Variation de la fraction volumique du S-FGM [22]

2.1.4 Voigt Model :

Voigt model (known also as rule of mixture ROM) is used to compute FGM property (P) as a function of volume fractions and material properties of constituents as represented in (2-9). This model is applied to uni directional FGM structures but cannot be applied to porous structures [21].

$$\mathrm{P} = \sum_{j=1}^{k} P\mathrm{j}\, V f\mathrm{j} \qquad \textbf{(2-9)}$$

Voigt model also provide the material properties of FGMs such as Young's modulus, mass density, and Poisson's ratio [21], for example let's take an FGM structure with two phases constituents (metal-ceramic), the overall property of this structure could be written as follows:

$$P = P\mathrm{m}Vm + P\mathrm{c}V\mathrm{c} \qquad \textbf{(2-10)}$$

P: Property along the z axis.
Pm, Pc : The mechanical property of metal and ceramic respectively.
Vm, Vc: volume fraction of metal and ceramic respectively.

2.1.5 Trigonometric Model :

This model provides the volume fraction in the form of trigonometric function for UD FGMs as given in [21] **(2-11)**

$$Vf = C\left(\frac{1}{2} - \frac{\alpha}{2}\sin\left(\frac{n\pi z}{h} + \varphi\right)\right)^{\gamma} \quad (2\text{-}\mathbf{11})$$

2.1.6 Viola Tornabene law Model

This model is mainly applied in the analysis of functionally graded beams. With the formulation one can select materials mixture either at bottom or top surface of a beam. This law is further categorized as three parameter and four parameter models which are given in (2-12) & (2-13) respectively [21].

$$Vf = \left(\frac{1}{2} - \frac{z}{h} + b\left(\frac{1}{2} + \frac{z}{h}\right)^{c}\right)^{p} \quad (2\text{-}\mathbf{12})$$

$$Vf = \left(\frac{1}{2} - a\left(\frac{1}{2} - \frac{z}{h}\right) + b\left(\frac{1}{2} + \frac{z}{h}\right)^{c}\right)^{p} \quad (2\text{-}\mathbf{13})$$

The terms a, b, c, p represent the propagation of material along the thickness direction of beam. This model provides most diverse material variation when compared to power law model.

2.2 Microstructural properties caracterization models :

2.2.1 Mori-Tanaka Scheme :

The execution of different homogenization models in a graded material system begins with the estimation of effective elastic moduli. In FGMs, overall local moduli are approximated to those of matrix-based composites reinforced with spherical particulate. Concerning the applications, the following relations for randomly distributed isotropic reinforcement particulate in an isotropic matrix of graded materials are given below [21].

The effective Young's modulus & Poisson's ratio is given by **(2-14)** and **(2-15)**

$$E = \frac{9KG}{3K + G} \quad (2\text{-}\mathbf{14})$$

$$\nu = \frac{3K - 2G}{2(3K + G)} \quad (2\text{-}\mathbf{15})$$

This model is further expressed as (2-16) and (2-18)

$$\frac{K - K1}{K2 - K1} = \frac{Vf}{1 + \frac{3Vf(K2 - K1)}{(3K1 + 4G1)}} \quad (2\text{-}\mathbf{16})$$

$$\frac{G-G1}{G2-G1}=\frac{Vf}{\frac{Vf(G2-G1)}{1+(G1+f1)}} \tag{2-17}$$

$$f1=\frac{\mathrm{G1}\,(9\mathrm{K1}-8\mathrm{G1}\,)}{6(\mathrm{K1}\,+\,2\mathrm{G1}\,)} \tag{2-18}$$

Where E is Young's modulus, is Poisson's ratio, K and G are local bulk and shear modulus ν respectively and suffixes 1, 2 represent matrix and reinforcement phases.

2.2.2 Self-consistent estimation Model :

In particular, this model is suited for estimating the effective moduli in the areas that possess similar microstructure [21]. The Hill self-consistent method assumes that each reinforcement inclusion is contained in a continuous material for which the properties are those of a composite. This method does not differentiate between the matrix phase and the reinforcement phase; implying that the same global moduli is estimated in another composite where the roles of the two phases are permutated. This allows the estimation of the effective moduli in regions where the skeleton of the microstructure has a continuous shape [22].

$$K=\frac{1}{\frac{\mathrm{V1}}{\mathrm{K1}+\frac{3}{4}G}+\frac{V2}{K2+\frac{3}{4}G}}-\frac{3}{4}G \tag{2-19}$$

It utilizes quadratic equation which must be solved at every surface of FGM plate to attain the shear modulus.

$$\left[\frac{V1K1}{K1+\frac{3}{4}G}+\frac{V2K2}{K2+\frac{3}{4}G}\right]+5\left[\frac{V1G2}{G-G2}+\frac{V2G1}{G-G1}\right]+2=0 \tag{2-20}$$

2.2.3 Hashin-Shtrikman bounds model :

This model is applied to develop the effective properties of a two-phase material having spherical shaped particles that are distributed randomly. It is a variation approach which provide the material properties at upper and lower bounds. (2-**21**) & (2-**22**) represent the effective shear and bulk moduli respectively.

$$G^{+} = G2 + \frac{(1-Vf)}{\frac{1}{G2-G1}+\frac{6(K2+2G2)Vf}{5G2(3K2+4G2)}} \quad ; \qquad G^{-} = G1 + \frac{Vf}{\frac{1}{G1-G2}+\frac{6(K2+2G1)(1-Vf)}{5G1(3K1+4G1)}} \tag{2-21}$$

$$K^{+} = K2 + \frac{(1-Vf)}{\frac{1}{K1-K2}+\frac{3Vf}{3K2+4G2}} \quad ; \qquad K^{-} = K1 + \frac{Vf}{\frac{1}{K2-K1}+\frac{3(1-Vf)}{3K1+4G1}} \tag{2-22}$$

The properties at upper and lower bounds are represented with superscripts + and – symbols. After obtaining the Shear and Bulk modulus, the Elastic modulus and Poisson's ratio are calculated using (2-**14**) and(2-**15**). The effective properties computed at lower bound is identical as reported by Mori-Tanaka scheme [21].

2.2.4 Halpin-Tsai model :

Halpin-Tsai model is a semi-empirical method to predict the elastic properties of fibre reinforced composites. This model can take into consideration the geometric characteristics and the orientation of the filler that would considerably affect the reinforcing efficiency. The longitudinal modulus E_{11}, the transverse modulus E_{22}, and the shear modulus G_{12} can be obtained as,[23]

$$E_{11} = \frac{1+\xi_{11}\eta_{11}Vf}{1-\eta_{11}Vf}E_m \quad ; \quad E_{22} = \frac{1+\xi_{22}\eta_{22}Vf}{1-\eta_{22}Vf}E_m \quad ; \; G_{12} = \frac{1}{1-\eta_{12}Vf}G_m \tag{2-23}$$

where η_{11}, η_{22} and η_{12} take the following expressions,

$$\eta_{11} = \frac{\left(E_f/E_m\right)-1}{\left(E_f/E_m\right)+\xi_{11}} \quad ; \quad \eta_{22} = \frac{\left(E_f/E_m\right)-1}{\left(E_f/E_m\right)+\xi_{22}} \; ; \; \eta_{12} = \frac{\left(G_f/G_m\right)-1}{\left(G_f/G_m\right)} \tag{2-24}$$

η_{11}, η_{22} , η_{12} are the filler length distribution factors in different directions.

ξ_{11}, ξ_{22} are the shape size parameters along longitudinal and transverse directions.

The reinforcement geometry factors have different expressions for different reinforcement shape. For platelets or lamellar-shaped fillers, ξ11 and ξ22 are defined as

$$\xi_{11} = 2\left(l/t\right) \qquad ; \qquad \xi_{22} = 2\left(w/t\right) \tag{2-25}$$

where l, w, and t represent the length, width and thickness of the rectangular filler, respectively.

The Young's modulus of the composite with randomly oriented reinforcement is given by,

$$E_c = {}^{3}/_{8}\, E_{11} + {}^{5}/_{8}\, E_{22} \qquad (2\text{-}\mathbf{26})$$

3. Plate deformation theories:

3.1 Plate Definition :

A plate is an elastic solid that has one dimension depending on the thickness, is small compared to the other two, and usually has a plane of symmetry in the middle of the width that we will call the mid-surface. By convention, this surface will be the plane (x-y), and the axis (o-z) corresponds to the transverse axis according to the thickness. [24].

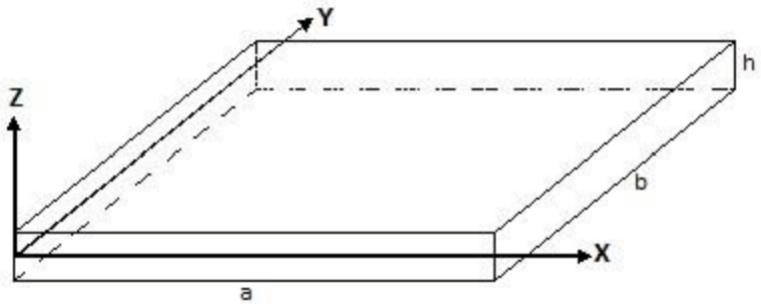

Figure 19: Geometry of a rectangular shape plate

The problems encountered mainly concern issues of dimensioning or control of vibrations and stresses. To better know the response of the dynamic and static behavior of the structure, it is imperative to approach in the most correct way possible the phenomena put into play by the plates that are more or less complex. For example, a bridge board, a building, a car box, an airplane wing, a boat... Among all these areas of application, several types of plates can be distinguished: membrane plates, thin, moderate, and thick plates with different material properties. In this study, we will be interested in heterogeneous plates in advanced composite materials, called properties gradient materials that are usually made up of two different constituents [24].

In order to solve the problems of structures having as structural elements FGM beams and plates in the elastic field, it is necessary to choose the correct theory correctly describing the static and dynamic behavior of the structure as well as the method of resolution to be applied. It was in 1888 that Love used Gustav Kirchhoff's hypotheses, themselves inspired by Euler-Bernoulli's, to establish a theory of thin plates "also known as the classical theory or Kirchhof-Love theory". The theory of semi-thick plates "theory of deformations of the first order" was consolidated by Mindlin from the work of Timoshenko [25] and Reissner [26]. Then, higher-order theories have come to improve the assumptions of classical and first-class theories when the thickness of the plate becomes significant. There is also the theory based on the three-dimensional elasticity "3-D theory" that makes no restrictive assumptions on the displacement of the plate [24]. In our study, we are interested in 2D plate elements.

3.2 Classical plate theory “Kirchhoff-love theory”:

A thin plate is referred to when the deflection, generated by the shear deformations remains negligible in front of the deflection generated from the curvature of the plate. In the case of a homogeneous isotropic plate, the shear part in the deflection is directly connected to the slenderness (L/h), (slenderness ration $h/a \leq 0.05$) [22]. The “classical plate theory” is generalized here to account for anisotropic and nonhomogeneous material behaviors [27]. The Kirchhoff assumptions taken by Love are as follows [22][24]:

- The material points, located on a normal to the mid-surface not deformed, remain on a straight in the deformation configuration.
- Transverse deformation, ε_{zz} equals to 0 (no strain variation throughout the plate.). The straight sections, initially normal to the mid-plane, remain flat and normal to it after deformation.
- The normal stress in the transverse direction is small, therefore negligible compared to the stress belonging to the plate plane (plane stress state).
- The nonlinear terms of the displacement are neglected. Rotation inertia is alsoneglected.

The CPT theory is the simplest of approaches that could describe the mechanical behavior of plates.

The displacement field written as:

$$\begin{cases} u(x,y,z) = u_0(x,y) - z\theta_y \\ v(x,y,z) = v_0(x,y) - z\theta_x \\ w(x,y,z) = w_0(x,y) \end{cases} \quad \textbf{(2-27)}$$

With:

$u_0(x,y)$ and $v_0(x,y)$: Membrane displacement in x and y directions, respectively,

$w_0(x,y)$: the plate deflection

θ_x and θ_y : Rotations due to bending (without shear effect).

The rotation angles of the deflection of the mid-surface are expressed as the transverse displacement $w_0(x,y)$ by,

$$\theta_y = \frac{\partial w_0}{\partial x} \quad ; \quad \theta_x = \frac{\partial w_0}{\partial y} \quad \textbf{(2-28)}$$

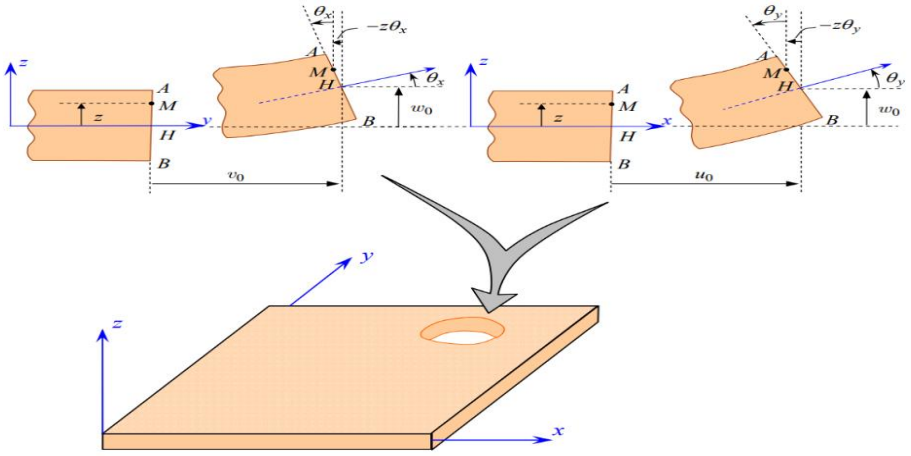

Figure 20: kinematic illustration of Kirchhoff-love plate.

The effect of transverse shear deformation increases significantly when the slenderness ratio h/a or h/b (a and b refers to length and width of the plate respectively) is greater than or equal to 0.05. Given theory neglects transverse shear flexibility, this leads to an overestimation

of the bending stiffness and, consequently, an overestimation of vibration frequencies and an underestimation of displacements [22].

3.3 Shear deformation theories:

3.3.1 First order shear deformation theory:

When the plate thickness no longer allows verification of Kirchhoff's bending motion hypotheses [22], a new theory based on the study of a moderated plate thickness was taken in consideration. The first-order shear deformation theory extended the classical plate theory by taking into account the effect of transverse shear, in which case stresses and strains are constant across the thickness of the plate [24].

In contrast to thin plate theory, Mindlin-Reissner's theory [26] assumes that cross-sections, initially normal to the mid-plane, remain flat and not necessarily normal to it after deformation [22].

The displacement field is given by,

$$\begin{cases} u(x,y,z) = u_0(x,y) - z\phi_x \\ v(x,y,z) = v_0(x,y) - z\phi_y \\ w(x,y,z) = w_0(x,y) \end{cases} \quad (\mathbf{2\text{-}29})$$

With:

ϕ_x and ϕ_y are rotations of the mean plane normal around the x and y axes.

The displacement field defined in the above expression allows us to take up the classical described in the last section by the replacement,

$$\phi_x = \frac{\partial w_0}{\partial x} \quad ; \quad \phi_y = \frac{\partial w_0}{\partial y} \quad (\mathbf{2\text{-}30})$$

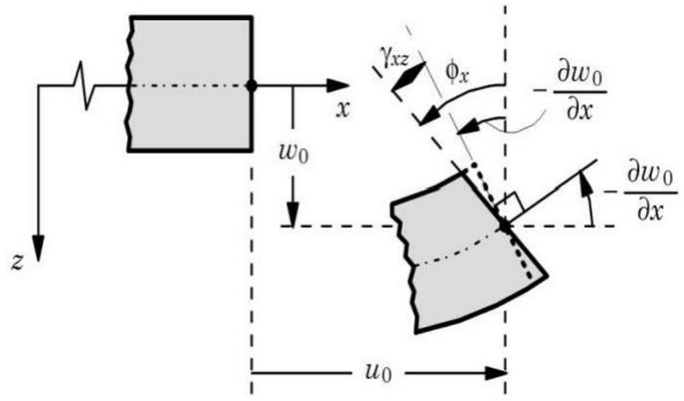

Figure 21: kinematic illustration of Reissner-Mindlin plate

Since first-order plate theory (FSDPT) does not satisfy the boundary conditions at the top and bottom surfaces of the plate (non-zero tensile stresses), a through-thickness shear correction factor is required. The value of this correction factor depends on the plate geometry, the variation in Poisson's ratio the variation of Poisson's ratio across the thickness, the loading applied and the imposed boundary conditions [22].

Moreover, to avoid the use of shear correction factor, many higher order shear deformation theories (HSDTs) were developed based on the assumption of nonlinear variations of in-plane displacements within the plate thickness [28].

3.3.2 Higher order shear deformation theories:

This class of finer theories is based on the development of displacement in thickness to order two or higher. These theories are particularly well suited to modeling the behavior of thick plates or short beams, where transverse deformation plays a predominant role, these models do not require correction factors. The high-order theory is based on a nonlinear distribution of fields in the thickness of the plate [24]. This theory uses a Taylor series expansion through the thickness of the displacement field, which can be represented by the following form [7][22]:

$$U(x,y,z,t) = U_0(x,y,t) + z\phi_x(x,y,t) + z^2{\phi_x}^2(x,y,t) + \cdots + z^n{\phi_x}^n(x,y,t) \quad \textbf{(2-31)}$$

Second order:

$$\begin{cases} u(x,y,z,t) = u_0(x,y,t) + z\phi_x(x,y,t) + z^2\psi_x(x,y,t) \\ v(x,y,z,t) = v_0(x,y,t) + z\phi_y(x,y,t) + z^2\psi_y(x,y,t) \\ w(x,y,z,t) = w_0(x,y,t) + z\phi_z(x,y,t) + z^2\psi_z(x,y,t) \end{cases} \quad (\mathbf{2\text{-}32})$$

Where $u_0, v_0, w_0, \phi_x, \phi_y, \phi_z, \psi_x, \psi_y, \psi_z, \ , \chi_y, \chi_z$ are the unknown functions.

Third order:

$$\begin{cases} u(x,y,z) = u_0(x,y,t) + z\phi_x(x,y,t) + z^2\psi_x(x,y,t) + z^3\chi_x(x,y,t) \\ v(x,y,z) = v_0(x,y,t) + z\phi_y(x,y,t) + z^2\psi_y(x,y,t) + z^3\chi_y(x,y,t) \\ w(x,y,z) = w_0(x,y,t) + z\phi_z(x,y,t) + z^2\psi_z(x,y,t) + z^3\chi_z(x,y,t) \end{cases} \quad (\mathbf{2\text{-}33})$$

Where $u_0, v_0, w_0, \phi_x, \phi_y, \phi_z, \psi_x, \psi_y, \psi_z, \ \chi_x, \chi_y, \chi_z$ are the unknown functions must be found to describe the plate motion.

The assumptions underlying the development of these theories are [22]:

- Displacements are small compared to the plate thickness.
- Cross-sections, initially flat and normal to the mid-plane, do not necessarily remain flat and normal to it after deformation.
- Axial deformation in the transverse direction is not negligible, which means that the plate undergoes thickness deformation.
- Normal stress in the transverse direction is generally not negligible.
- Flexural and shear deformations are both important and interdependent.
- The material points, located on a normal to the mid-surface not deformed, not necessary remain on a straight in the deformation configuration, which means that the plate undergoes thickness deformation.

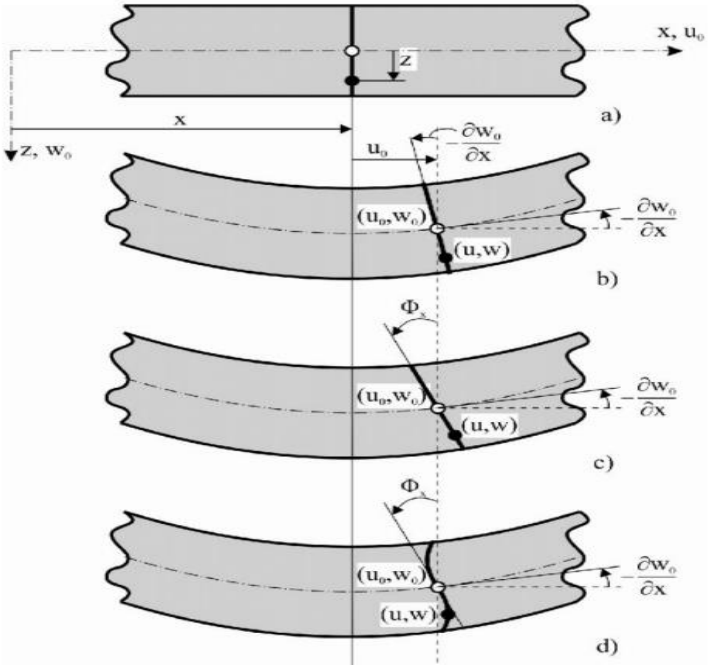

Figure 22: Transverse shear deformation of a plane according to various plate theories.

Practically, it can be seen that the higher-order theory of thick plates can be complex to apply, and often requires the use of numerical methods to solve the equations [7].

3.3.2.1 Refined theory:

First-order (FSDT) and higher-order (HSDT) theories are impractical due to the number of higher-order terms introduced into the formulation. In order to reduce the number of variables used in existing formulations, Shimpi developed a refined model for isotropic plates (RPT: Refined Plate Theory). The most interesting features of this method are that it does not require a shear correction coefficient and has many similarities with classical plate theory in terms of equations of motion, boundary conditions and moment expressions. The RPT theory was then successfully adapted to orthotropic plates by Shimpi and Patel and by Kim, Thai et al. and to FGM plate bending by Atmane, Tounsi [22]. Refined Plate Theories are more complex and accurate models than traditional higher-order theory, introducing shape functions describing shear deformations and stresses through the plate thickness.

Refined higher-order theories are therefore useful for a more accurate and realistic analysis of these structures and can have a significant impact on their behavior in terms of strength, stability, vibrations, deformations…etc [7]. Their displacement field is given by [22]:

$$\begin{cases} u(x,y,z) = u_0(x,y) - z\frac{\partial w}{\partial x} + \varphi(z)\left(\phi_x(x,y) + \frac{\partial w_0}{\partial x}\right) \\ v(x,y,z) = v_0(x,y) - z\frac{\partial w}{\partial y} + \varphi(z)\left(\phi_y(x,y) + \frac{\partial w_0}{\partial y}\right) \\ w(x,y,z) = w_0(x,y) \end{cases} \quad (2\text{-}33)$$

Where: (z) is the shape function driving the distribution of shear strains and stresses across the plate thickness, it is unique to each theory (table 4), and u_0, v_0, w_0, ϕ_x, ϕ_y are the five variables to find (five variables theory)

Classical plate theory (CPT) displacements are obtained by taking $(z) = 0$, while first-order theory (FSDPT) can be obtained by $(z) = z$.

Reddy's model assumes that the membrane displacement field is cubic. This approach is a good approximation for transverse shear stresses compared to the three-dimensional elasticity solution. This makes Reddy's theory frequently the most widely used for the study of plate bending, buckling and vibration.

$$\begin{cases} u(x,y,z) = u_0(x,y) - z\frac{\partial w}{\partial x} + z^3\left(1 - \frac{4}{3h^2}\right)\left(\phi_x(x,y) + \frac{\partial w_0}{\partial x}\right) \\ v(x,y,z) = v_0(x,y) - z\frac{\partial w}{\partial y} + z^3\left(1 - \frac{4}{3h^2}\right)\left(\phi_y(x,y) + \frac{\partial w_0}{\partial y}\right) \\ w(x,y,z) = w_0(x,y) \end{cases} \quad (2\text{-}34)$$

Mahi et al [30] proposed that the distribution of transverse-shear strains and stresses have a hyperbolic shape function, it is variationaly consistent, based on the same assumptions as those of the third-order shear deformation plate theory of Reddy and have five degrees of freedom. It shows a good agreement between analytic results for bending and free vibration compared to the "quasi-3D theory",

Mahi et al displacement field could be written as:

$$\begin{cases} u(x,y,z) = u_0(x,y) - z\frac{\partial w_0}{\partial x} + \left(\frac{h}{2}\tanh\left(\frac{2z}{h}\right) - \frac{4}{3\cosh^2(1)}\left(\frac{z^3}{h^2}\right)\right)\left(\phi_x(x,y) + \frac{\partial w_0}{\partial x}\right) \\ v(x,y,z) = v_0(x,y) - z\frac{\partial w_0}{\partial y} + \left(\frac{h}{2}\tanh\left(\frac{2z}{h}\right) - \frac{4}{3\cosh^2(1)}\left(\frac{z^3}{h^2}\right)\right)\left(\phi_y(x,y) + \frac{\partial w_0}{\partial y}\right) \\ w(x,y,z) = w_0(x,y) \end{cases} \quad (2\text{-}35)$$

Table 4: Different model of shape functions

Theory	Shape function

Mahi [22]	$z\left[1-\alpha\left(\frac{z}{h}\right)^2+\beta\left(\frac{z}{h}\right)^4\right]$
Mantari and Okten &soares [31]	$\tan(\mathrm{mz})+\mathrm{y}^{*}z \;\; ; \;\; \mathrm{y}^{*}=-\mathrm{m}\sec^2(\alpha)\,, \quad m>0, \quad \alpha=m\frac{h}{2}$
Touratier [32]	$\frac{h}{\pi}\sin(\frac{z}{h})$
Ait Atmane [33]	$\frac{\cosh\left(\frac{\pi}{2}\right)}{\cosh\left(\frac{\pi}{2}\right)-1}z-\frac{\frac{h}{\pi}\sinh\frac{\pi z}{h}}{\cosh\left(\frac{\pi}{2}\right)-1}$
El Meiche [34]	$\frac{\frac{h}{\pi}sinh\left(\frac{\pi z}{h}\right)-z}{\cosh\left(\frac{\pi}{z}\right)-1}$
Mahi [30]	$\frac{h}{2}\tanh(\frac{2z}{h})-\frac{4}{3\cosh^2(1)}(\frac{z^3}{h^2})$
Sahoo and singh [35]	$\coth^{-1}(\frac{rh}{z})-\frac{4r}{h(4r^2+1)} \quad ; r=0.46$
Ambartsumian [36]	$\frac{z}{2}\left(\frac{h^2}{4}-\frac{z^2}{3}\right)$
Shimpi [37]	$h\left[\frac{1}{4}\left(\frac{z}{h}\right)-\frac{5}{3}\left(\frac{z}{h}\right)^3\right]$

Shimpi's shape function is used for the displacement field given (four variables refined theory) by,

$$\begin{cases} u(x,y,z)=u_0(x,y)-z\frac{\partial w_b}{\partial x}+\varphi(z)\left(\frac{\partial w_s}{\partial x}\right) \\ v(x,y,z)=v_0(x,y)-z\frac{\partial w_b}{\partial x}+\varphi(z)\left(\frac{\partial w_s}{\partial x}\right) \\ w(x,y,z)=w_{\mathrm{b}}(x,y)+w_{\mathrm{b}}(x,y) \end{cases} \qquad (3\text{-}\mathbf{36})$$

Where:

u_0 and v_0 the membrane displacement in the x and y directions,

w_b and w_s are the deflections of the plate due to shear and bending forces.

3.3.2.2 Laminated theories:

In order to better describe the shear deformation of composite materials, some authors have high order theory with the so-called zig-zag theory to better describe interface effects. Thus, various models derived from the layer approach have been proposed. The multilayer is subdivided into substructures (corresponding to each layer or set of layers). First-order theory or a high-order model is applied to each substructure. The kinematics of zig-zag models satisfy a priori the contact conditions and are independent of the number of layers. The main advantage

of the displacement field of zig-zag models lies in the fact that the distortion of the normal to the deformed surface. This is achieved without increasing the number and order of the fundamental equations of first-order theory. The use of transverse shear correction coefficients is avoided. Based on the concept of Di Sciuva, several authors have made significant improvements to the zig-zag model. The main improvement is the introduction of a non-linear displacement distribution. The zig-zag field (piecewise linear) is superimposed on a high-order displacement field (often cubic) [24].

Compatibility conditions are satisfied on both the top and bottom surfaces of the to reduce the number of parameters,

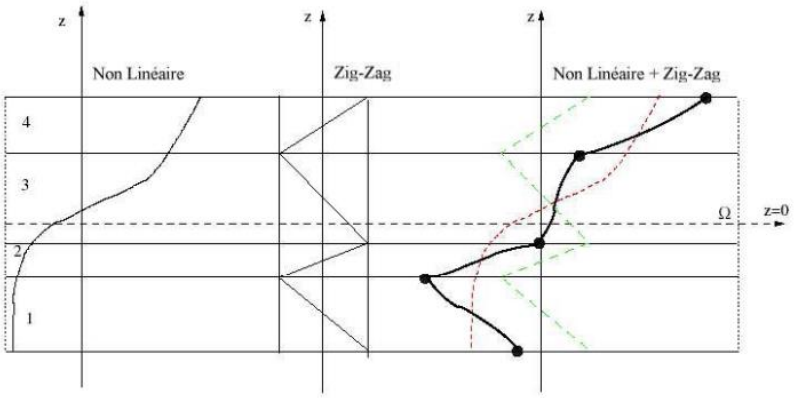

Figure 23: Displacement field of the high-order zig-zag model

3.3.3 Zeroth Order Shear Deformation Theory:

In addition to the high-order theory, a new shear deformation theory has been used to describe the behavior of laminated composite plates, the zeroth-order shear deformation theory (ZSDT) was first proposed by Shimpi and Ray, the zero-order theory accounts for the shear effect without the introduction of shear correction factors, while maintaining a minimum level of complexity to get the solution [24].

The displacement field is given by,

$$\begin{cases} u(x,y,z) = u_0(x,y) - z\dfrac{\partial w}{\partial x} + \dfrac{1}{\lambda_x}\left(\dfrac{3}{2}\left(\dfrac{z}{h}\right) - 2\left(\dfrac{z}{h}\right)^3\right) Q_X \\ v(x,y,z) = v_0(x,y) - z\dfrac{\partial w}{\partial y} + \dfrac{1}{\lambda_y}\left(\dfrac{3}{2}\left(\dfrac{z}{h}\right) - 2\left(\dfrac{z}{h}\right)^3\right) Q_y \\ w(x,y,z) = w_0(x,y) \end{cases} \quad (\mathbf{2\text{-}37})$$

Where:

Q_x and Q_y are the resultants of transverse shear stresses.

λ_x and λ_y are constants that can be determined by considering the definition of the resultants Qx and Qy .

$$Q_x = \int_{-h/2}^{h/2} \tau_{xz}\, dz \quad ; \quad Q_y = \int_{-\frac{h}{2}}^{\frac{h}{2}} \tau_{yz}\, dz \quad (\mathbf{2\text{-}38})$$

4. Conclusion:

The literature research conducted in this chapter has offered crucial models for the analysis of functionally graded materials (FGMs) structures, including plates and beams.

In the field of materials science, functionally graded materials (FGMs) are of great interest due to their unique properties and potential applications. FGMs are composite materials that exhibit a gradual change in composition and/or microstructure across their thickness, resulting in a gradient of properties. This gradient can be designed to achieve specific performance characteristics, such as improved strength, toughness, or thermal conductivity.

To fully understand the properties and behavior of FGMs, it is important to have a comprehensive understanding of the distribution models that can define these materials. (P-FGM), (E-FGM), (S-FGM) are the models allow for a description of how the macrostructural properties of the material change across its thickness, providing insight into how the material will behave under different loading conditions.

On the other hand, microstructural properties, such as the orientation and distribution of reinforcing fibers or particles, can also be characterized using specific distribution models. The Halpin Tsai model and Mori-Tanaka model are commonly used to describe the behavior of filler or reinforcement materials in FGMs. These models take into account the shape, size, and orientation of the reinforcing particles, providing a detailed depiction of the microstructure of the material.

This chapter delves into an in-depth study of the various shear deformation theories of plates, with the primary objective of understanding how to accurately describe the behavior of deformed configurations of functionally graded material (FGM) plates and extract their displacement fields. To begin with, we explore the classical plate theory (CPT) that provides insights into the bending behavior of plates while neglecting the shear effect. However, it is important to note that this theory often leads to imprecise results of the deformed plate because it fails to take into account the shear effect.

In light of this, researchers have developed new deformation theories, such as first-order shear deformation and higher-order shear deformation, to describe the real behavior of deformed plates. These theories are crucial in providing a more accurate representation of the deformation and displacement fields within FGM plates. By incorporating the shear effect, these theories are able to capture the nuances of the deformation process, which would otherwise be overlooked by CPT.

It is worth noting that the use of higher-order shear deformation theories is particularly important in the analysis of FGM plates. This is because the material properties within these plates tend to vary spatially, resulting in non-uniform deformation. As such, higher-order shear deformation theories are better suited to account for the complex deformation patterns that are observed in FGM plates.

CHAPTER 3

ANALYTICAL MODELLING OF AN FGM COMPOSITE PLATE REINFORCED WITH GRAPHENE NANO-PLATELETS

1. Introduction:

In this chapter, we will be going to model an FG-GPLRC (Functionally Graded Graphene-Platelets Reinforced Composite) plate. This will involve various steps that will allow us to accurately describe the behavior of the plate in terms of displacements, deformations, and stresses. To achieve this, we will make use of the theory of Mahi et al, which consists of five variables. By utilizing this model, we will be able to more precisely predict the plate's performance under different conditions.

In addition, we will consider the plate reinforcement with graphene nano-platelets. By employing the Halpin-Tsai model, which is commonly used in the field of composite materials.

Once we have incorporated both the Mahi et al and Halpin-Tsai models, we will derive the governing equations using Hamilton's principal, a fundamental concept in classical mechanics that relates to the principle of least action.

Finally, having derived the motion equations, we will use an analytical method to solve the coupled differential equations system. This will enable us to find the displacement equations of our bending and buckling problem, giving us a complete picture of the plate's behavior. By utilizing these sophisticated models and methods, we'll gain a deeper understanding of the mechanics and properties of FG-GPLRC plates, and ultimately develop better, more resilient materials for a wide range of applications.

2. FG-GPLRC plate modelling:

Consider a rectangular FGM plate of length a, width b and height h. The associated coordinates system is such that the z axis starts from the middle plane and points upwards, and the x and y axes start from one corner with $0 \leq x \leq a$ and $0 \leq y \leq b$. The modeling procedure starts by [38] a uniform distribution of graphene nano-platelets through one phase matrix (epoxy), then gradually adding GPls inclusions,

Adding GPls will enhance stiffness. The new elastic modulus E_m^{GPl} is calculated using the Halpin-Tsai homogenization model, which is expressed as:

$$E_c = {}^{3}/_{8}\, E_{11} + {}^{5}/_{8}\, E_{22} \qquad (\mathbf{3}\text{-}1)$$

$$E_m^{GPl}(z) = {}^{3}/_{8}\frac{1+\xi_L\eta_L Vf}{1-\eta_L Vf}E_m + {}^{5}/_{8}\frac{1+\xi_W\eta_W Vf}{1-\eta_W Vf}E_m \tag{3-2}$$

Where η_L, η_W and take the following expressions,

$$\eta_L = \frac{\left({}^{E_{GPl}}/_{E_m}\right)-1}{\left({}^{E_{GPl}}/_{E_m}\right)+\xi_L} \quad ; \quad \eta_W = \frac{\left({}^{E_{GPl}}/_{E_m}\right)-1}{\left({}^{E_{GPl}}/_{E_m}\right)+\xi_W} \tag{3-3}$$

With:

$$\xi_L = 2\left({}^{l_{GPl}}/_{t_{GPl}}\right) \qquad ; \qquad \xi_W = 2\left({}^{w_{GPl}}/_{t_{GPl}}\right) \tag{3-4}$$

E_m , E_{GPl} are Young's modulus of polymer matrix and graphene nano-platelets respectively

l_{GPl}, w_{GPl}, and t_{GPl} represent the length, width and thickness of GPls, respectively.

ξ_L, ξ_W are the shape parameters of the GPls along longitudinal and transverse directions.

The effective volumetric density ρ_m^{GPl} and Poisson's ratio ν_m^{GPl} are calculated using the rule of mixture between the matrix and GPls:

$$\rho_m^{GPl}(z) = \rho_{GPl}V_{GPl}(z) + \rho_m\left(1 - V_{GPl}(z)\right) \tag{3-5}$$

$$\nu_m^{GPl}(z) = \nu_{GPl}V_{GPl}(z) + \nu_m\left(1 - V_{GPl}(z)\right) \tag{3-6}$$

The shear modulus expression is given by,

$$G_m^{GPl}(z) = \frac{E_m^{GPl}(z)}{2\left(1+\nu_m^{GPl}(z)\right)} \tag{3-7}$$

In which ρ_{GPl} and ν_{GPl} are the corresponding properties of GPls, and V_{GPl} is GPls' volume fraction which varies along the coordinate z in specified patterns. In the present study we use the following variation forms:

$$V_{GPl}(z)=\begin{cases} V_{GPl}^{*} & GPl-UD \\ \begin{cases} 2V_{GPl}^{*}\left(1-\dfrac{2z}{h}\right), & 0\le z\le \dfrac{h}{2} \\ 2V_{GPl}^{*}\left(1-2\dfrac{(h-z)}{h}\right), & \dfrac{h}{2}\le z\le h \end{cases} & GPl-X:\ surface-rich \\ \begin{cases} 2V_{GPl}^{*}\left(1-2\dfrac{\left(\frac{h}{2}-z\right)}{h}\right), & 0\le z\le \dfrac{h}{2} \\ 2V_{GPl}^{*}\left(1+2\dfrac{\left(\frac{h}{2}-z\right)}{h}\right), & \dfrac{h}{2}\le z\le h \end{cases} & GPl-O:\ middle-rich \end{cases} \tag{3-8}$$

Where V_{GPl}^{*} denotes the total (or average) volume fraction of GPls. The volume-fraction V_{GPl}^{*} is not directly measurable, but it can be derived from the weight-fraction A_{GPl} by the relation:

$$V_{GPl}^{*}=\frac{A_{GPl}}{\left(\frac{\rho_{GPl}}{\rho_{m}}\right)(1-A_{GPl})+A_{GPl}} \tag{3-9}$$

In our study, we treat our FG-GPLRC plate as a multilayers plate to make an efficient study comparing our results to the reference [40].

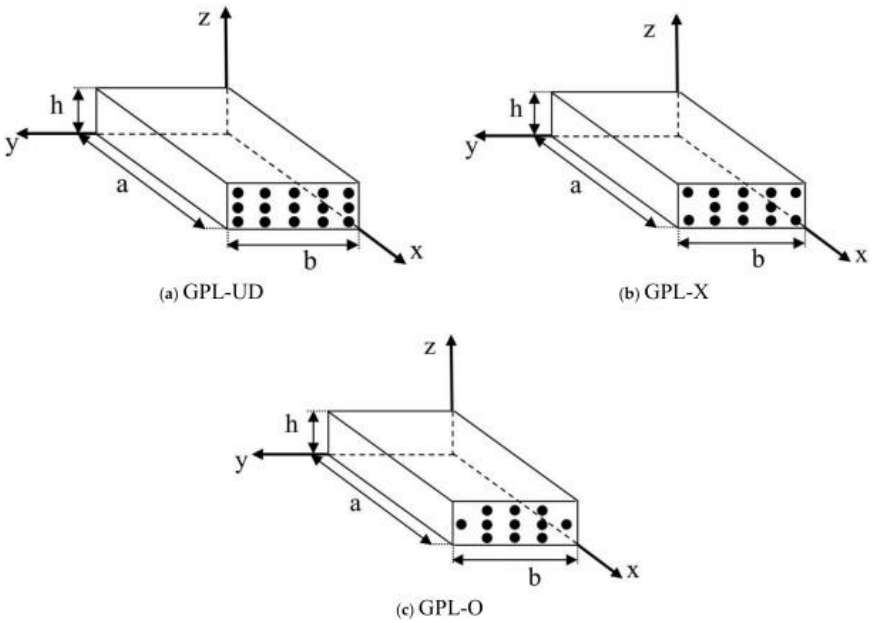

Figure 24: GPls distribution patterns through the plate thickness

3. Derivation of the governing equations of motion:

3.1 Determination of the strain and stress fields:

3.1.1 Displacement, strain and stress fields:

The displacement field of the plate is expressed as:

$$\begin{cases} u(x,y,z) = u_0(x,y) - z\dfrac{\partial w_0}{\partial x} + \varphi(z)\left(\phi_x(x,y) + \dfrac{\partial w_0}{\partial x}\right) \\ v(x,y,z) = v_0(x,y) - z\dfrac{\partial w_0}{\partial y} + \varphi(z)\left(\phi_y(x,y) + \dfrac{\partial w_0}{\partial y}\right) \\ w(x,y,z) = w_0(x,y) \end{cases} \tag{3-10}$$

Where $u_0(x,y)$, $v_0(x,y)$ are the longitudinal displacements at the mid-plane level in the x and y directions, respectively, and $w_0(x,y)$ is the deflection of the plate. $\phi_x(x,y)$ and $\phi_y(x,y)$ denote respectively the total bending rotations around the y and x axes at the mid-plane. $\varphi(z)$ is a generic shape function that determines the distribution of transverse-shear strains and stresses. In the present study we will use the hyperbolic HSDT proposed by Mahi et al:

$$\varphi(z) = \frac{h}{2}\tanh\left(\frac{2z}{h}\right) - \frac{4}{3\cosh^2(1)}\left(\frac{z^3}{h^2}\right) \tag{3-11}$$

As pointed out by Mahi et al [30], the derivative of the shape function ($\varphi'(z)$) features a parabolic variation of transverse stresses and vanishes at z = -h/2 and z = h/2, satisfying the traction-free boundary conditions.

By substituting the displacements of equation (3-10) into the linear strain tensor, defined as:

$$\varepsilon_{ij} = \frac{1}{2}\left(\frac{\partial u_i}{\partial x_i} + \frac{\partial u_j}{\partial x_j}\right) \tag{3-12}$$

$$\begin{cases} \varepsilon_{xx} = \dfrac{\partial u_0}{\partial x} - z\dfrac{\partial^2 w_0}{\partial x^2} + \varphi(z)\left(\dfrac{\partial \phi_x}{\partial x} + \dfrac{\partial^2 w_0}{\partial x^2}\right) \\ \varepsilon_{yy} = \dfrac{\partial v_0}{\partial y} - z\dfrac{\partial^2 w_0}{\partial y^2} + \varphi(z)\left(\dfrac{\partial \phi_y}{\partial y} + \dfrac{\partial^2 w_0}{\partial y^2}\right) \\ \varepsilon_{zz} = 0 \\ \gamma_{xy} = \dfrac{\partial u_0}{\partial y} + \dfrac{\partial v_0}{\partial x} - 2z\dfrac{\partial^2 w_0}{\partial x \partial y} + \varphi(z)\left(\dfrac{\partial \phi_x}{\partial y} + \dfrac{\partial \phi_y}{\partial x} + 2\dfrac{\partial^2 w_0}{\partial x \partial y}\right) \\ \gamma_{xz} = \dfrac{\partial \varphi}{\partial z}\left(\phi_x + \dfrac{\partial w_0}{\partial x}\right) \\ \gamma_{yz} = \dfrac{\partial \varphi}{\partial z}\left(\phi_y + \dfrac{\partial w_0}{\partial y}\right) \end{cases} \tag{3-13}$$

The various stresses acting on a material point are shown in the following figure:

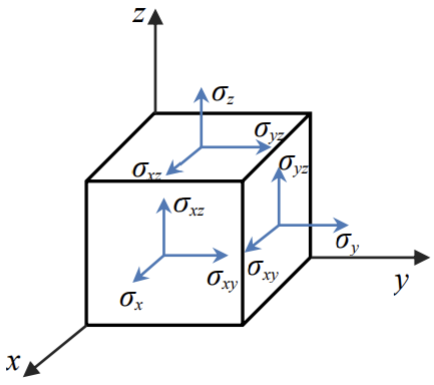

Figure 25: Stress vector components

Stress-strain relations can then be written in the following matrix form:

$$\begin{Bmatrix} \sigma_{xx} \\ \sigma_{yy} \\ \tau_{yz} \\ \tau_{xz} \\ \tau_{xy} \end{Bmatrix} = \begin{bmatrix} Q_{11} & Q_{12} & 0 & 0 & 0 \\ Q_{21} & Q_{22} & 0 & 0 & 0 \\ 0 & 0 & Q_{44} & 0 & 0 \\ 0 & 0 & 0 & Q_{55} & 0 \\ 0 & 0 & 0 & 0 & Q_{66} \end{bmatrix} \begin{Bmatrix} \varepsilon_{xx} \\ \varepsilon_{yy} \\ \gamma_{yz} \\ \gamma_{xz} \\ \gamma_{xy} \end{Bmatrix} \tag{3-14}$$

Where the stiffness coefficients Q_{ij} are given by the following constitutive equations:

$$\begin{cases} Q_{11} = Q_{22} = \dfrac{E(z)}{1-\nu^2(z)} \\ Q_{12} = Q_{21} = \dfrac{\nu(z)E(z)}{1-\nu^2(z)} \\ Q_{44} = Q_{55} = Q_{66} = \dfrac{E(z)}{2\left(1+\nu(z)\right)} \end{cases} \tag{3-15}$$

3.1.2 Constitutive relations :

- **Membrane and shear resultants :**

$$\begin{pmatrix} N_x \\ N_y \\ Q_{xy} \end{pmatrix} = \int_{-h/2}^{h/2} \begin{pmatrix} \sigma_{xx} \\ \sigma_{yy} \\ \sigma_{xy} \end{pmatrix} dz = \int_{-\frac{h}{2}}^{\frac{h}{2}} \begin{pmatrix} Q_{11}\varepsilon_{xx} + Q_{12}\varepsilon_{yy} \\ Q_{12}\varepsilon_{xx} + Q_{22}\varepsilon_{yy} \\ Q_{66}\gamma_{xy} \end{pmatrix} dz \tag{3-16}$$

Where:

N_x, N_y and Q_{xy} are the resultants, per unit length, of the normal stresses (along x and y) and shear stresses in the (x-y) plane, respectively.

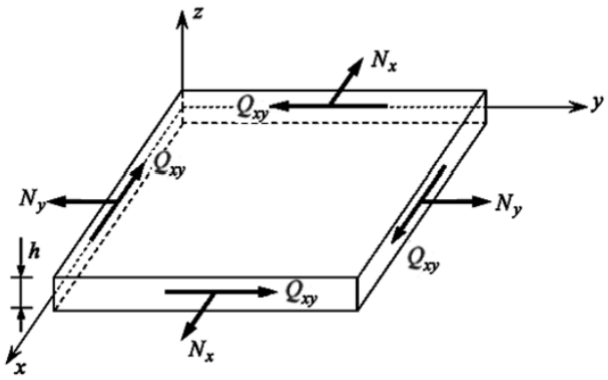

Figure 26: Components of normal and shear forces in the plane.

The higher order shear stresses are written as:

$$\begin{pmatrix} Q_{xz}^{a} \\ Q_{yz}^{a} \end{pmatrix} = \int_{-\frac{h}{2}}^{\frac{h}{2}} \begin{pmatrix} \sigma_{xz} \\ \sigma_{yz} \end{pmatrix} \frac{\partial \varphi}{\partial z} \, dz \tag{3-17}$$

Where:

The components Q_{xz}^{a} and Q_{yz}^{a} are the resultants, per unit length, of the higher order shear stresses of $(x\text{-}z)$ and $(y\text{-}z)$ planes.

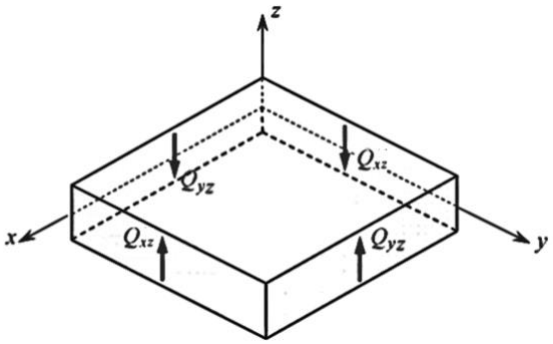

Figure 27: Components of transverse shear stresses

- **Bending and torsion moments :**

$$\begin{pmatrix} M_x \\ M_y \\ M_{xy} \end{pmatrix} = \int_{-\frac{h}{2}}^{\frac{h}{2}} \begin{pmatrix} \sigma_{xx} \\ \sigma_{yy} \\ \sigma_{xy} \end{pmatrix} z\, dz \tag{3-18}$$

M_x and M_y are respectively the bending moments around the y and x axes, and M_{xy} is the torsion moment.

The higher order moments are written as:

$$\begin{pmatrix} M_x^a \\ M_y^a \\ M_{xy}^a \end{pmatrix} = \int_{-\frac{h}{2}}^{\frac{h}{2}} \begin{pmatrix} \sigma_{xx} \\ \sigma_{yy} \\ \sigma_{xy} \end{pmatrix} \varphi(z)\, dz \tag{3-19}$$

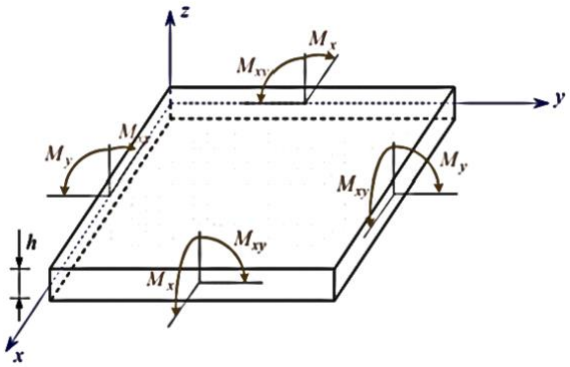

Figure 28: Bending and torsion moment components

M_x^a, M_y^a and M_{xy}^a are the corresponding higher-order bending moments in the x and y directions and the higher-order torsion moment, respectively.

3.1.3 Constitutive equation:

Substituting the expressions of strains (3-13) and stresses (3-14) in the constitutive relations and writing it in the matrix form gives the following constitutive equation:

$$\begin{Bmatrix} N_x \\ N_y \\ M_x \\ M_y \\ M_x^a \\ M_y^a \end{Bmatrix} = \begin{bmatrix} A_{11} & A_{12} & B_{11} & B_{12} & B_{11}^a & B_{12}^a \\ A_{21} & A_{22} & B_{21} & B_{22} & B_{21}^a & B_{22}^a \\ B_{11} & B_{12} & D_{11} & D_{12} & D_{11}^a & D_{12}^a \\ B_{21} & B_{22} & D_{21} & D_{22} & D_{21}^a & D_{22}^a \\ B_{11}^a & B_{12}^a & D_{11}^a & D_{12}^a & D_{11}^{aa} & D_{12}^{aa} \\ B_{21}^a & B_{22}^a & D_{21}^a & D_{22}^a & D_{21}^{aa} & D_{22}^{aa} \end{bmatrix} \begin{Bmatrix} \frac{\partial u_0}{\partial x} \\ \frac{\partial v_0}{\partial y} \\ -\frac{\partial^2 w_0}{\partial x^2} \\ -\frac{\partial^2 w_0}{\partial y^2} \\ \frac{\partial \phi_x}{\partial x} + \frac{\partial^2 w_0}{\partial x^2} \\ \frac{\partial \phi_y}{\partial y} + \frac{\partial^2 w_0}{\partial y^2} \end{Bmatrix} \tag{3-20}$$

$$\begin{Bmatrix} Q_{xy} \\ M_{xy} \\ M_{xy}^a \end{Bmatrix} = \begin{bmatrix} A_{66} & B_{66} & B_{66}^a \\ B_{66} & D_{66} & D_{66}^a \\ B_{66}^a & D_{66}^a & D_{66}^{aa} \end{bmatrix} \begin{Bmatrix} \frac{\partial u_0}{\partial y} + \frac{\partial v_0}{\partial x} \\ -2\frac{\partial^2 w_0}{\partial x \partial y} \\ \frac{\partial \phi_x}{\partial y} + \frac{\partial \phi_y}{\partial x} + 2\frac{\partial^2 w_0}{\partial x \partial y} \end{Bmatrix} \tag{3-21}$$

$$\begin{Bmatrix} Q_{xz}^a \\ Q_{yz}^a \end{Bmatrix} = \begin{bmatrix} A_{55}^a & 0 \\ 0 & A_{44}^a \end{bmatrix} \begin{Bmatrix} \phi_x + \frac{\partial w_0}{\partial x} \\ \phi_y + \frac{\partial w_0}{\partial y} \end{Bmatrix} \tag{3-22}$$

Where the elements of stiffness matrices are defined as:

$$\left(A_{ij}, B_{ij}, B_{ij}^a\right) = \int_{-h/2}^{h/2} Q_{ij}\,(1, z, \varphi)\,dz \qquad i,j = 1,2,6 \tag{3-23}$$

$$\left(D_{ij}, D_{ij}^a, D_{ij}^{aa}\right) = \int_{-h/2}^{h/2} Q_{ij}\,(z^2, z\varphi, \varphi^2)\,dz \qquad i,j = 1,2,6 \tag{3-24}$$

$$A_{ij}^a = \int_{-h/2}^{h/2} Q_{ij}\left(\frac{\partial \varphi}{\partial z}\right)^2 dz \qquad i,j = 4,5 \tag{3-25}$$

A_{ij} coefficients represent the extension stiffness [Pa.m], B_{ij} and B_{ij}^a coefficients represent the (bending-extension) coupling stiffness [Pa.m^2]. D_{ij}, D_{ij}^a & D_{ij}^{aa} coefficients represent the bending stiffness [Pa.m^3]. A_{ij}^a coefficients represent the transverse-shear stiffness [Pa.m] [38].

As pointed out by Mahi et al [30], the transverse-shear stiffness is related to the derivative of the shape function ($\varphi'(z)$) that features a parabolic variation of transverse stresses and vanishes at z = -h/2 and z = h/2, satisfying the traction-free boundary conditions [38].

The coupling and higher-order bending stiffnesses are related to the shape function that has been introduced into the displacement field.

$$
\begin{cases}
N_x = A_{11}\dfrac{\partial u_0}{\partial x} + A_{12}\dfrac{\partial v_0}{\partial y} - B_{11}\dfrac{\partial^2 w_0}{\partial x^2} - B_{12}\dfrac{\partial^2 w_0}{\partial y^2} + B_{11}^{a}\left(\dfrac{\partial \phi_x}{\partial x} + \dfrac{\partial^2 w_0}{\partial x^2}\right) + B_{12}^{a}\left(\dfrac{\partial \phi_y}{\partial y} + \dfrac{\partial^2 w_0}{\partial y^2}\right) \\
N_y = A_{21}\dfrac{\partial u_0}{\partial x} + A_{22}\dfrac{\partial v_0}{\partial y} - B_{21}\dfrac{\partial^2 w_0}{\partial x^2} - B_{22}\dfrac{\partial^2 w_0}{\partial y^2} + B_{21}^{a}\left(\dfrac{\partial \phi_x}{\partial x} + \dfrac{\partial^2 w_0}{\partial x^2}\right) + B_{22}^{a}\left(\dfrac{\partial \phi_y}{\partial y} + \dfrac{\partial^2 w_0}{\partial y^2}\right) \\
M_x = B_{11}\dfrac{\partial u_0}{\partial x} + B_{12}\dfrac{\partial v_0}{\partial y} - D_{11}\dfrac{\partial^2 w_0}{\partial x^2} - D_{12}\dfrac{\partial^2 w_0}{\partial y^2} + D_{11}^{a}\left(\dfrac{\partial \phi_x}{\partial x} + \dfrac{\partial^2 w_0}{\partial x^2}\right) + D_{12}^{a}\left(\dfrac{\partial \phi_y}{\partial y} + \dfrac{\partial^2 w_0}{\partial y^2}\right) \\
M_y = B_{21}\dfrac{\partial u_0}{\partial x} + B_{22}\dfrac{\partial v_0}{\partial y} - D_{21}\dfrac{\partial^2 w_0}{\partial x^2} - D_{22}\dfrac{\partial^2 w_0}{\partial y^2} + D_{21}^{a}\left(\dfrac{\partial \phi_x}{\partial x} + \dfrac{\partial^2 w_0}{\partial x^2}\right) + D_{22}^{a}\left(\dfrac{\partial \phi_y}{\partial y} + \dfrac{\partial^2 w_0}{\partial y^2}\right) \\
M_x^a = B_{11}^{a}\dfrac{\partial u_0}{\partial x} + B_{12}^{a}\dfrac{\partial v_0}{\partial y} - D_{11}^{a}\dfrac{\partial^2 w_0}{\partial x^2} - D_{12}^{a}\dfrac{\partial^2 w_0}{\partial y^2} + D_{11}^{aa}\left(\dfrac{\partial \phi_x}{\partial x} + \dfrac{\partial^2 w_0}{\partial x^2}\right) + D_{12}^{aa}\left(\dfrac{\partial \phi_y}{\partial y} + \dfrac{\partial^2 w_0}{\partial y^2}\right) \\
M_y^a = B_{21}^{a}\dfrac{\partial u_0}{\partial x} + B_{22}^{a}\dfrac{\partial v_0}{\partial y} - D_{21}^{a}\dfrac{\partial^2 w_0}{\partial x^2} - D_{22}^{a}\dfrac{\partial^2 w_0}{\partial y^2} + D_{21}^{aa}\left(\dfrac{\partial \phi_x}{\partial x} + \dfrac{\partial^2 w_0}{\partial x^2}\right) + D_{22}^{aa}\left(\dfrac{\partial \phi_y}{\partial y} + \dfrac{\partial^2 w_0}{\partial y^2}\right) \\
Q_{xy} = \mathrm{A}_{66}\left(\dfrac{\partial u_0}{\partial y} + \dfrac{\partial v_0}{\partial x}\right) - 2\mathrm{B}_{66}\dfrac{\partial^2 w_0}{\partial x \partial y} + \mathrm{B}_{66}^{a}\left(\dfrac{\partial \phi_x}{\partial y} + \dfrac{\partial \phi_y}{\partial x} + 2\dfrac{\partial^2 w_0}{\partial x \partial y}\right) \\
M_{xy} = \mathrm{B}_{66}\left(\dfrac{\partial u_0}{\partial y} + \dfrac{\partial v_0}{\partial x}\right) - 2\mathrm{D}_{66}\dfrac{\partial^2 w_0}{\partial x \partial y} + \mathrm{D}_{66}^{a}\left(\dfrac{\partial \phi_x}{\partial y} + \dfrac{\partial \phi_y}{\partial x} + 2\dfrac{\partial^2 w_0}{\partial x \partial y}\right) \\
\mathrm{M}_{xy}^{a} = \mathrm{B}_{66}^{a}\left(\dfrac{\partial u_0}{\partial y} + \dfrac{\partial v_0}{\partial x}\right) - 2\mathrm{D}_{66}^{a}\dfrac{\partial^2 w_0}{\partial x \partial y} + \mathrm{D}_{66}^{aa}\left(\dfrac{\partial \phi_x}{\partial y} + \dfrac{\partial \phi_y}{\partial x} + 2\dfrac{\partial^2 w_0}{\partial x \partial y}\right) \\
Q_{xz}^{a} = \mathrm{A}_{55}^{a}\left(\phi_x + \dfrac{\partial w_0}{\partial x}\right) \\
Q_{yz}^{a} = \mathrm{A}_{44}^{a}\left(\phi_y + \dfrac{\partial w_0}{\partial y}\right)
\end{cases}
\quad (3\text{-}\mathbf{26})
$$

3.1.4 External loads modelling:

In an elasticity problem, a plate subjected to transverse loads at the upper surface (along x and y) where these loads can be sinusoidal or have any other form of intensity distribution (x, y), must be able to withstand these loads. In other words, the plate reacts in such a way that it can maintain equilibrium in each of its elements. **Figure 29** illustrates the general case of an element of a plate in equilibrium.

The buckling model is presented in **Figure 30**, which has the ability to detect the critical buckling load of an FGM plate under distributed pre-buckling forces (Px, Py), knowing that:

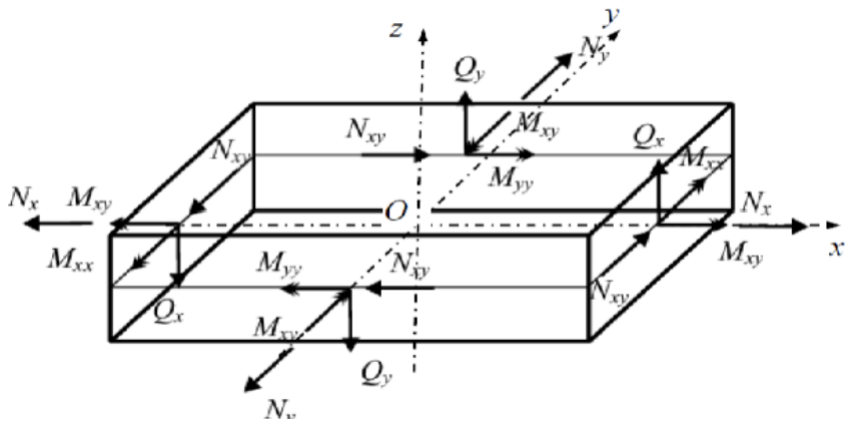

Figure 29: Internal loads

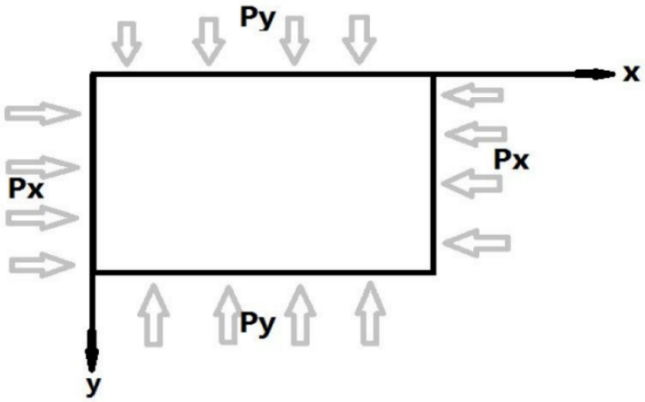

Figure 30: Pre-buckling compression load distribution

3.2 Energetic formulation of composite plate reinforced with graphene nano-platelets:

3.2.1 Kinetic energy:

The kinetic energy of the FGM plate is given by:

$$E_k = \frac{1}{2}\iiint \rho(z)\frac{\partial u_i}{\partial t}\frac{\partial u_j}{\partial t}dv = \frac{1}{2}\iint \int_{-h/2}^{h/2} \rho(z)\left[\frac{\partial u}{\partial t}^2 + \frac{\partial v}{\partial t}^2 + \frac{\partial w}{\partial t}^2\right]dz\ dA \quad (3\text{-}27)$$

3.2.2 Strain energy:

The mathematical expression of the strain energy, also known as potential or elastic energy due to the elastic deformation of a solid, is as follows:

$$E_U = \frac{1}{2}\iiint \sigma_{ij}\varepsilon_{ij}\,dv \qquad i,j = x,y,z \quad (3\text{-}28)$$

$$= \frac{1}{2}\iint \int_{-\frac{h}{2}}^{\frac{h}{2}} \sigma_{xx}\varepsilon_{xx} + \sigma_{yy}\varepsilon_{yy} + \sigma_{yz}\gamma_{yz} + \sigma_{xz}\gamma_{xz} + \sigma_{xy}\gamma_{xy}\,dz\,dA = \sum_{i=1}^{5} E_U^i$$

$$E_U^1 = \frac{1}{2}\iiint \sigma_{xx}\varepsilon_{xx}\,dv = \frac{1}{2}\iint \left[N_x\frac{\partial u_0}{\partial x} - M_x\frac{\partial^2 w_0}{\partial x^2} + M_x^a\left(\frac{\partial \phi_x}{\partial x} + \frac{\partial^2 w_0}{\partial x^2}\right)\right]dA \quad (3\text{-}29)$$

$$E_U^2 = \frac{1}{2}\iiint \sigma_{yy}\varepsilon_{yy}\,dv = \frac{1}{2}\iint \left[N_y\frac{\partial v_0}{\partial y} - M_y\frac{\partial^2 w_0}{\partial y^2} + M_y^a\left(\frac{\partial \phi_y}{\partial y} + \frac{\partial^2 w_0}{\partial y^2}\right)\right]dA \quad (3\text{-}30)$$

$$E_U^3 = \frac{1}{2}\iiint \sigma_{xz}\gamma_{xz}dv = \frac{1}{2}\iint \left[Q_{xz}^a\left(\phi_x + \frac{\partial w_0}{\partial x}\right)\right]dA \quad (3\text{-}31)$$

$$E_U^4 = \frac{1}{2}\iiint \sigma_{yz}\gamma_{yz}dv = \frac{1}{2}\iint \left[Q_{yz}^a\left(\phi_y + \frac{\partial w_0}{\partial y}\right)\right]dA \quad (3\text{-}32)$$

$$E_U^5 = \frac{1}{2}\iiint \sigma_{xy}\gamma_{xy}\,dv$$
$$= \frac{1}{2}\iint \left[Q_{xy}\left(\frac{\partial u_0}{\partial y} + \frac{\partial v_0}{\partial x}\right) - 2M_{xy}\frac{\partial^2 w_0}{\partial x \partial y} + M_{xy}^a\left(\frac{\partial \phi_x}{\partial y} + \frac{\partial \phi_y}{\partial x} + 2\frac{\partial^2 w_0}{\partial x \partial y}\right)\right]dA \quad (3\text{-}33)$$

3.2.2.1 Strain energy variation:

The variation in strain energy is derived from equation (3-28) and is given as:

$$\delta E_U = \iiint \sigma_{ij}\delta\varepsilon_{ij}\,dv \quad (3\text{-}34)$$

$$\delta E_U = \delta E_U^1 + \delta E_U^2 + \delta E_U^3 + \delta E_U^4 + \delta E_U^5 \quad (3\text{-}35)$$

$$\delta E_U = \iint \left[N_x \delta\left(\frac{\partial u_0}{\partial x}\right) - M_x \delta\left(\frac{\partial^2 w_0}{\partial x^2}\right) + M_x^a \delta\left(\frac{\partial \phi_x}{\partial x}\right) + M_x^a \delta\left(\frac{\partial^2 w_0}{\partial x^2}\right) + N_y \delta\left(\frac{\partial v_0}{\partial y}\right) \right.$$
$$- M_y \delta\left(\frac{\partial^2 w_0}{\partial y^2}\right) + M_y^a \delta\left(\frac{\partial \phi_y}{\partial y}\right) + M_y^a \delta\left(\frac{\partial^2 w_0}{\partial y^2}\right) + Q_{xz}^a \delta\phi_x + Q_{xz}^a \delta\left(\frac{\partial w_0}{\partial x}\right)$$
$$+ Q_{yz}^a \delta\phi_y + Q_{yz}^a \delta\left(\frac{\partial w_0}{\partial y}\right) + Q_{xy} \delta\left(\frac{\partial u_0}{\partial y}\right) + Q_{xy} \delta\left(\frac{\partial v_0}{\partial x}\right) - 2M_{xy} \delta\left(\frac{\partial^2 w_0}{\partial x \partial y}\right)$$
$$\left. + M_{xy}^a \delta\left(\frac{\partial \phi_x}{\partial y}\right) + M_{xy}^a \delta\left(\frac{\partial \phi_y}{\partial x}\right) + 2M_{xy}^a \delta\left(\frac{\partial^2 w_0}{\partial x \partial y}\right) \right] dA \quad (3\text{-}36)$$

By integrating by part, we find:

$$\delta E_U = \iint \left[-\frac{\partial N_x}{\partial x}\delta u_0 - \frac{\partial^2 M_x}{\partial x^2}\delta w_0 - \frac{\partial M_x^a}{\partial x}\delta\phi_x + \frac{\partial^2 M_x^a}{\partial x^2}\delta w_0 - \frac{\partial N_y}{\partial y}\delta v_0 - \frac{\partial^2 M_y}{\partial y^2}\delta w_0 \right.$$
$$- \frac{\partial M_y^a}{\partial y}\delta\phi_y + \frac{\partial^2 M_y^a}{\partial y^2}\delta w_0 + Q_{xz}^a \delta\phi_x - \frac{\partial Q_{xz}^a}{\partial x}\delta w_0 + Q_{yz}^a \delta\phi_y - \frac{\partial Q_{yz}^a}{\partial y}\delta w_0$$
$$- \frac{\partial Q_{xy}}{\partial y}\delta u_0 - \frac{\partial Q_{xy}}{\partial x}\delta v_0 - 2\frac{\partial^2 M_{xy}}{\partial x \partial y}\delta w_0 - \frac{\partial M_{xy}^a}{\partial y}\delta\phi_x - \frac{\partial M_{xy}^a}{\partial x}\delta\phi_y$$
$$\left. + 2\frac{\partial^2 M_{xy}^a}{\partial x \partial y}\delta w_0 \right] dA \quad (3\text{-}37)$$

The contributions of the source terms of the strain energy related to the variations δu_0, δv_0, δw_0, $\delta\phi_x$, $\delta\phi_y$ are:

$$\boldsymbol{\delta u_0}: -\frac{\partial N_x}{\partial x} - \frac{\partial Q_{xy}}{\partial y}$$

$$\boldsymbol{\delta v_0}: -\frac{\partial N_y}{\partial y} - \frac{\partial Q_{xy}}{\partial x} \quad (3\text{-}38)$$

$$\boldsymbol{\delta w_0}: -\frac{\partial^2 M_x}{\partial x^2} + \frac{\partial^2 M_x^a}{\partial x^2} - \frac{\partial^2 M_y}{\partial y^2} + \frac{\partial^2 M_y^a}{\partial y^2} - \frac{\partial Q_{xz}^a}{\partial x} - \frac{\partial Q_{yz}^a}{\partial y} - 2\frac{\partial^2 M_{xy}}{\partial x \partial y} + 2\frac{\partial^2 M_{xy}^a}{\partial x \partial y}$$

$$\boldsymbol{\delta\phi_x}: -\frac{\partial M_x^a}{\partial x} + Q_{xz}^a - \frac{\partial M_{xy}^a}{\partial y}$$

$$\boldsymbol{\delta\phi_y}: -\frac{\partial M_y^a}{\partial y} + Q_{yz}^a - \frac{\partial M_{xy}^a}{\partial x}$$

3.2.3 Work of external loads:

3.2.3.1 Virtual work:

The work done by the distributed transverse load (q) and edge loads (P_x and P_y) as a virtual form is expressed as follows:

$$\delta W = -\iint [q\delta w_0]\, dxdy + \iint \left[P_x \frac{\partial w_0}{\partial x}\delta\left(\frac{\partial w_0}{\partial x}\right) + P_y \frac{\partial w_0}{\partial y}\delta\left(\frac{\partial w_0}{\partial y}\right)\right] dxdy \qquad (3\text{-}39)$$

By integrating by part, we find:

$$\delta W = -\iint [q\delta w_0]\, dxdy + \iint \left[-P_x \frac{\partial^2 w_0}{\partial x^2}\delta w_0 - P_y \frac{\partial^2 w_0}{\partial y^2}\delta w_0\right] dxdy \qquad (3\text{-}40)$$

Where:

$$\begin{cases} \mathrm{P}_x = \lambda_1 \mathrm{P}_{cr} \\ \mathrm{P}_y = \lambda_2 \mathrm{P}_{cr} \end{cases}$$

λ_1 and λ_2 are the buckling parameters and $\mathrm{P_{cr}}$ is the critical buckling load.

The contribution of the source term of the virtual work related to δw_0 variation is:

$$\boldsymbol{\delta w_0}: -q - P_x \frac{\partial^2 w_0}{\partial x^2} - P_y \frac{\partial^2 w_0}{\partial y^2} \qquad (3\text{-}41)$$

3.2.4 Hamilton's principle:

The variational principle is used to obtain the equilibrium equations of the FG-GPLRC plates which state that:

$$\delta\,(E_U + W) = 0 \qquad (3\text{-}42)$$

Where E_U and W are the strain energy and potential energy (work) of the applied (external) loads, respectively.

This variational principle that applies to static problem ($E_k = 0$) can be derived from Hamilton's Principle applicable to dynamic problems:

$$0 = \int_0^t (\delta E_U + \delta W - \delta E_k)\, dt \qquad (3\text{-}43)$$

3.2.5 Equilibrium equations:

From the contributions of strain energy and the virtual work to the variations δu_0, δv_0, δw_0, $\delta \phi_x$, $\delta \phi_y$ and by applying Hamilton's principle, we can derive the equations governing the motion of the FGM plate reinforced with graphene nano-platelets.

$$\boldsymbol{\delta u_0}: \frac{\partial N_x}{\partial x} + \frac{\partial Q_{xy}}{\partial y} = 0$$

$$\boldsymbol{\delta v_0}: \frac{\partial N_y}{\partial y} + \frac{\partial Q_{xy}}{\partial x} = 0 \tag{3-44}$$

$$\boldsymbol{\delta w_0}: \frac{\partial^2 M_x}{\partial x^2} - \frac{\partial^2 M_x^a}{\partial x^2} + \frac{\partial^2 M_y}{\partial y^2} - \frac{\partial^2 M_y^a}{\partial y^2} + \frac{\partial Q_{xz}^a}{\partial x} + \frac{\partial Q_{yz}^a}{\partial y} + 2\frac{\partial^2 M_{xy}}{\partial x \partial y} - 2\frac{\partial^2 M_{xy}^a}{\partial x \partial y} + q + P_x \frac{\partial^2 w_0}{\partial x^2} + P_y \frac{\partial^2 w_0}{\partial y^2} = 0$$

$$\boldsymbol{\delta \phi_x}: \frac{\partial M_x^a}{\partial x} - Q_{xz}^a + \frac{\partial M_{xy}^a}{\partial y} = 0$$

$$\boldsymbol{\delta \phi_y}: \frac{\partial M_y^a}{\partial y} - Q_{yz}^a + \frac{\partial M_{xy}^a}{\partial x} = 0$$

In order to solve these equations, it is advisable express them to the generalized displacements δu_0, δv_0, δw_0, $\delta \phi_x$ and $\delta \phi_y$ by replacing the forces and moments with their expressions obtained from the constitutive equation.

$$\boldsymbol{\delta u_0}: A_{11}\frac{\partial^2 u_0}{\partial x^2} + A_{12}\frac{\partial^2 v_0}{\partial x \partial y} - B_{11}\frac{\partial^3 w_0}{\partial x^3} - B_{12}\frac{\partial^3 w_0}{\partial x \partial y^2} + B_{11}^a\left(\frac{\partial^2 \phi_x}{\partial x^2} + \frac{\partial^3 w_0}{\partial x^3}\right) + B_{12}^a\left(\frac{\partial^2 \phi_y}{\partial x \partial y} + \frac{\partial^3 w_0}{\partial x \partial y^2}\right) + \mathrm{A}_{66}\left(\frac{\partial^2 u_0}{\partial y^2} + \frac{\partial^2 v_0}{\partial y \partial x}\right) - 2\mathrm{B}_{66}\frac{\partial^3 w_0}{\partial x \partial y^2} + \mathrm{B}_{66}^{\mathrm{a}}\left(\frac{\partial^2 \phi_x}{\partial y^2} + \frac{\partial^2 \phi_y}{\partial x \partial y} + 2\frac{\partial^3 w_0}{\partial x \partial y^2}\right) = 0$$

$$\boldsymbol{\delta v_0}: A_{21}\frac{\partial^2 u_0}{\partial x \partial y} + A_{22}\frac{\partial^2 v_0}{\partial y^2} - B_{21}\frac{\partial^3 w_0}{\partial x^2 \partial y} - B_{22}\frac{\partial^3 w_0}{\partial y^3} + B_{21}^a\left(\frac{\partial^2 \phi_x}{\partial x \partial y} + \frac{\partial^3 w_0}{\partial x^2 \partial y}\right) + B_{22}^a\left(\frac{\partial^2 \phi_y}{\partial y^2} + \frac{\partial^3 w_0}{\partial y^3}\right) + A_{66}\left(\frac{\partial^2 u_0}{\partial x \partial y} + \frac{\partial^2 v_0}{\partial x^2}\right) - 2B_{66}\frac{\partial^3 w_0}{\partial x^2 \partial y} + B_{66}^a\left(\frac{\partial^2 \phi_x}{\partial x \partial y} + \frac{\partial^2 \phi_y}{\partial x^2} + 2\frac{\partial^3 w_0}{\partial x^2 \partial y}\right) = 0 \tag{3-45}$$

$$\boldsymbol{\delta w_0}: (B_{11}-B_{11}^a)\frac{\partial^3 u_0}{\partial x^3}+(B_{12}-B_{12}^a)\frac{\partial^3 v_0}{\partial x^2\partial y}-(D_{11}-D_{11}^a)\frac{\partial^4 w_0}{\partial x^4}-(D_{12}-D_{12}^a)\frac{\partial^4 w_0}{\partial x^2\partial y^2}$$
$$+(D_{11}^a-D_{11}^{aa})\left(\frac{\partial^3\phi_x}{\partial x^3}+\frac{\partial^4 w_0}{\partial x^4}\right)+(D_{12}^a-D_{12}^{aa})\left(\frac{\partial^3\phi_y}{\partial x^2\partial y}+\frac{\partial^4 w_0}{\partial x^2\partial y^2}\right)+(B_{21}$$
$$-B_{21}^a)\frac{\partial^3 u_0}{\partial x\partial y^2}+(B_{22}-B_{22}^a)\frac{\partial^3 v_0}{\partial y^3}-(D_{21}-D_{21}^a)\frac{\partial^4 w_0}{\partial x^2\partial y^2}+(D_{21}^a$$
$$-D_{21}^{aa})\left(\frac{\partial^3\phi_x}{\partial x\partial y^2}+\frac{\partial^4 w_0}{\partial x^2\partial y^2}\right)+(D_{22}^a-D_{22}^{aa})\left(\frac{\partial^3\phi_y}{\partial y^3}+\frac{\partial^4 w_0}{\partial y^4}\right)-(D_{22}$$
$$-D_{22}^a)\frac{\partial^4 w_0}{\partial y^4}+\mathrm{A}_{55}^a\left(\frac{\partial\phi_x}{\partial x}+\frac{\partial^2 w_0}{\partial x^2}\right)+\mathrm{A}_{44}^a\left(\frac{\partial\phi_y}{\partial y}+\frac{\partial^2 w_0}{\partial y^2}\right)+2(\mathrm{B}_{66}$$
$$-\mathrm{B}_{66}^{\mathrm{a}})\left(\frac{\partial^3 u_0}{\partial x\partial y^2}+\frac{\partial^3 v_0}{\partial x^2\partial y}\right)-4(\mathrm{D}_{66}-\mathrm{D}_{66}^{\mathrm{a}})\frac{\partial^4 w_0}{\partial x^2\partial y^2}+2(\mathrm{D}_{66}^{\mathrm{a}}$$
$$-\mathrm{D}_{66}^{\mathrm{aa}})\left(\frac{\partial^3\phi_x}{\partial x\partial y^2}+\frac{\partial^3\phi_y}{\partial x^2\partial y}+2\frac{\partial^4 w_0}{\partial x^2\partial y^2}\right)$$
$$-2\mathrm{D}_{66}^{\mathrm{aa}}\left(\frac{\partial^3\phi_x}{\partial x\partial y^2}+\frac{\partial^3\phi_y}{\partial x^2\partial y}+2\frac{\partial^4 w_0}{\partial x^2\partial y^2}\right)+q+P_x\frac{\partial^2 w_0}{\partial x^2}+P_y\frac{\partial^2 w_0}{\partial y^2}=0$$

$$\boldsymbol{\delta\phi_x}: B_{11}^a\frac{\partial^2 u_0}{\partial x^2}+B_{12}^a\frac{\partial^2 v_0}{\partial x\partial y}-D_{11}^a\frac{\partial^3 w_0}{\partial x^3}-D_{12}^a\frac{\partial^3 w_0}{\partial x\partial y^2}+D_{11}^{aa}\left(\frac{\partial^2\phi_x}{\partial x^2}+\frac{\partial^3 w_0}{\partial x^3}\right)$$
$$+D_{12}^{aa}\left(\frac{\partial^2\phi_y}{\partial x\partial y}+\frac{\partial^3 w_0}{\partial x\partial y^2}\right)-\mathrm{A}_{55}^a\left(\phi_x+\frac{\partial w_0}{\partial x}\right)+\mathrm{B}_{66}^{\mathrm{a}}\left(\frac{\partial^2 u_0}{\partial y^2}+\frac{\partial^2 v_0}{\partial y\partial x}\right)$$
$$-2\mathrm{D}_{66}^{\mathrm{a}}\frac{\partial^3 w_0}{\partial x\partial y^2}+\mathrm{D}_{66}^{\mathrm{aa}}\left(\frac{\partial^2\phi_x}{\partial y^2}+\frac{\partial^2\phi_y}{\partial x\partial y}+2\frac{\partial^3 w_0}{\partial x\partial y^2}\right)=0$$

$$\boldsymbol{\delta\phi_y}: B_{21}^a\frac{\partial^2 u_0}{\partial x\partial y}+B_{22}^a\frac{\partial^2 v_0}{\partial y^2}-D_{21}^a\frac{\partial^3 w_0}{\partial x^2\partial y}-D_{22}^a\frac{\partial^3 w_0}{\partial y^3}+D_{21}^{aa}\left(\frac{\partial^2\phi_x}{\partial x\partial y}+\frac{\partial^3 w_0}{\partial x^2\partial y}\right)$$
$$+D_{22}^{aa}\left(\frac{\partial^2\phi_y}{\partial y^2}+\frac{\partial^3 w_0}{\partial y^3}\right)-\mathrm{A}_{44}^a\left(\phi_y+\frac{\partial w_0}{\partial y}\right)+\mathrm{B}_{66}^{\mathrm{a}}\left(\frac{\partial^2 u_0}{\partial x\partial y}+\frac{\partial^2 v_0}{\partial x^2}\right)$$
$$-2\mathrm{D}_{66}^{\mathrm{a}}\frac{\partial^3 w_0}{\partial x^2\partial y}+\mathrm{D}_{66}^{\mathrm{aa}}\left(\frac{\partial^2\phi_x}{\partial x\partial y}+\frac{\partial^2\phi_y}{\partial x^2}+2\frac{\partial^3 w_0}{\partial x^2\partial y}\right)=0$$

The equations **(3-45)** describe five fourth-order linear partial differential equations in terms of the five generalized displacements.

3.3 Fundamental bending relations:

Taking into account the transverse load and eliminating edge loads, the fundamental bending relations are described as follows:

$$\begin{cases} q \neq 0 \\ P_x = P_y = 0 \end{cases} \tag{3-46}$$

The fundamental bending relations are given by equations (3-47). The relation corresponding to δw_0 being modified as follows:

$$\begin{aligned} &\boldsymbol{\delta w_0}: (B_{11} - B_{11}^a)\frac{\partial^3 u_0}{\partial x^3} + (B_{12} - B_{12}^a)\frac{\partial^3 v_0}{\partial x^2 \partial y} - (D_{11} - D_{11}^a)\frac{\partial^4 w_0}{\partial x^4} - (D_{12} - D_{12}^a)\frac{\partial^4 w_0}{\partial x^2 \partial y^2} \\ &+ (D_{11}^a - D_{11}^{aa})\left(\frac{\partial^3 \phi_x}{\partial x^3} + \frac{\partial^4 w_0}{\partial x^4}\right) + (D_{12}^a - D_{12}^{aa})\left(\frac{\partial^3 \phi_y}{\partial x^2 \partial y} + \frac{\partial^4 w_0}{\partial x^2 \partial y^2}\right) + (B_{21} - B_{21}^a)\frac{\partial^3 u_0}{\partial x \partial y^2} \\ &+ (B_{22} - B_{22}^a)\frac{\partial^3 v_0}{\partial y^3} - (D_{21} - D_{21}^a)\frac{\partial^4 w_0}{\partial x^2 \partial y^2} + (D_{21}^a - D_{21}^{aa})\left(\frac{\partial^3 \phi_x}{\partial x \partial y^2} + \frac{\partial^4 w_0}{\partial x^2 \partial y^2}\right) + (D_{22}^a \\ &- D_{22}^{aa})\left(\frac{\partial^3 \phi_y}{\partial y^3} + \frac{\partial^4 w_0}{\partial y^4}\right) - (D_{22} - D_{22}^a)\frac{\partial^4 w_0}{\partial y^4} + A_{55}^a\left(\frac{\partial \phi_x}{\partial x} + \frac{\partial^2 w_0}{\partial x^2}\right) + A_{44}^a\left(\frac{\partial \phi_y}{\partial y} + \frac{\partial^2 w_0}{\partial y^2}\right) \\ &+ 2(B_{66} - B_{66}^a)\left(\frac{\partial^3 u_0}{\partial x \partial y^2} + \frac{\partial^3 v_0}{\partial x^2 \partial y}\right) - 4(D_{66} - D_{66}^a)\frac{\partial^4 w_0}{\partial x^2 \partial y^2} + 2(D_{66}^a \\ &- D_{66}^{aa})\left(\frac{\partial^3 \phi_x}{\partial x \partial y^2} + \frac{\partial^3 \phi_y}{\partial x^2 \partial y} + 2\frac{\partial^4 w_0}{\partial x^2 \partial y^2}\right) - 2D_{66}^{aa}\left(\frac{\partial^3 \phi_x}{\partial x \partial y^2} + \frac{\partial^3 \phi_y}{\partial x^2 \partial y} + 2\frac{\partial^4 w_0}{\partial x^2 \partial y^2}\right) + q \\ &= 0 \end{aligned} \tag{3-47}$$

3.4 Fundamental buckling relations:

Taking into account the edge loads and eliminating transverse load, the fundamental buckling relations are described by the following expressions:

$$\begin{cases} q = 0 \\ P_x = \lambda_1 P_{cr} \\ P_y = \lambda_2 P_{cr} \end{cases} \tag{3-48}$$

Where:

$\lambda_1$and λ_2 are the buckling parameters:

- Uni-axial buckling (along the x-axis): $\lambda_1 \neq 0$ and $\lambda_2 = 0$.
- Uni-axial buckling (along the y-axis): $\lambda_1 = 0$ and $\lambda_2 \neq 0$.
- Bi- axial buckling (along x and y axis): $\lambda_1 \neq 0$ and $\lambda_2 \neq 0$.

The fundamental buckling relations are given by (3-48) relations. The relation corresponding to δw_0 being modified as follows:

$$\boldsymbol{\delta w_0}: (B_{11}-B_{11}^a)\frac{\partial^3 u_0}{\partial x^3}+(B_{12}-B_{12}^a)\frac{\partial^3 v_0}{\partial x^2\partial y}-(D_{11}-D_{11}^a)\frac{\partial^4 w_0}{\partial x^4}-(D_{12}-D_{12}^a)\frac{\partial^4 w_0}{\partial x^2\partial y^2}+(D_{11}^a - D_{11}^{aa})\left(\frac{\partial^3\phi_x}{\partial x^3}+\frac{\partial^4 w_0}{\partial x^4}\right)+(D_{12}^a-D_{12}^{aa})\left(\frac{\partial^3\phi_y}{\partial x^2\partial y}+\frac{\partial^4 w_0}{\partial x^2\partial y^2}\right)+(B_{21}-B_{21}^a)\frac{\partial^3 u_0}{\partial x\partial y^2}+(B_{22}-B_{22}^a)\frac{\partial^3 v_0}{\partial y^3}-(D_{21}-D_{21}^a)\frac{\partial^4 w_0}{\partial x^2\partial y^2}+(D_{21}^a-D_{21}^{aa})\left(\frac{\partial^3\phi_x}{\partial x\partial y^2}+\frac{\partial^4 w_0}{\partial x^2\partial y^2}\right)+(D_{22}^a-D_{22}^{aa})\left(\frac{\partial^3\phi_y}{\partial y^3}+\frac{\partial^4 w_0}{\partial y^4}\right)-(D_{22}-D_{22}^a)\frac{\partial^4 w_0}{\partial y^4}+A_{55}^a\left(\frac{\partial\phi_x}{\partial x}+\frac{\partial^2 w_0}{\partial x^2}\right)+A_{44}^a\left(\frac{\partial\phi_y}{\partial y}+\frac{\partial^2 w_0}{\partial y^2}\right)+2(B_{66}-B_{66}^a)\left(\frac{\partial^3 u_0}{\partial x\partial y^2}+\frac{\partial^3 v_0}{\partial x^2\partial y}\right)-4(D_{66}-D_{66}^a)\frac{\partial^4 w_0}{\partial x^2\partial y^2}+2(D_{66}^a-D_{66}^{aa})\left(\frac{\partial^3\phi_x}{\partial x\partial y^2}+\frac{\partial^3\phi_y}{\partial x^2\partial y}+2\frac{\partial^4 w_0}{\partial x^2\partial y^2}\right)-2D_{66}^{aa}\left(\frac{\partial^3\phi_x}{\partial x\partial y^2}+\frac{\partial^3\phi_y}{\partial x^2\partial y}+2\frac{\partial^4 w_0}{\partial x^2\partial y^2}\right)+P_{cr}(\lambda_1\frac{\partial^2 w_0}{\partial x^2}+\lambda_2\frac{\partial^2 w_0}{\partial y^2})=0 \quad (3\text{-}49)$$

4. Analytical solution of motion equations:

4.1 Boundary conditions and Navier solution:

The analysis of a rectangular plate requires the solution of the governing equation, along with appropriate boundary conditions at the four edges, to yield the deflection function w(x, y). Once this is carried out, the strains and stresses at any point of the plate structure can be obtained. The basic idea behind Navier's method is to seek the solution for w in the form of an infinite series such that the edge conditions are satisfied a priori, and the governing differential equations are reduced to simple algebraic equations for a simply supported plate (SSSS) [39].

Any transverse mechanical load $q(x, y)$ applied to the plate can also be expanded into Fourier series in order to obtain:

$$q(x,y)=\sum_{m=1}^{\infty}\sum_{n=1}^{\infty}Q_{mn}\,sin(\alpha x)\,sin(\beta y) \quad (3\text{-}50)$$

The boundary conditions along the edges of a simply supported plate can be written as follows:

$$u_0(x,0)=0 \quad ; \quad u_0(x,b)=0 \quad ; \quad v_0(0,y)=0 \quad ; \quad v_0(a,y)=0$$

$$\begin{aligned}
&w_0(x,0)=0 \quad ; \quad w_0(x,b)=0 \quad ; \quad w_0(0,y)=0 \quad ; \quad w_0(a,y)=0 \\
&\phi_x(x,0)=0 \quad ; \quad \phi_x(x,b)=0 \quad ; \quad \phi_y(0,y)=0 \quad ; \quad \phi_y(a,y)=0 \\
&M_x(x,0)=0 \quad ; \quad M_x(x,b)=0 \quad ; \quad M_y(0,y)=0 \quad ; \quad M_y(a,y)=0 \\
&N_x(x,0)=0 \quad ; \quad N_x(x,b)=0 \quad ; \quad N_y(0,y)=0 \quad ; \quad N_y(a,y)=0 \\
&M_x^a(x,0)=0 \quad ; \quad M_x^a(x,b)=0 \quad ; \quad M_y^a(0,y)=0 \quad ; \quad M_y^a(a,y)=0
\end{aligned} \tag{3-51}$$

The displacement functions that satisfy these boundary conditions are represented in the form of double Fourier series:

$$\begin{aligned}
U(x,y) &= \sum_{m=1}^{\infty}\sum_{n=1}^{\infty} J_{mn}\, cos(\alpha x)\, sin(\beta y) \\
V(x,y) &= \sum_{m=1}^{\infty}\sum_{n=1}^{\infty} K_{mn}\, sin(\alpha x)\, cos(\beta y) \\
W(x,y) &= \sum_{m=1}^{\infty}\sum_{n=1}^{\infty} L_{mn}\, sin(\alpha x)\, sin(\beta y) \\
\phi_x(x,y) &= \sum_{m=1}^{\infty}\sum_{n=1}^{\infty} M_{mn}\, cos(\alpha x)\, sin(\beta y) \\
\phi_y(x,y) &= \sum_{m=1}^{\infty}\sum_{n=1}^{\infty} N_{mn}\, sin(\alpha x)\, cos(\beta y)
\end{aligned} \tag{3-52}$$

Where:

J_{mn}, K_{mn}, L_{mn}, M_{mn} and N_{mn} are the unknown amplitudes parameters,

$$\alpha = \frac{m\pi}{a} \text{ and } \beta = \frac{n\pi}{b} \tag{3-53}$$

For a sinusoidal load distribution, Q_{mn} simplifies to:

$$Q_{mn} = q_0 \tag{3-54}$$

Where:

q_0 is the magnitude of the load applied to the plate.

And for a uniform load distribution, we have:

$$Q_{mn} = \sum_{m=1}^{\infty}\sum_{n=1}^{\infty} \frac{16q_0}{mn\pi^2} \tag{3-55}$$

4.1.1 Solving the bending motion equations:

By substituting the displacement equations **(3-52)** into the bending equations of motion, we obtain the system of equations for each given value of m and n. The algebraic system is expressed in the form:

$$[\boldsymbol{K}]\{\boldsymbol{d}\} = \{\boldsymbol{F}\} \tag{3-56}$$

Where:

$\boldsymbol{K}$ is the stiffness matrix and it is symmetric, $\boldsymbol{d}$ is the displacement vector represented by the parameters of amplitudes and $\boldsymbol{F}$ is the external load vector.

$$\begin{bmatrix} k_{11} & k_{12} & k_{13} & k_{14} & k_{15} \\ k_{21} & k_{22} & k_{23} & k_{24} & k_{25} \\ k_{31} & k_{32} & k_{33} & k_{34} & k_{35} \\ k_{41} & k_{42} & k_{43} & k_{44} & k_{45} \\ k_{51} & k_{52} & k_{53} & k_{54} & k_{55} \end{bmatrix} \begin{Bmatrix} J_{mn} \\ K_{mn} \\ L_{mn} \\ M_{mn} \\ N_{mn} \end{Bmatrix} = \begin{Bmatrix} 0 \\ 0 \\ Q_{mn} \\ 0 \\ 0 \end{Bmatrix} \tag{3-57}$$

Where:

$$k_{11} = A_{11}\alpha^2 + \mathrm{A}_{66}\,\beta^2 \; ; k_{12} = k_{21} = (A_{12} + \mathrm{A}_{66})\alpha\beta$$

$$k_{13} = k_{31} = \alpha^3(B^a_{11} - B_{11}) + \alpha\beta^2(B^a_{12} + 2\mathrm{B}^{\mathrm{a}}_{66} - 2\mathrm{B}_{66} - B_{12})$$

$$k_{14} = k_{41} = B^a_{11}\alpha^2 + \beta^2\mathrm{B}^{\mathrm{a}}_{66} \; ; k_{15} = k_{51} = (\mathrm{B}^{\mathrm{a}}_{66} + B^a_{12})\alpha\beta$$

$$k_{22} = A_{22}\beta^2 + A_{66}\alpha^2 \; ; k_{23} = k_{32} = \alpha^2\beta(B^a_{12} + 2B^a_{66} - 2B_{66} - B_{12}) + \beta^3(B^a_{22} - B_{22}) \tag{3-58}$$

$$k_{24} = k_{42} = (B^a_{12} + \mathrm{B}^{\mathrm{a}}_{66})\alpha\beta \; ; \; k_{25} = k_{52} = \mathrm{B}^{\mathrm{a}}_{66}\alpha^2 + B^a_{22}\,\beta^2$$

$$k_{33} = \alpha^4(D_{11} - 2D^a_{11} + D^{aa}_{11}) + \beta^4(D_{22} - 2D^a_{22} + D^{aa}_{22}) + \alpha^2\beta^2(2D_{12} - 4D^a_{12} + 2D^{aa}_{12} + 4\mathrm{D}_{66} + 4\mathrm{D}^{\mathrm{aa}}_{66} - 8\mathrm{D}^{\mathrm{a}}_{66}) + \mathrm{A}^a_{55}\alpha^2 + \mathrm{A}^a_{44}\beta^2$$

$$k_{34} = k_{43} = \alpha^3(D^{aa}_{11} - D^a_{11}) + \alpha\beta^2(D^{aa}_{12} + 2\mathrm{D}^{\mathrm{aa}}_{66} - D^a_{12} - 2\mathrm{D}^{\mathrm{a}}_{66}) + \mathrm{A}^a_{55}\alpha$$

$$k_{35} = k_{53} = \alpha^2\beta(D^{aa}_{12} + 2\mathrm{D}^{\mathrm{aa}}_{66} - D^a_{12} - 2\mathrm{D}^{\mathrm{a}}_{66}) + \beta^3(D^{aa}_{22} - D^a_{22}) + \mathrm{A}^a_{44}\beta$$

$$k_{44} = D^{aa}_{11}\alpha^2 + \mathrm{A}^a_{55} + \mathrm{D}^{\mathrm{aa}}_{66}\beta^2 \; ; k_{45} = k_{54} = (D^{aa}_{12} + \mathrm{D}^{\mathrm{aa}}_{66})\alpha\beta$$

$$k_{55} = D^{aa}_{22}\beta^2 + \mathrm{A}^a_{44} + \mathrm{D}^{\mathrm{aa}}_{66}\alpha^2$$

4.1.2 Solving the buckling motion equations:

By substituting the displacement equations into the buckling equations of motion, we obtain the system of equations for each given value of m and n in a stability problem (buckling analysis). The resulting system of algebraic equations can be expressed in the form:

$$[\boldsymbol{K'}]\{\boldsymbol{d}\} = \{\boldsymbol{0}\} \tag{3-59}$$

$\boldsymbol{K'}$ is the stiffness matrix for buckling problem and it is symmetric, $\boldsymbol{d}$ is the displacement vector represented by the parameters of amplitudes.

$$\begin{bmatrix} k_{11} & k_{12} & k_{13} & k_{14} & k_{15} \\ k_{21} & k_{22} & k_{23} & k_{24} & k_{25} \\ k_{31} & k_{32} & k_{33}+k & k_{34} & k_{35} \\ k_{41} & k_{42} & k_{43} & k_{44} & k_{45} \\ k_{51} & k_{52} & k_{53} & k_{54} & k_{55} \end{bmatrix} \begin{Bmatrix} J_{mn} \\ K_{mn} \\ L_{mn} \\ M_{mn} \\ N_{mn} \end{Bmatrix} = \begin{Bmatrix} 0 \\ 0 \\ 0 \\ 0 \\ 0 \end{Bmatrix} \tag{3-60}$$

Where:

$k_{11} = A_{11}\alpha^2 + \mathrm{A}_{66}\,\beta^2$; $k_{12} = k_{21} = (A_{12} + \mathrm{A}_{66})\alpha\beta$

$k_{13} = k_{31} = \alpha^3(B^a_{11} - B_{11}) + \alpha\beta^2(B^a_{12} + 2\mathrm{B}^{\mathrm{a}}_{66} - 2\mathrm{B}_{66} - B_{12})$

$k_{14} = k_{41} = B^a_{11}\alpha^2 + \beta^2\mathrm{B}^{\mathrm{a}}_{66}$; $k_{15} = k_{51} = (\mathrm{B}^{\mathrm{a}}_{66}+B^a_{12})\alpha\beta$

$k_{22} = A_{22}\beta^2 + A_{66}\alpha^2$; $k_{23} = k_{32} = \alpha^2\beta(B^a_{12} + 2B^a_{66} - 2B_{66} - B_{12}) + \beta^3(B^a_{22} - B_{22})$

$k_{24} = k_{42} = (B^a_{12} + B^a_{66})\alpha\beta$; $k_{25} = k_{52} = B^a_{66}\alpha^2 + B^a_{22}\,\beta^2$ (3-61)

$k_{33} + \mathrm{k} = \alpha^4(D_{11} - 2D^a_{11} + D^{aa}_{11}) + \beta^4(D_{22} - 2D^a_{22} + D^{aa}_{22}) + \alpha^2\beta^2(2D_{12} - 4D^a_{12} + 2D^{aa}_{12} + 4\mathrm{D}_{66} + 4\mathrm{D}^{\mathrm{aa}}_{66} - 8\mathrm{D}^{\mathrm{a}}_{66}) + \mathrm{A}^a_{55}\alpha^2 + \mathrm{A}^a_{44}\beta^2 + \mathrm{k}$

$k_{34} = k_{43} = \alpha^3(D^{aa}_{11} - D^a_{11}) + \alpha\beta^2(D^{aa}_{12} + 2\mathrm{D}^{\mathrm{aa}}_{66} - D^a_{12} - 2\mathrm{D}^{\mathrm{a}}_{66}) + \mathrm{A}^a_{55}\alpha$

$k_{35} = k_{53} = \alpha^2\beta(D^{aa}_{12} + 2\mathrm{D}^{\mathrm{aa}}_{66} - D^a_{12} - 2\mathrm{D}^{\mathrm{a}}_{66}) + \beta^3(D^{aa}_{22} - D^a_{22}) + \mathrm{A}^a_{44}\beta$

$k_{44} = D^{aa}_{11}\alpha^2 + \mathrm{A}^a_{55} + \mathrm{D}^{\mathrm{aa}}_{66}\beta^2$; $k_{45} = k_{54} = (D^{aa}_{12} + \mathrm{D}^{\mathrm{aa}}_{66})\alpha\beta$

$k_{55} = D^{aa}_{22}\beta^2 + \mathrm{A}^a_{44} + \mathrm{D}^{\mathrm{aa}}_{66}\alpha^2$

And:

$$k = \lambda P_{cr} \;\; ; \quad \lambda = \lambda_1\alpha^2 + \lambda_2\beta^2 \tag{3-62}$$

To find the critical buckling load P_{cr} (the smallest load that causes buckling), the system must be written in the following canonical form:

$$\left(\begin{bmatrix} k_{11} & k_{12} & k_{13} & k_{14} & k_{15} \\ k_{21} & k_{22} & k_{23} & k_{24} & k_{25} \\ \bar{k}_{31} & \bar{k}_{32} & \bar{k}_{33} & \bar{k}_{34} & \bar{k}_{35} \\ k_{41} & k_{42} & k_{43} & k_{44} & k_{45} \\ k_{51} & k_{52} & k_{53} & k_{54} & k_{55} \end{bmatrix} - P_{cr} \begin{bmatrix} 0 & 0 & 0 & 0 & 0 \\ 0 & 0 & 0 & 0 & 0 \\ 0 & 0 & -1 & 0 & 0 \\ 0 & 0 & 0 & 0 & 0 \\ 0 & 0 & 0 & 0 & 0 \end{bmatrix}\right) \begin{Bmatrix} J_{mn} \\ K_{mn} \\ L_{mn} \\ M_{mn} \\ N_{mn} \end{Bmatrix} = \begin{Bmatrix} 0 \\ 0 \\ 0 \\ 0 \\ 0 \end{Bmatrix} \quad (3\text{-}63)$$

Where:

$$\bar{k}_{3j} = \frac{k_{3j}}{\lambda} \quad ; \quad j = 1,2,3,4,5 \quad (3\text{-}64)$$

To find the nontrivial solution, the problem boils down to solving the equation of the determinant set equal to zero.

$$\left|\begin{bmatrix} k_{11} & k_{12} & k_{13} & k_{14} & k_{15} \\ k_{21} & k_{22} & k_{23} & k_{24} & k_{25} \\ \bar{k}_{31} & \bar{k}_{32} & \bar{k}_{33} & \bar{k}_{34} & \bar{k}_{35} \\ k_{41} & k_{42} & k_{43} & k_{44} & k_{45} \\ k_{51} & k_{52} & k_{53} & k_{54} & k_{55} \end{bmatrix} - P_{cr} \begin{bmatrix} 0 & 0 & 0 & 0 & 0 \\ 0 & 0 & 0 & 0 & 0 \\ 0 & 0 & -1 & 0 & 0 \\ 0 & 0 & 0 & 0 & 0 \\ 0 & 0 & 0 & 0 & 0 \end{bmatrix}\right| = 0 \quad (3\text{-}65)$$

4.1.3 Displacements and stresses fields:

After we obtained the solution for the five differential equations by Navier's method, the general displacement equations could be written by substituting (3-52) equations in (3-10).

For m=n=1, we get the following equations of displacement field:

$$\begin{cases} u(x,y,z) = cos\left(\frac{\pi}{a}x\right) sin\left(\frac{\pi}{b}y\right)\left[J_{11} - z\frac{\pi}{a}L_{11} + \left(\frac{h}{2}tanh(\frac{2z}{h}) - \frac{4}{3\,cosh^2(1)}(\frac{z^3}{h^2})\right)\left(M_{11} + \frac{\pi}{a}L_{11}\right)\right] \\ v(x,y,z) = sin\left(\frac{\pi}{a}x\right) cos\left(\frac{\pi}{b}y\right)\left[K_{11} - z\frac{\pi}{b}L_{11} + \left(\frac{h}{2}tanh(\frac{2z}{h}) - \frac{4}{3\,cosh^2(1)}(\frac{z^3}{h^2})\right)\left(N_{11} + \frac{\pi}{b}L_{11}\right)\right] \\ w(x,y,z) = L_{11}\, sin\left(\frac{\pi}{a}x\right) sin\left(\frac{\pi}{b}y\right) \end{cases} \quad (3\text{-}66)$$

Spontaneously, we obtain the deformation field by substituting (3-49) equations in (3-13) and we get:

$$\begin{cases} \varepsilon_{xx} = \sin\left(\frac{\pi}{a}x\right)\sin\left(\frac{\pi}{b}y\right)\left[-\frac{\pi}{a}J_{11} + z\left(\frac{\pi}{a}\right)^2 L_{11} - \left(\frac{h}{2}tanh(\frac{2z}{h}) - \frac{4}{3\cosh^2(1)}(\frac{z^3}{h^2})\right)\left(\frac{\pi}{a}M_{11} + \left(\frac{\pi}{a}\right)^2 L_{11}\right)\right] \\ \varepsilon_{yy} = \sin\left(\frac{\pi}{a}x\right)\sin\left(\frac{\pi}{b}y\right)\left[-\frac{\pi}{b}K_{11} + z\left(\frac{\pi}{b}\right)^2 L_{11} - \left(\frac{h}{2}tanh(\frac{2z}{h}) - \frac{4}{3\cosh^2(1)}(\frac{z^3}{h^2})\right)\left(\frac{\pi}{b}N_{11} + \left(\frac{\pi}{b}\right)^2 L_{11}\right)\right] \\ \varepsilon_{zz} = 0 \\ \gamma_{xy} = \cos\left(\frac{\pi}{a}x\right)\cos\left(\frac{\pi}{b}y\right)[\frac{\pi}{b}J_{11} + \frac{\pi}{a}K_{11} - 2z\frac{\pi^2}{ab}L_{11} + \left(\frac{h}{2}tanh(\frac{2z}{h}) - \frac{4}{3\cosh^2(1)}(\frac{z^3}{h^2})\right)(\frac{\pi}{b}M_{11} + \frac{\pi}{a}N_{11} \\ +2\frac{\pi^2}{ab}L_{11})] \\ \gamma_{xz} = \cos\left(\frac{\pi}{a}x\right)\sin\left(\frac{\pi}{b}y\right)\left[\frac{1}{\cosh^2\left(\frac{2z}{h}\right)} - \&\frac{1}{\cosh^2(1)}\left(\frac{2z}{h}\right)^2\right]\left(M_{11} + \frac{\pi}{a}L_{11}\right) \\ \gamma_{yz} = \sin\left(\frac{\pi}{a}x\right)\cos\left(\frac{\pi}{b}y\right)\left[\frac{1}{\cosh^2\left(\frac{2z}{h}\right)} - \&\frac{1}{\cosh^2(1)}\left(\frac{2z}{h}\right)^2\right]\left(N_{11} + \frac{\pi}{b}L_{11}\right) \end{cases} \quad (3\text{-}67)$$

To determine the stress field, we've to substitute (3-66) equations in (3-14) and then, we obtain the following stress field expressions:

$$\begin{aligned} \sigma_{xx} = {} & Q_{11}\sin\left(\frac{\pi}{a}x\right)\sin\left(\frac{\pi}{b}y\right)\left[-\frac{\pi}{a}J_{11} + z\left(\frac{\pi}{a}\right)^2 L_{11}\right. \\ & \left. - \left(\frac{h}{2}tanh(\frac{2z}{h}) - \frac{4}{3\cosh^2(1)}(\frac{z^3}{h^2})\right)\left(\frac{\pi}{a}M_{11} + \left(\frac{\pi}{a}\right)^2 L_{11}\right)\right] \\ & + Q_{12}\sin\left(\frac{\pi}{a}x\right)\sin\left(\frac{\pi}{b}y\right)\left[-\frac{\pi}{b}K_{11} + z\left(\frac{\pi}{b}\right)^2 L_{11}\right. \\ & \left. - \left(\frac{h}{2}tanh(\frac{2z}{h}) - \frac{4}{3\cosh^2(1)}(\frac{z^3}{h^2})\right)\left(\frac{\pi}{b}N_{11} + \left(\frac{\pi}{b}\right)^2 L_{11}\right)\right] \end{aligned} \quad (3\text{-}68)$$

$$\begin{aligned} \sigma_{yy} = {} & Q_{12}\sin\left(\frac{\pi}{a}x\right)\sin\left(\frac{\pi}{b}y\right)\left[-\frac{\pi}{a}J_{11} + z\left(\frac{\pi}{a}\right)^2 L_{11}\right. \\ & \left. - \left(\frac{h}{2}tanh(\frac{2z}{h}) - \frac{4}{3\cosh^2(1)}(\frac{z^3}{h^2})\right)\left(\frac{\pi}{a}M_{11} + \left(\frac{\pi}{a}\right)^2 L_{11}\right)\right] \\ & + Q_{22}\sin\left(\frac{\pi}{a}x\right)\sin\left(\frac{\pi}{b}y\right)\left[-\frac{\pi}{b}K_{11} + z\left(\frac{\pi}{b}\right)^2 L_{11}\right. \\ & \left. - \left(\frac{h}{2}tanh(\frac{2z}{h}) - \frac{4}{3\cosh^2(1)}(\frac{z^3}{h^2})\right)\left(\frac{\pi}{b}N_{11} + \left(\frac{\pi}{b}\right)^2 L_{11}\right)\right] \end{aligned} \quad (3\text{-}69)$$

$$\sigma_{xz} = Q_{55}\cos\left(\frac{\pi}{a}x\right)\sin\left(\frac{\pi}{b}y\right)\left[\frac{1}{\cosh^2\left(\frac{2z}{h}\right)} - \frac{1}{\cosh^2(1)}\left(\frac{2z}{h}\right)^2\right]\left(M_{11} + \frac{\pi}{a}L_{11}\right) \quad (3\text{-}70)$$

$$\sigma_{yz} = Q_{44}\sin\left(\frac{\pi}{a}x\right)\cos\left(\frac{\pi}{b}y\right)\left[\frac{1}{\cosh^2\left(\frac{2z}{h}\right)} - \frac{1}{\cosh^2(1)}\left(\frac{2z}{h}\right)^2\right]\left(N_{11} + \frac{\pi}{b}L_{11}\right) \quad (3\text{-}71)$$

$$\sigma_{xy} = Q_{66}\cos\left(\frac{\pi}{a}x\right)\cos\left(\frac{\pi}{b}y\right)\left[\frac{\pi}{b}J_{11} + \frac{\pi}{a}K_{11} - 2z\frac{\pi^2}{ab}L_{11} + \left(\frac{h}{2}tanh(\frac{2z}{h}) - \frac{4}{3\,cosh^2(1)}(\frac{z^3}{h^2})\right)\left(\frac{\pi}{b}M_{11} + \frac{\pi}{a}N_{11} + 2\frac{\pi^2}{ab}L_{11}\right)\right] \quad (3\text{-}72)$$

Where:

$$\begin{cases} Q_{11} = Q_{22} = \dfrac{E(z)}{1-\nu^2(z)} \\ Q_{12} = Q_{21} = \dfrac{\nu(z)E(z)}{1-\nu^2(z)} \\ Q_{44} = Q_{55} = Q_{66} = \dfrac{E(z)}{2\left(1+\nu(z)\right)} \end{cases} \quad (3\text{-}73)$$

Generally speaking, we can write displacements and stresses fields as follows:

- **Displacement field**

$$\begin{cases} u(x,y,z) = \sum_{m=1}^{\infty}\sum_{n=1}^{\infty} cos\left(\frac{m\pi}{a}x\right)sin\left(\frac{n\pi}{b}y\right)\left[J_{11} - z\frac{m\pi}{a}L_{11} + \left(\frac{h}{2}tanh(\frac{2z}{h}) - \frac{4}{3\,cosh^2(1)}(\frac{z^3}{h^2})\right)\left(M_{11} + \frac{m\pi}{a}L_{11}\right)\right] \\ v(x,y,z) = \sum_{m=1}^{\infty}\sum_{n=1}^{\infty} sin\left(\frac{m\pi}{a}x\right)cos\left(\frac{n\pi}{b}y\right)\left[K_{11} - z\frac{n\pi}{b}L_{11} + \left(\frac{h}{2}tanh(\frac{2z}{h}) - \frac{4}{3\,cosh^2(1)}(\frac{z^3}{h^2})\right)\left(N_{11} + \frac{n\pi}{b}L_{11}\right)\right] \\ w(x,y,z) = \sum_{m=1}^{\infty}\sum_{n=1}^{\infty} L_{11}\,sin\left(\frac{m\pi}{a}x\right)sin\left(\frac{n\pi}{b}y\right) \end{cases} \quad (3\text{-}74)$$

- **Stress field**

$$\sigma_{xx} = \sum_{m=1}^{\infty}\sum_{n=1}^{\infty} sin\left(\frac{m\pi}{a}x\right)sin\left(\frac{n\pi}{b}y\right)\left[Q_{11}\left(-\frac{m\pi}{a}J_{11} + z\left(\frac{m\pi}{a}\right)^2 L_{11} - \left(\frac{h}{2}tanh(\frac{2z}{h}) - \frac{4}{3\,cosh^2(1)}(\frac{z^3}{h^2})\right)\left(\frac{m\pi}{a}M_{11} + \left(\frac{m\pi}{a}\right)^2 L_{11}\right)\right) + Q_{12}\left(-\frac{n\pi}{b}K_{11} + z\left(\frac{n\pi}{b}\right)^2 L_{11} - \left(\frac{h}{2}tanh(\frac{2z}{h}) - \frac{4}{3\,cosh^2(1)}(\frac{z^3}{h^2})\right)\left(\frac{n\pi}{b}N_{11} + \left(\frac{n\pi}{b}\right)^2 L_{11}\right)\right)\right] \quad (3\text{-}75)$$

$$\sigma_{yy} = \sum_{m=1}^{\infty}\sum_{n=1}^{\infty} sin\left(\frac{m\pi}{a}x\right) sin\left(\frac{n\pi}{b}y\right)\left[Q_{12}\left(-\frac{m\pi}{a}J_{11} + z\left(\frac{m\pi}{a}\right)^2 L_{11} - \left(\frac{h}{2}tanh(\frac{2z}{h}) - \frac{4}{3\,cosh^2(1)}(\frac{z^3}{h^2})\right)\left(\frac{m\pi}{a}M_{11} + \left(\frac{m\pi}{a}\right)^2 L_{11}\right)\right) + Q_{22}\left(-\frac{n\pi}{b}K_{11} + z\left(\frac{n\pi}{b}\right)^2 L_{11} - \left(\frac{h}{2}tanh(\frac{2z}{h}) - \frac{4}{3\,cosh^2(1)}(\frac{z^3}{h^2})\right)\left(\frac{n\pi}{b}N_{11} + \left(\frac{n\pi}{b}\right)^2 L_{11}\right)\right)\right] \quad (3\text{-}76)$$

$$\sigma_{xz} = Q_{55}\sum_{m=1}^{\infty}\sum_{n=1}^{\infty} cos\left(\frac{m\pi}{a}x\right) sin\left(\frac{n\pi}{b}y\right)\left[\frac{1}{cosh^2\left(\frac{2z}{h}\right)} - \frac{1}{cosh^2(1)}\left(\frac{2z}{h}\right)^2\right]\left(M_{11} + \frac{m\pi}{a}L_{11}\right) \quad (3\text{-}77)$$

$$\sigma_{yz} = Q_{44}\sum_{m=1}^{\infty}\sum_{n=1}^{\infty} sin\left(\frac{m\pi}{a}x\right) cos\left(\frac{n\pi}{b}y\right)\left[\frac{1}{cosh^2\left(\frac{2z}{h}\right)} - \frac{1}{cosh^2(1)}\left(\frac{2z}{h}\right)^2\right]\left(N_{11} + \frac{n\pi}{b}L_{11}\right) \quad (3\text{-}78)$$

$$\sigma_{xy} = Q_{66}\sum_{m=1}^{\infty}\sum_{n=1}^{\infty} cos\left(\frac{m\pi}{a}x\right) cos\left(\frac{n\pi}{b}y\right)\left[\frac{n\pi}{b}J_{11} + \frac{m\pi}{a}K_{11} - 2z\frac{mn\pi^2}{ab}L_{11} + \left(\frac{h}{2}tanh(\frac{2z}{h}) - \frac{4}{3\,cosh^2(1)}(\frac{z^3}{h^2})\right)\left(\frac{n\pi}{b}M_{11} + \frac{m\pi}{a}N_{11} + 2\frac{mn\pi^2}{ab}L_{11}\right)\right] \quad (3\text{-}79)$$

5. Conclusion:

In this chapter, our focus was on deriving the governing equations of motion for a plate made of functionally graded graphene platelets reinforced composite (FG-GPLRC).

To start with, we determined the displacement field using the hyperbolic higher-order shear deformation theory (HSDT) proposed by Mahi et al. Based on the displacement field, we then derived the deformation field and the stress field of the FG-GPLRC plate. This was done by considering the material properties of the composite, which vary continuously in the thickness direction.

To obtain the motion equations, we use the energetic formulation of Hamilton on our FG-GPLRC plate, we were able to derive the governing equations of motion.

Finally, we used the classical Navier method to solve analytically our bending and buckling problems for simply supported plates.

CHAPTER 4

RESULTS AND DISCUSSIONS

1. Introduction:

In this chapter, we will present the results and discussions of the bending and buckling problems. These results were used with the calculation code developed in Python. Python is an interpreted language, unlike other classical languages which are compiled languages. Python can therefore be seen as an interactive tool that is always ready to react to your commands. We will compare the results with the published papers. The results representing the stresses and displacements as well as the critical buckling load will be represented in the form of appropriate graphs to show the influence of the parameters considered (geometric dimensions, relative thickness and volume fraction of the graphene nano-platelets distributions through the FG composite plate) in this study.

2. Numerical resolution of the static problem:

For our study, we are making a comparison of the results of reference [40] to validate both buckling and bending problems.

In this section, several numerical examples are presented to study the bending and buckling of FG-GPLRC plates. The properties of the epoxy matrix are given by:

$$\nu m = 0.34$$
$$\rho m = 1200 \text{ Kg/m}^3$$
$$Em = 3 \text{ GPa}$$

The mechanical properties of graphene nanoplatelets (GPL) are given by:

$$\nu_{GPL} = 0.186$$
$$\rho_{GPL} = 1060 \text{ Kg/m}^3$$
$$E_{GPL} = 1.01 \text{ TPa}$$
$$l_{GPL} = 2.5 \text{ µm}$$
$$w_{GPL} = 1.5 \text{ µm}$$
$$t_{GPL} = 1.5 \text{ nm}$$

2.1 Graphical representation of the FG-GPLRC plate properties:

After a series of calculations, we obtain the graphs of $V_{GPl}(z)$, $E_m^{GPl}(z)$, $\rho_m^{GPl}(z)$, $\nu_m^{GPl}(z)$ and $G_m^{GPl}(z)$ for the three patterns of distributions (b/h=10, Agpl=0.01).

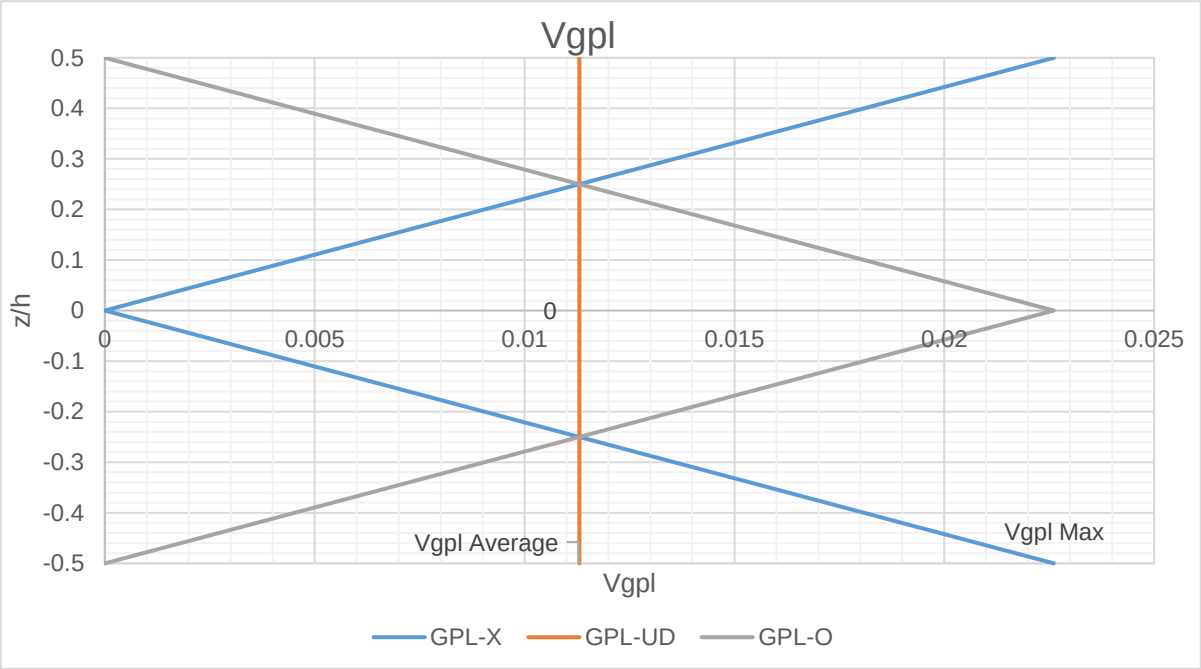

Figure 31: Volume fraction variation through the plate thickness for different distributions.

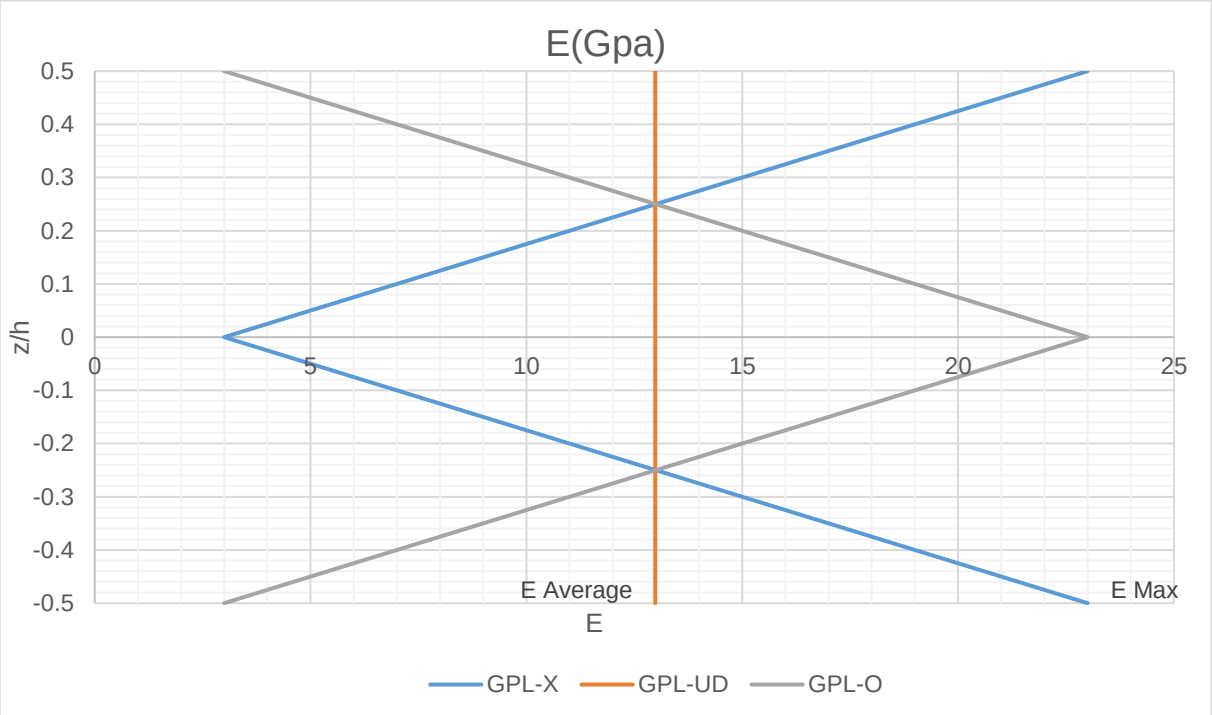

Figure 32: Young's modulus variation through the plate thickness for different distributions.

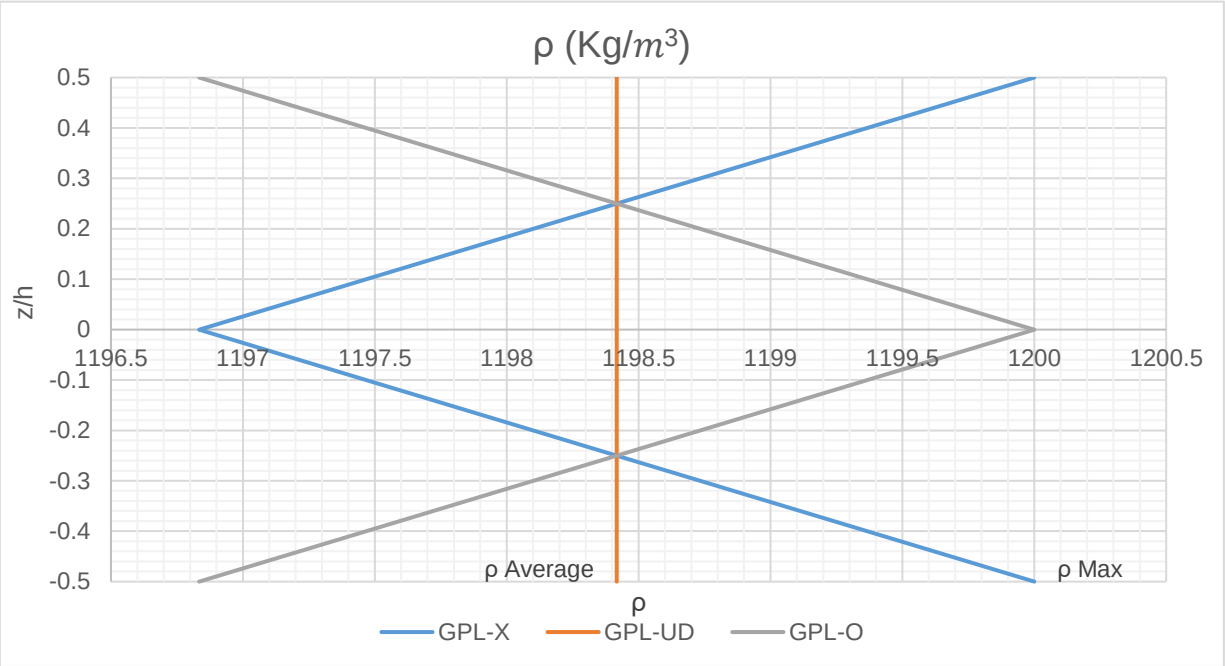

Figure 33: Volumetric density variation through the plate thickness for different distributions.

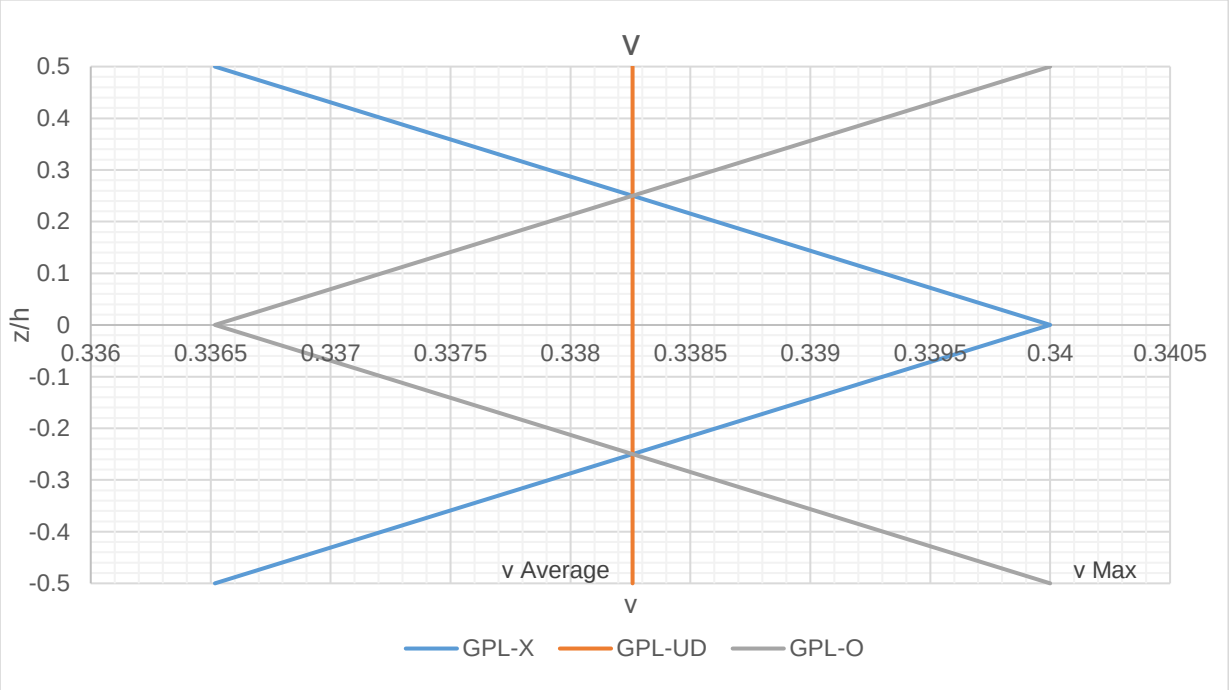

Figure 34: Poisson coefficient variation through the plate thickness for different distributions.

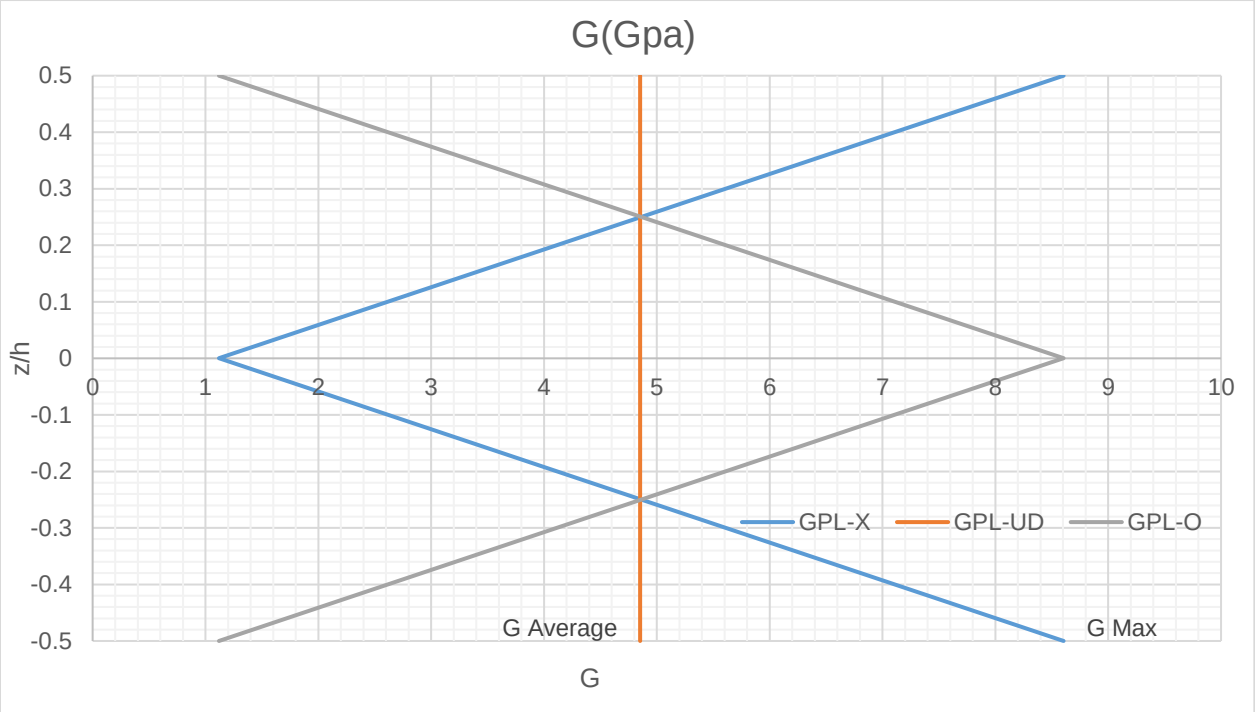

Figure 35: Shear modulus variation through the plate thickness for different distributions.

Basing on the analysis of the different graphs of mechanical properties, we note that:

- Constant values for the different mechanical properties in the **UD pattern** through the plate thickness **(Figures 30-34)**.
- A symmetric variation for the different mechanical properties in **X pattern (surface rich)** and **O pattern (middle rich)** through the plate thickness **(Figures 30-34)**.

2.2 Stiffnesses calculation of the static system:

Table 5: Extension stiffnesses of the plate for different distribution patterns and for different volume fractions

Volume fraction Agpl	Extension Stiffnesses (Pa.m×10^8)	GPL-UD	GPL-X	GPL-O
0.01	A_{11}	6.598839003020	6.598963440422	6.598963440422
	A_{12}	2.232116044442	2.229214091310	2.229214091310

	A_{66}	2.183361479286	2.184874674 555	2.184874674555
0.02	A_{11}	11.65859946743	11.659203956971	11.659203956971
	A_{12}	3.923379799696	3.9118360231390	3.9118360231390
	A_{66}	3.867609833869	3.8736839669160	3.8736839669160
0.03	A_{11}	16.70594796372	16.707545607894	16.707545607894
	A_{12}	5.592991885265	5.567159521285	5.567159521285
	A_{66}	5.556478039218	5.570193043304	5.570193043304

Table 6: Transverse-shear stiffnesses of the plate for different distribution patterns and for different volume fractions

Volume Fraction Agpl	**Higher order Shear Stiffnesses (Pa.m×10^8)**	**GPL-UD**	**GPL-X**	**GPL-O**
0.01	A_{44}^a	1.0530574319674	0.7129652103731	1.394642083389
	A_{55}^a	1.0530574319674	0.7129652103731	1.394642083389
0.02	A_{44}^a	1.8653875311702	1.1839259187836	2.552839922108
	A_{55}^a	1.8653875311702	1.1839259187836	2.552839922108
0.03	A_{44}^a	2.6799458313585	1.6558385787600	3.717579879938
	A_{55}^a	2.6799458313585	1.6558385787600	3.717579879938

Table 7 : Coupling stiffnesses of the plate for different distribution patterns and for different volume fractions.

Volume Fraction Agpl	**Coupling Stiffnesses (Pa.m²)**	**GPL-UD**	**GPL-X**	**GPL-O**
0.01	B_{11}	0	0	0
	B_{12}	0	0	0
	B_{66}	0	0	0
0.02	B_{11}	0	0	0
	B_{12}	0	0	0
	B_{66}	0	0	0
0.03	B_{11}	0	0	0
	B_{12}	0	0	0
	B_{66}	0	0	0

Table 8: Higher order coupling stiffnesses of the plate for different distribution patterns and for different volume fractions.

Volume Fraction Agpl	Higher order Coupling Stiffnesses (Pa.m²)	GPL-UD	GPL-X	GPL-O
0.01	B_{11}^{a}	0	0	0
	B_{12}^{a}	0	0	0
	B_{66}^{a}	0	0	0
0.02	B_{11}^{a}	0	0	0
	B_{12}^{a}	0	0	0
	B_{66}^{a}	0	0	0
0.03	B_{11}^{a}	0	0	0
	B_{12}^{a}	0	0	0
	B_{66}^{a}	0	0	0

Table 9: Bending stiffnesses of the plate for different distribution patterns and for different volume fractions.

Volume Fraction Agpl	Bending Stiffnesses (Pa.m³×10⁵)	GPL-UD	GPL-X	GPL-O
0.01	D_{11}	1.113554081	1.541591954	0.685566605
	D_{12}	0.376669582	0.519891599	0.232272274
	D_{66}	0.368442249	0.377512657	0.226647165
0.02	D_{11}	1.967388660	2.822556158	1.112465978
	D_{12}	0.662070341	0.944053323	0.375412124
	D_{66}	0.652659159	0.939251417	0.368526927
0.03	D_{11}	2.819128718	4.10060154	1.538302931
	D_{12}	0.943817380	1.360158415	0.517042139
	D_{66}	0.937655669	1.370221564	0.510644358

Table 10: Higher order bending stiffnesses of the plate for different distribution patterns and for different volume fractions.

Volume Fraction Agpl	Higher order Bending Stiffnesses (Pa.m³×10⁵)	GPL-UD	GPL-X	GPL-O

0.01	$\boldsymbol{D_{11}^{a}}$	0.845863855	1.139339060	0.552423578
	D_{12}^{a}	0.286120980	0.384313745	0.187113702
	D_{66}^{a}	0.2798714378	0.377512657	0.182654938
0.02	D_{11}^{a}	1.4944428702	2.080770938	0.908284467
	D_{12}^{a}	0.5029134919	0.696231747	0.306355155
	D_{66}^{a}	0.4957646891	0.692269595	0.300964655
0.03	D_{11}^{a}	2.1414308721	3.020047111	1.263263052
	D_{12}^{a}	0.7169306115	1.002347044	0.424263605
	D_{66}^{a}	0.7122501302	1.008850033	0.419499723

Table 11 : Higher order bending stiffnesses of the plate for different distribution patterns and for different volume fractions.

Volume Fraction Agpl	Higher order Bending Stiffnesses	GPL-UD ($Pa.m^3 \times 10^5$)	GPL-X ($Pa.m^3 \times 10^5$)	GPL-O ($Pa.m^3 \times 10^5$)
0.01	D_{11}^{aa}	0.652826130	0.853827579	0.451849129
	D_{12}^{aa}	0.220824250	0.288070325	0.153008002
	D_{66}^{aa}	0.216000939	0.282878627	0.149420563
0.02	D_{11}^{aa}	1.153390523	1.554967838	0.751931978
	D_{12}^{aa}	0.388141739	0.520520904	0.253494462
	D_{66}^{aa}	0.382624391	0.517223466	0.249218758
0.03	D_{11}^{aa}	1.652726995	2.254494312	1.051273582
	D_{12}^{aa}	0.553317219	0.748744032	0.352814881
	D_{66}^{aa}	0.549704888	0.752875139	0.349229350

After analyzing the results of the various stiffnesses represented in the tables bellow, we noted that:

- All stiffnesses increase by increasing the mass fraction of GPLs.
- The results of extension stiffnesses A_{ij} are quietly the same with some light differences at **UD pattern** (**Table 5**).
- The uniform distribution pattern always takes the average values comparing it with the surface rich and the middle rich distributions.
- A significant behavior from **O pattern** where the transverse shear stiffnesses give the greatest values comparing to **X** and **UD patterns**, the values of $\boldsymbol{A_{ij}^{a}}$ decrease in **UD pattern** and decrease more in **X pattern** (**Table 6**).

- The coupling stiffnesses (extension-bending stiffnesses) give a null value this because of the symmetry of the different distribution patterns over the plan z/h=0 (**Table 7-8**).
- A significant behavior from X **pattern** where the bending and the higher order bending stiffnesses give the greatest values comparing to **UD** and **O patterns**, the values of D_{ij}, D_{ij}^{a}, and D_{ij}^{aa} decrease in **UD pattern** and decrease more in **O pattern** (**Table 9-10-11**).

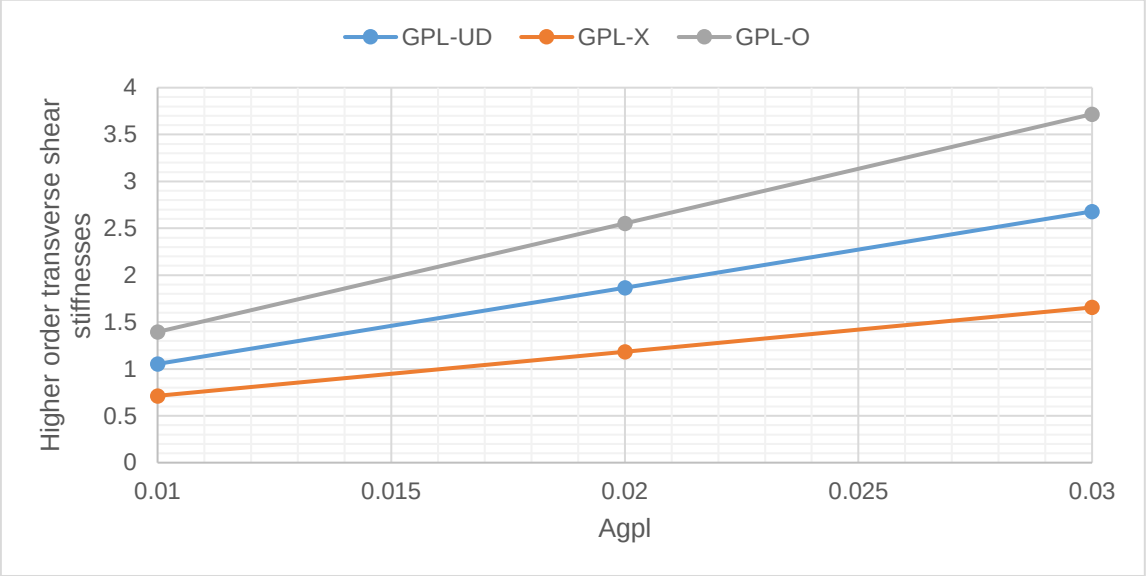

Figure 36: Agpl mass fraction effect on the higher order transverse shear stiffnesses $\boldsymbol{A_{ij}^{a}}$.

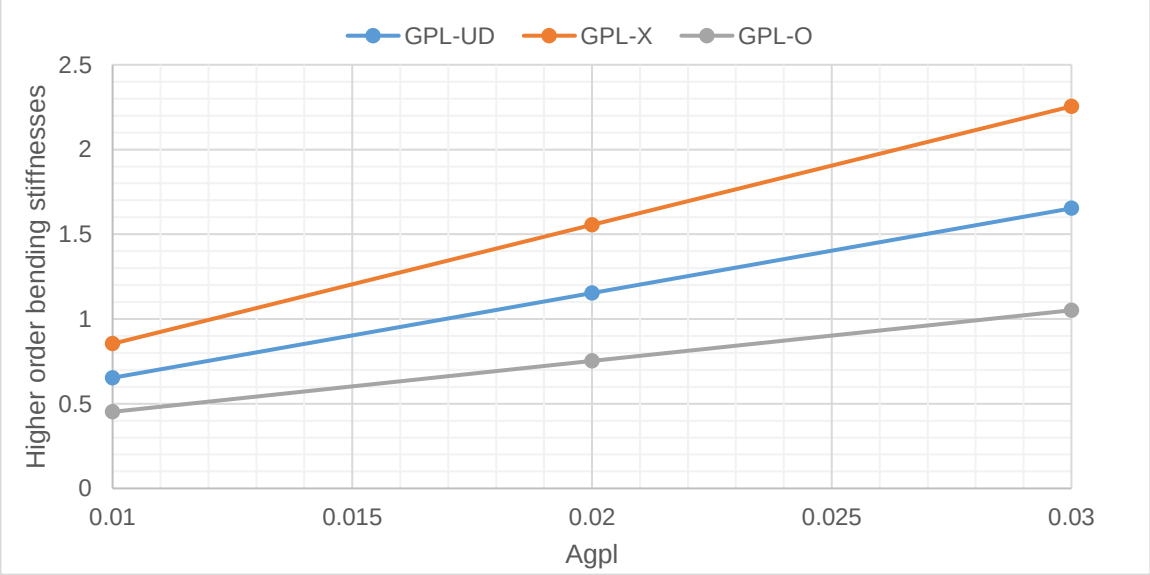

Figure 37: Agpl mass fraction effect on the higher order bending stiffnesses $\boldsymbol{D_{ij}^{aa}}$.

2.3 Buckling analysis:

The response to buckling of composite plates reinforced by graphene nano-platelets (GPLRC) is studied. The distribution of GPLs through the thickness of the plate can be uniform or graduated by a median symmetrical pattern. The properties of the plate FG-GPLRC are obtained using the modified rule of mixtures, Halpin-Tsai model is employed to calculate Young's modulus. The higher-order plate theory (HSDT) is adopted to develop or derive the basic equations of plate motion.

The Navier method has been utilized to derive elastic stiffness matrices, specifically for edges in simple supports (SSSS). Convergence and comparison studies have been conducted to demonstrate the efficiency and accuracy of the method. Parametric studies have also been carried out to investigate the impact of GPL mass fraction, thickness distribution law, and the a/h ratio of the plate. The results indicate that a gradual functional distribution and strategic use of nano-platelets can enhance the plate's buckling ability, leading to lower critical buckling loads. Furthermore, enriching the matrix with graphene nano-platelets has been shown to improve the buckling loads of FG-GPLRC plates.

2.3.1 Comparing results:

In this part, several numerical examples are presented and discussed to verify the accuracy and efficiency of the present theory in the prediction of the critical buckling load of an FG-GPLRC plate subjected to a uniaxial compression load.

The dimensionless critical buckling loads are calculated using the Python program that we created, which utilizes the dimensionless form as follows:

$$\bar{P}_{cr} = \frac{100 P_{cr}(1 - \nu_m{}^2)}{E_m h} \tag{4-1}$$

Table 12: Validation of dimensionless critical buckling load of FG-GPLRC square plate subjected to a uniaxial compression.

Agpl (%)	Reference	SSSS		
		Pattern		
		GPL- UD	GPL- X	GPL- O
0.0	Present (HSDT)	3.1048	3.1048	3.1048
	Ghandourah et al [40]	3.1046	3.1046	3.1046
	|Error (%)|	0.006	0.006	0.006
0.1	Present (HSDT)	3.1552	3.1781	3.1324
	Ghandourah et al [40]	3.1550	3.1732	3.1367
	|Error (%)|	0.006	0.15	0.13
0.3	Present (HSDT)	3.2565	3.3256	3.1876
	Ghandourah et al [40]	3.2562	3.3115	3.2011
	|Error (%)|	0.009	0.42	0.42
0.5	Present (HSDT)	3.3586	3.4747	3.2429
	Ghandourah et al [40]	3.3583	3.4510	3.2657
	|Error (%)|	0.008	0.68	0.69

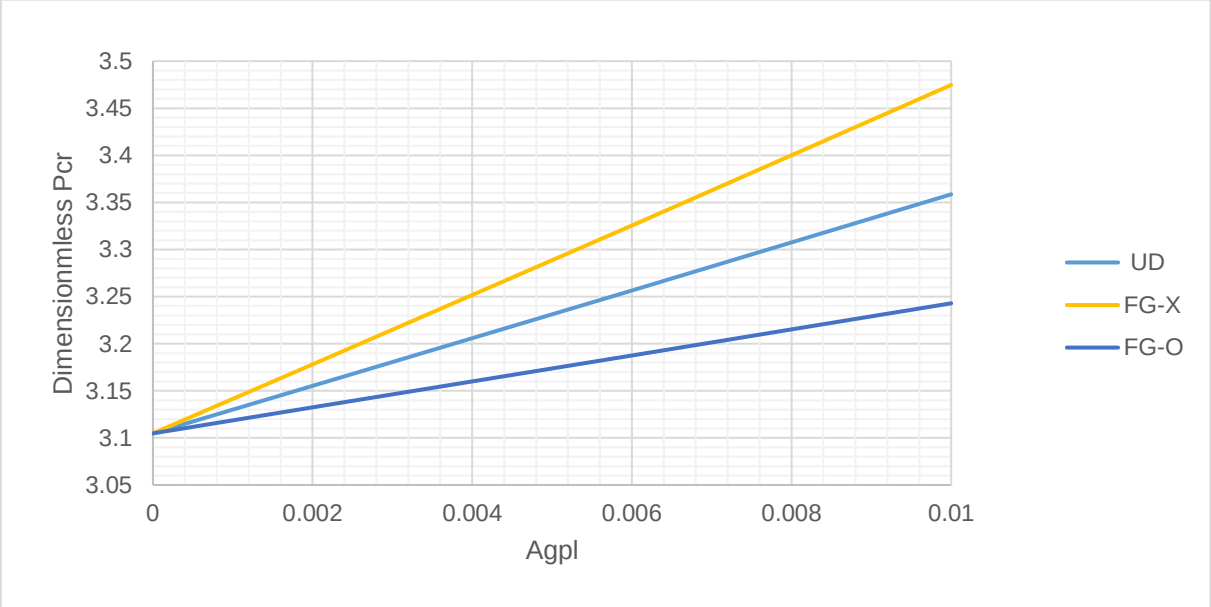

Figure 38: Variation of the dimensionless critical buckling load FG-GPLRC plate subjected to a uniaxial compression.

The comparison table displays the dimensionless critical buckling load of an FG-GPLRC square plate under uni-axial compression. To provide a clearer understanding of the evolution of these loads, a graph illustrating the variation of mass fraction (Agpl) for different distribution patterns has been developed. The relative error of the results, when compared to previously published data, remains low, although there is a slight increase for the GPL-O distribution. This increase is due to the employment of a different plate theory, which impacts the GPL-O pattern more significantly than the other patterns. Overall, this demonstrates the effective performance of the developed Python program, establishing its reliability for conducting a parametric study, as detailed in the next section. **Figure 37** shows that as the mass fraction increases, the dimensionless critical buckling load also increases because the plate becomes more rigid. In summary, the higher the (Agpl) (making the plate richer), the higher the supported critical buckling load.

2.3.2 Parametric study:

In this section, we study the influence of the a/h ratio and mass fraction Agpl on the critical dimensionless buckling load for an FG-GPLRC square plate. The figures below show the variation of the dimensionless critical buckling load according to the a/h ratio and GPLs mass fraction, the dimensionless critical load decreases while the ratio increases, this gives an information that the plate become thinner so the critical load supported becomes smaller, in the other hand each time the mass fraction increases, the critical load increases, it means that more we reinforced the plate, bigger critical load required. The shape of the graph is given because of the formulation of the dimensionless critical buckling load expression. After the figures have been analyzed, we can deduce that the X pattern gives more rigidity to the plate to support the minimum load causes buckling, after it comes UD pattern and last O pattern. All the distribution patterns (UD, FG-X, FG-O) give the same type of variation of the dimensionless critical buckling load. For a biaxial compression the dimensionless critical buckling load becomes smaller to the half value of the case where the plate is under a uniaxial compression, this is available for all types and values of the reinforcements which we can deduce that the plate bearing to buckling decreasing even it has been reinforced.

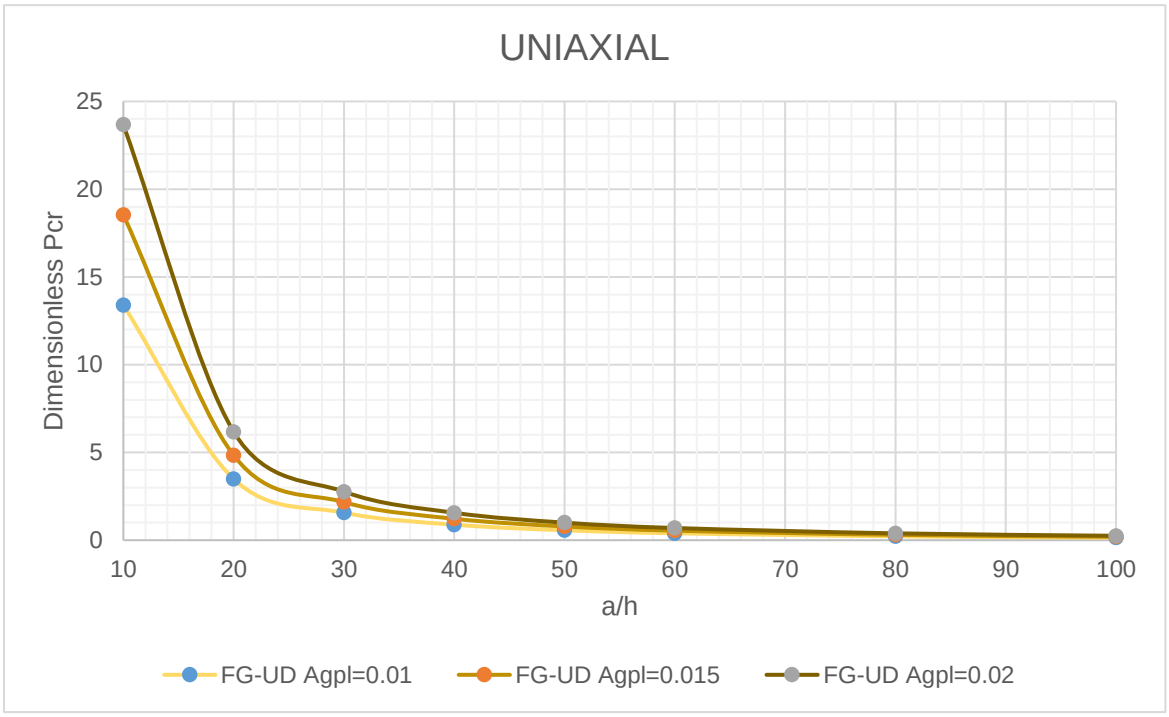

Figure 39: Effect of a/h ratio on the dimensionless critical buckling load for a plate FG-UD ($\lambda 1 = -1, \lambda 2 = 0$)

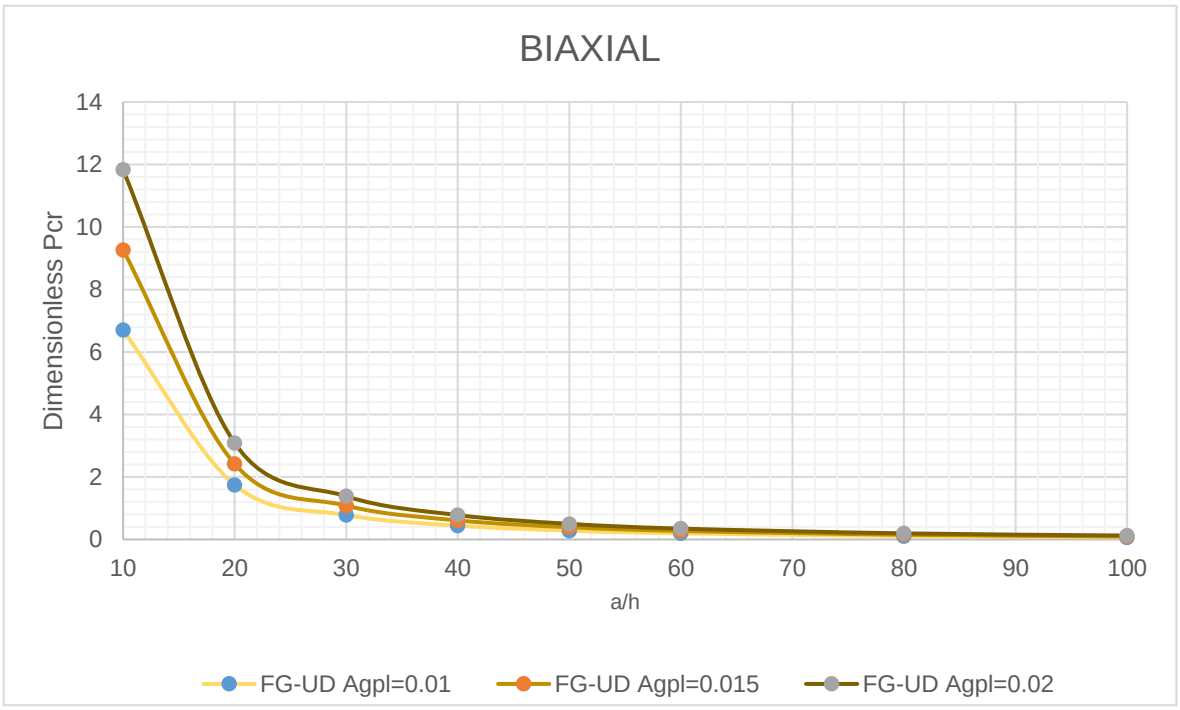

Figure 40: Effect of a/h ratio on the dimensionless critical buckling load for a plate FG-UD ($\lambda 1 = -1, \lambda 2 = -1$)

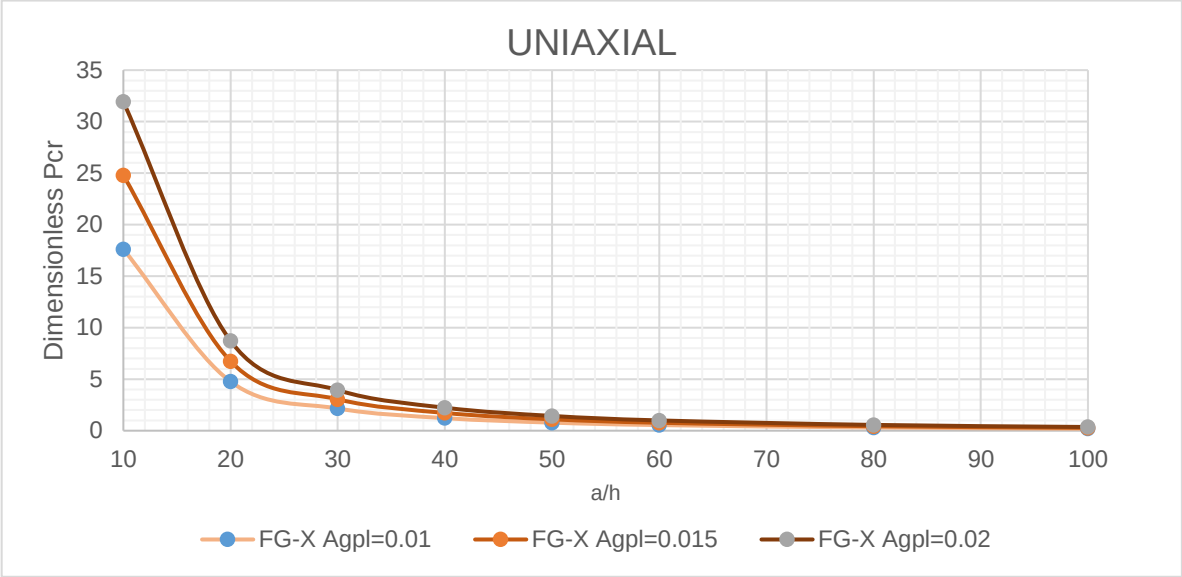

Figure 41: Effect of a/h ratio on the dimensionless critical buckling load for a plate FG-X ($\lambda 1 = -1, \lambda 2 = 0$)

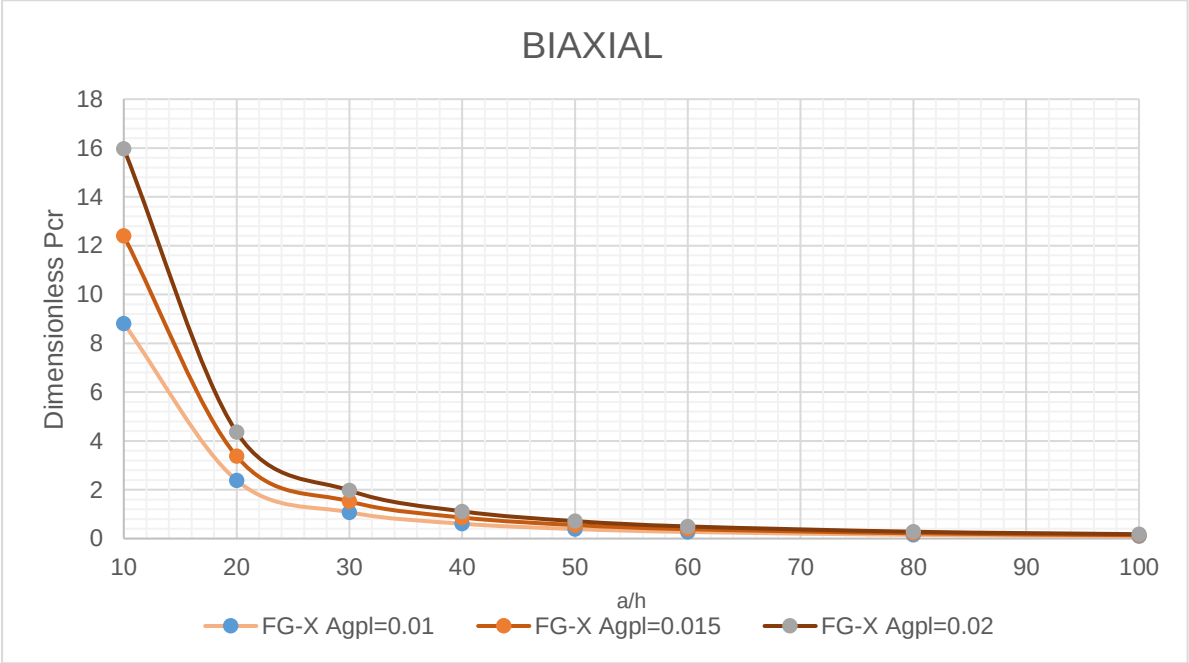

Figure 42: Effect of a/h ratio on the dimensionless critical buckling load for a plate FG-X ($\lambda 1 = -1, \lambda 2 = -1$)

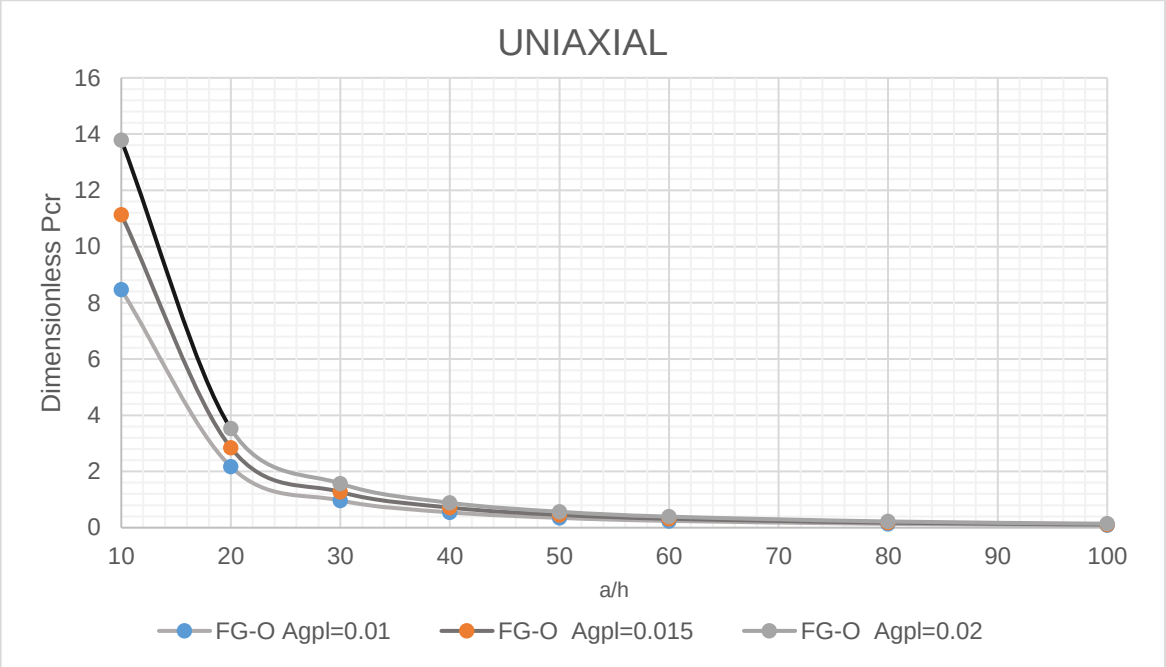

Figure 43: Effect of a/h ratio on the dimensionless critical buckling load for a plate FG-O ($\lambda 1 = -1, \lambda 2 = 0$)

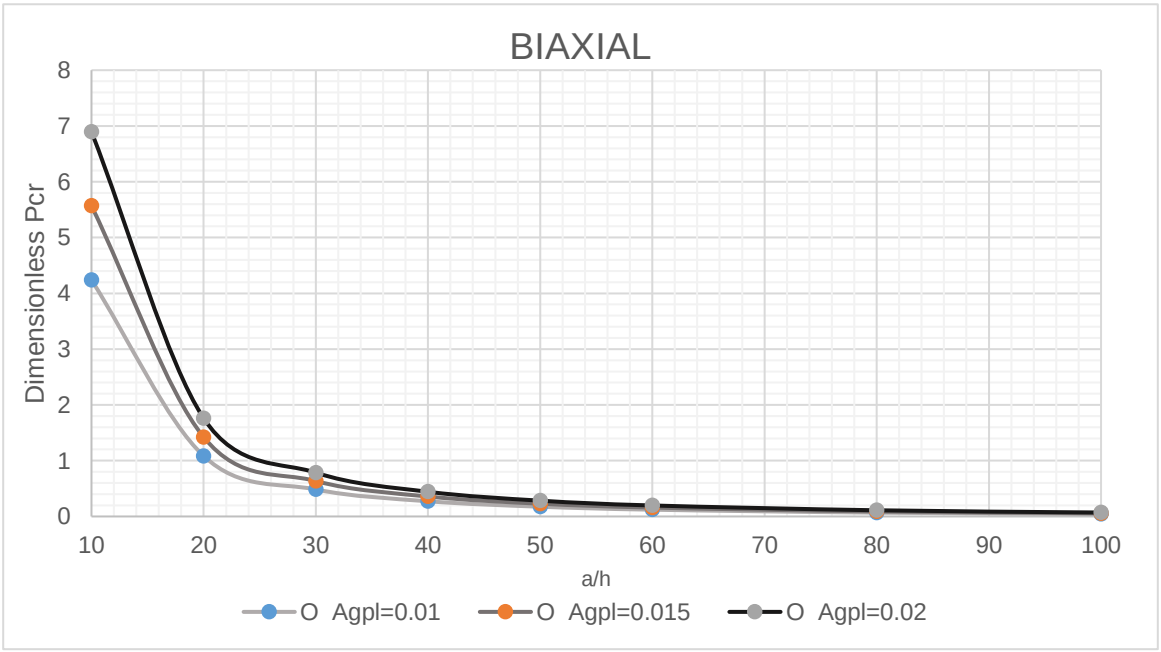

Figure 44: Effect of a/h ratio on the dimensionless critical buckling load for a plate FG-O ($\lambda 1 = -1, \lambda 2 = -1$)

Table 13: Effect of the variation of a/h ratio on the dimensionless critical buckling load ($\bar{P}$cr) for two type of compression Agpl=0.01.

Pattern	AGPL 0.01		
	a/h	UNIAXIAL	BIAXIAL
UD	2	144.72	72.36
	5	45.90	22.95
	10	13.4	6.7001
	20	3.49	1.7485
	30	1.567	0.7835
	40	0.884	0.442
	50	0.5665	0.2832
	100	0.1418	0.0709
X	2	130.45	65.22
	5	53.93	26.96
	10	17.62	8.8127
	20	4.77	2.3876
	30	2.1558	1.0779
	40	1.2193	0.6096
	50	0.7824	0.3912
	100	0.1962	0.0981
O	2	123.55	61.77
	5	31.10	15.55
	10	8.47	4.2396
	20	2.1689	1.0844
	30	0.9681	0.484
	40	0.5453	0.2726
	50	0.3492	0.1746
	100	0.0874	0.0437

Table 14 : Effect of the variation of a/h ratio on the dimensionless critical buckling load ($\bar{P}$cr) for two type of compression, Agpl=0.015.

Pattern	Agpl 0.015		
	a/h	UNIAXIAL	BIAXIAL
UD	2	200.37	100.18
	5	63.52	31.76
	10	18.5397	9.2698
	20	4.8381	2.419
	30	2.1679	1.0839
	40	1.2229	0.6114
	50	0.7837	0.3918
	100	0.1962	0.0981
X	2	177	88.5
	5	74.92	37.46
	10	24.7945	12.3972
	20	6.7482	3.3741
	30	3.0493	1.5246
	40	1.7253	0.8626
	50	1.1072	0.5536
	100	0.2778	0.1389
O	2	166.10	83.05
	5	41.05	20.52
	10	11.1382	5.5691
	20	2.8453	1.4226
	30	1.2697	0.6348
	40	0.7152	0.3576
	50	0.458	0.229
	100	0.1146	0.0573

Table 15: Effect of the variation of a/h ratio on the dimensionless critical buckling load ($\bar{P}$cr) for two type of compression, Agpl=0.02.

Pattern	Agpl 0.02		
	a/h	UNIAXIAL	BIAXIAL
UD	2	256.03	128.01
	5	81.12	40.56
	10	23.6737	11.8368
	20	6.1775	3.0887
	30	2.768	1.384
	40	1.5615	0.7807
	50	1.0006	0.5003
	100	0.2506	0.1253
X	2	223.40	111.70
	5	95.82	47.91
	10	31.9467	15.9733
	20	8.7183	4.3591
	30	3.9417	1.9708
	40	2.2307	1.1153
	50	1.4317	0.7158
	100	0.3592	0.1796
O	2	208.43	104.21
	5	50.96	25.48
	10	13.7924	6.8962
	20	3.5208	1.7604
	30	1.5709	0.7854
	40	0.8848	0.4424
	50	0.5666	0.2833
	100	0.1417	0.0708

2.4 Bending analysis:

2.4.1 Comparing results:

In this study, we have assumed that the plate is simply supported. To ensure the accuracy of our results, we have compiled the data in Table 16 for comparison purposes. In our calculation code, we have utilized the following dimensionless expressions.

$$\bar{w}(z) = \frac{10E_0 h}{a^2 q_0} w\left(\frac{a}{2}, \frac{b}{2}, \frac{h}{2}\right)$$

$$\bar{\sigma}_{xx}(z) = \frac{10h^2}{a^2 q_0} w\left(\frac{a}{2}, \frac{b}{2}, \frac{h}{2}\right)$$

$$\bar{\sigma}_{xy}(z) = \frac{10h^2}{a^2 q_0} \sigma_{xy}\left(0, 0, -\frac{h}{2}\right) \qquad (\mathbf{4\text{-}2})$$

$$\bar{\sigma}_{xz}(z) = \frac{10h^2}{a^2 q_0} \sigma_{xz}\left(0, \frac{b}{2}, 0\right)$$

Where E_0=1GPa

In this section, the response to the bending of an FGM plate is obtained under the action of a sinusoidal distribution of the transverse load. Table 16 contains the bending results obtained thanks to the higher-order shear deformation theory for a square FGM plate.

Table 16 shows the dimensionless central deflection $\bar{w}$ and the dimensionless stresses of three types of plates squares simply supported and subjected to a sinusoidal transverse load q_0. The data are the same as those of the references used for the comparison.

The results of the present formulation are compared with those of the quasi-3D theory reported by Ghandourah et al [40] where the transverse strain is null. Three types of distributions of graphene nanoplatelets through the thickness are considered, referred to in the literature by UD, FG-O and FG-X. Based on the good results obtained with a low relative error, it is evident that the method being used has a significant impact on the GPL-O distribution. The slight increase in the transverse shear stress can be attributed to the implications of the plate theory being utilized. It can be concluded that the analysis, based on a higher-order shear deformation theory and an analytical method of solving, is well-suited for deformation problems in moderately thick FGM plates reinforced by GPLs and simply supported. We observe that the central deflection of the FG-O GPLRC plate is larger than the deflection of the

UD-GPLRC and FG-X GPLRC plate because the latter make the plate stiffer, which leads us to higher values of the dimensionless axial stress $\bar{\sigma}_{xx}$ and the dimensionless shear stress $\bar{\sigma}_{xy}$ for the UD-GPLRC and FG-X GPLRC plate where the table results make a good agreement with it. But for the dimensionless transverse shear stress $\bar{\sigma}_{xz}$, the FG-O GPLRC plate shows stiffer pattern than FG-X GPLRC and UD-GPLRC plate.

Table 16: Validation of dimensionless central deflection and stresses of FG-GPLRC square plate with a/h=10 and Agpl=1%.

Pattern	Reference	$\bar{w}$	$\bar{\sigma}_{xx}$	$\bar{\sigma}_{xy}$	$\bar{\sigma}_{xz}$
GPL-UD	Present (HSDT)	8.8950	2.0558	1.0165	0.2504
	Ghandourah et al [40]	8.8943	2.0554	1.0163	0.2463
	$\lvert Error\ (\%)\rvert$	0.007	0.019	0.019	1.66
GPL- X	Present (HSDT)	8.5983	2.1303	1.0575	0.2378
	Ghandourah et al [40]	8.6554	2.0951	1.0387	0.2390
	$\lvert Error\ (\%)\rvert$	0.65	1.68	1.80	0.5
GPL- O	Present (HSDT)	9.2115	1.9772	0.9738	0.2626
	Ghandourah et al [40]	9.1463	2.0136	0.9931	0.2535
	$\lvert Error\ (\%)\rvert$	0.71	1.80	1.94	3.58

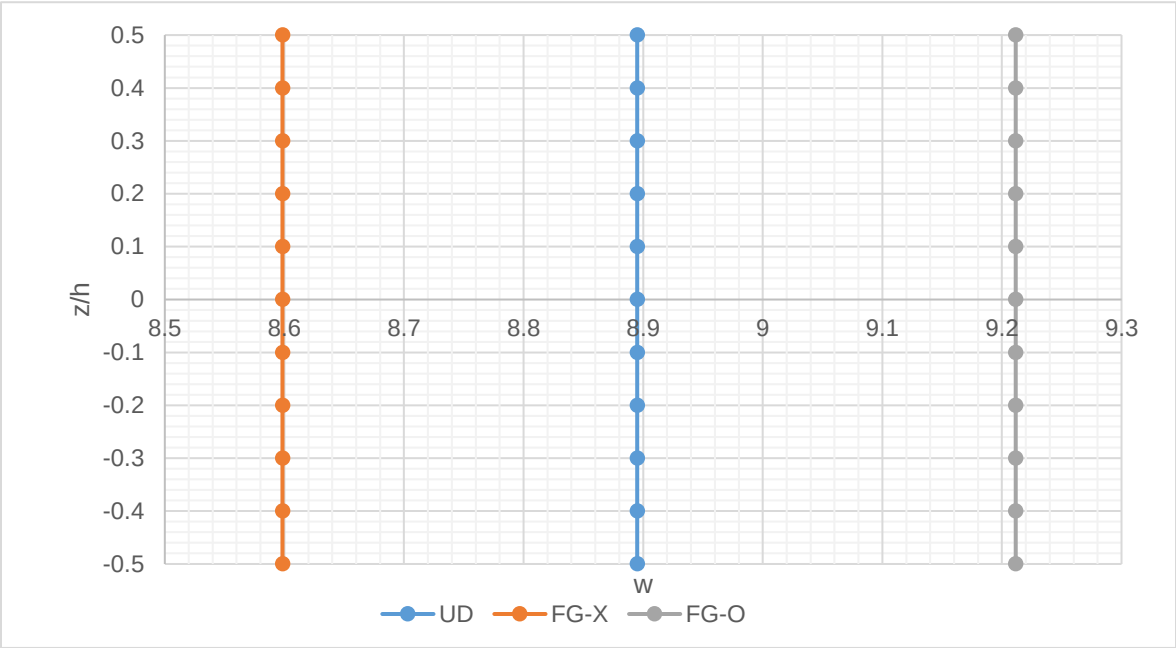

Figure 45: Variation of Dimensionless deflection through the plate thickness for different patterns.

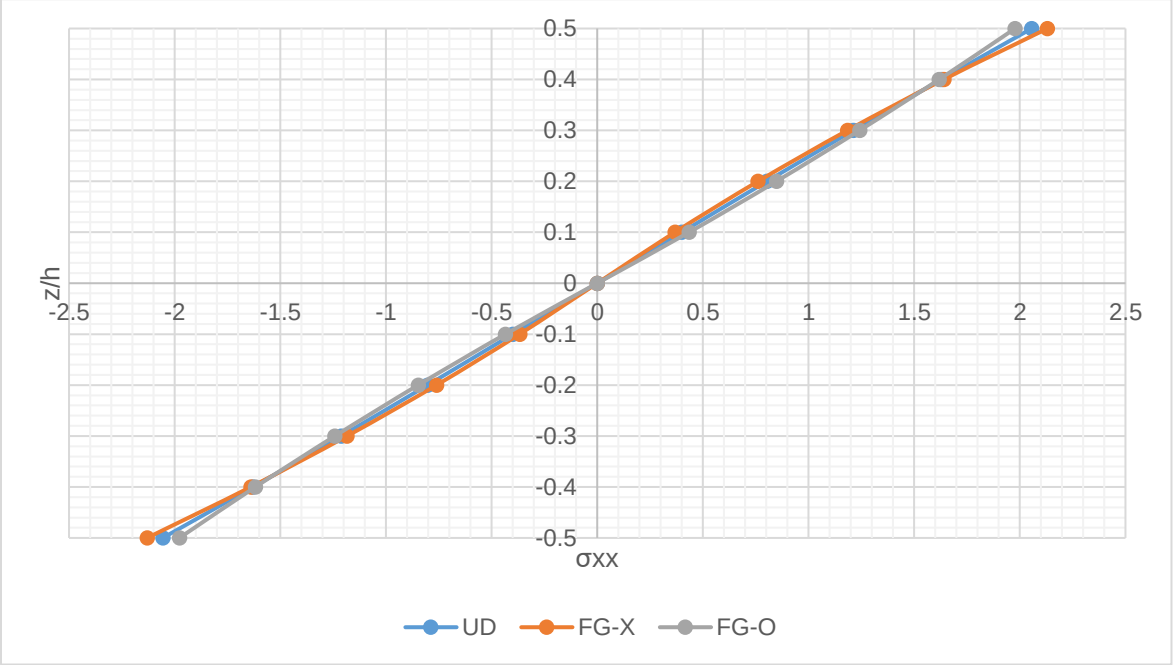

Figure 46: Variation of Dimensionless axial stress through the plate thickness for different patterns.

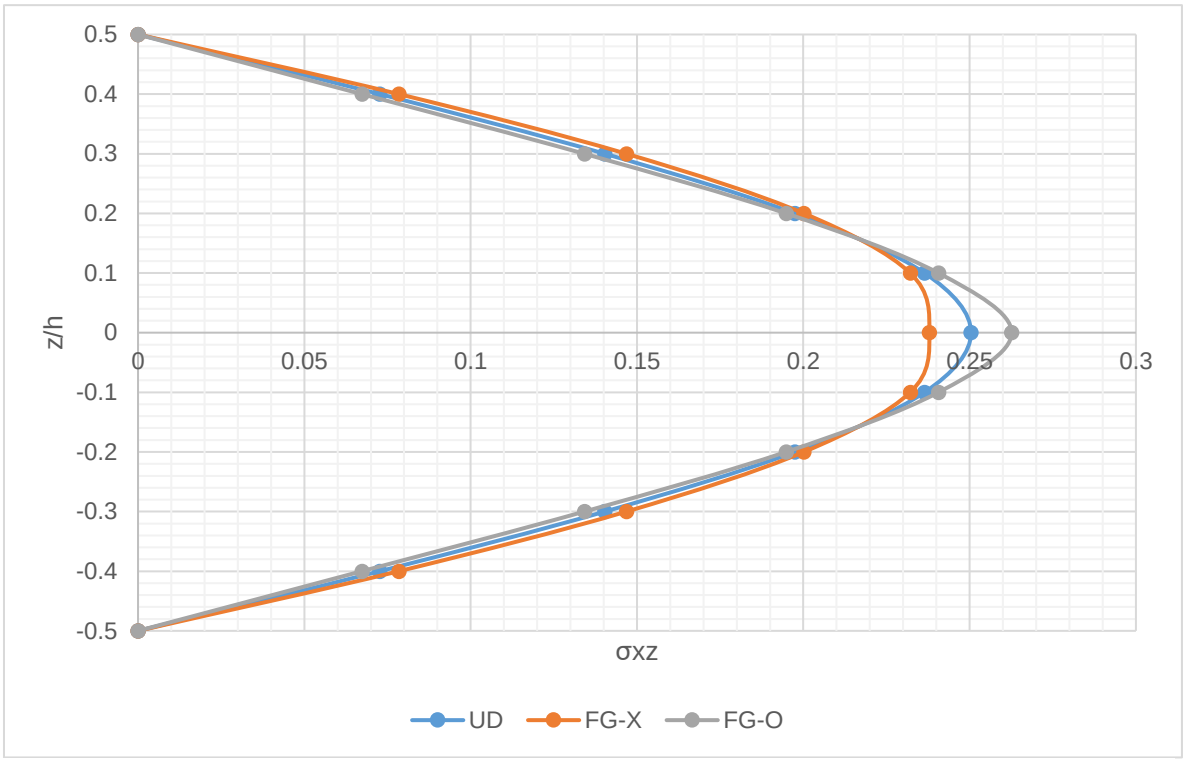

Figure 47: Variation of Dimensionless transverse shear stress through the plate thickness for different patterns.

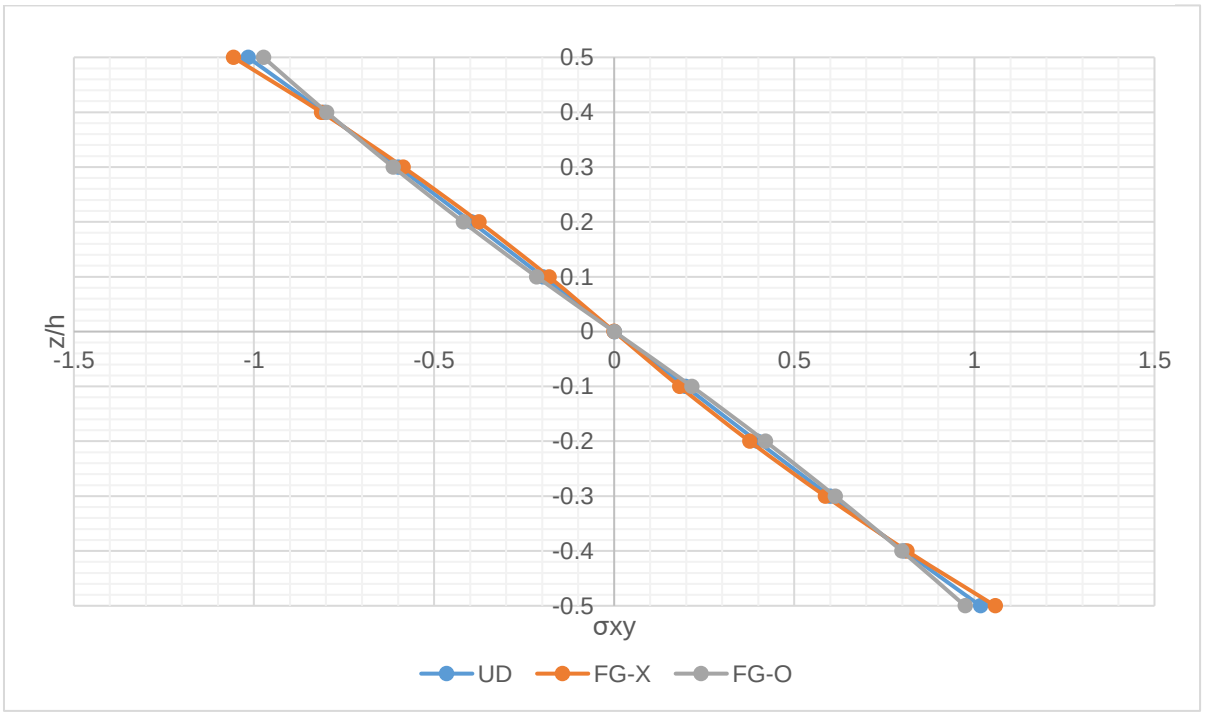

Figure 48: Variation of Dimensionless shear stress through the plate thickness for different patterns.

The figures illustrate the variations of different dimensionless parameters. It is observed that the X pattern represents higher values near the two surfaces of the plate, while the O pattern represents higher values near the mid-plane. The UD pattern consistently describes the average values. Additionally, the figures simulate the parabolic variation of the transverse shear stress as mentioned in the literature.

2.4.2 Parametric study:

In this section, we investigate the impact of the Agpl mass fraction and the plate geometry (variations in the a/h ratio) on the bending behavior of a simply supported functionally graded reinforced graphene nanoplatelets composite plate under a sinusoidal transverse load. We will present several figures depicting the variation of transverse central displacement and plate stresses for a square plate with different values of the a/h ratio (10, 20, 30, 40, 50, 60, 80, 100), as well as for three distribution patterns (UD, FG-X, FG-O) and three increasing values of Agpl mass fraction (0.01, 0.015, 0.02). This analysis aims to assess how these factors influence the bending characteristics of the composite plate.

The dimensionless central deflection (**Figures 49-50-51**) increases as the a/h ratio increases. This is because the plate becomes slenderer and hence more flexible. It is also noted that the dimensionless deflection increases slowly when the ratio values are between 10 and 40, but after passing 40, the deflection increases rapidly. The effect of mass fraction on the deflection is clearly notable in the figures for the different distribution patterns. As the mass fraction increases, the deflection decreases, indicating that the FG-GPLRC plate becomes stiffer. Overall, the FG-X pattern shows a stiffer pattern than FG-O and UD patterns, with lower values of dimensionless deflection for the three values of mass fraction. The FG-O pattern shows a less stiff pattern, with the highest values of dimensionless deflection.

The dimensionless longitudinal stress (illustrated in **Figures 52 to 56**) decreases as the a/h ratio increases. This is because the plate becomes thinner and less rigid. The axial stress decreases rapidly when the ratio values are between 10 and 20, and then the rate of decrease becomes lower after surpassing 20. When mass fraction values are added for the UD and FG-O patterns, the longitudinal stress remains lower. Conversely, in the FG-X patterns, higher mass fractions result in higher axial stress. Notably, the FG-O pattern consistently shows lower values of dimensionless longitudinal stress compared to other distributions.

The dimensionless transverse shear stress (**Figures 57 to 63**) reveals that the UD pattern maintains a consistent value across all mass fraction quantities, whereas the other distribution

patterns show consistent variation but with different magnitudes for each mass fraction. The transverse shear stress increases rapidly from 10 to 20, then stabilizes as the plate becomes thinner, indicating increased flexibility. However, this variation is not consistent across different GPL concentrations. In the FG-X distribution, a higher mass fraction results in lower transverse shear stress, while in the FG-O pattern, a higher (Agpl) concentration leads to higher shear stress compared to the FG-X and UD patterns. Notably, the FG-O pattern shows the highest values of dimensionless shear stress among the three patterns, while the FG-X pattern exhibits the lowest.

The dimensionless shear stress decreases for all distribution types as the (a/h) ratio increases, due to the effect of the slenderness of the plate. Reinforcement, or the increase in (Agpl), raises the shear stress values in the UD and FG-X patterns, whereas in the FG-O distribution, it results in lower shear stress values for the highest mass fraction. The dimensionless shear stress variation exhibits a similar graphic shape across the different patterns. Overall, the FG-O pattern has the highest values of dimensionless shear stress, followed by the UD pattern and then the FG-X pattern.

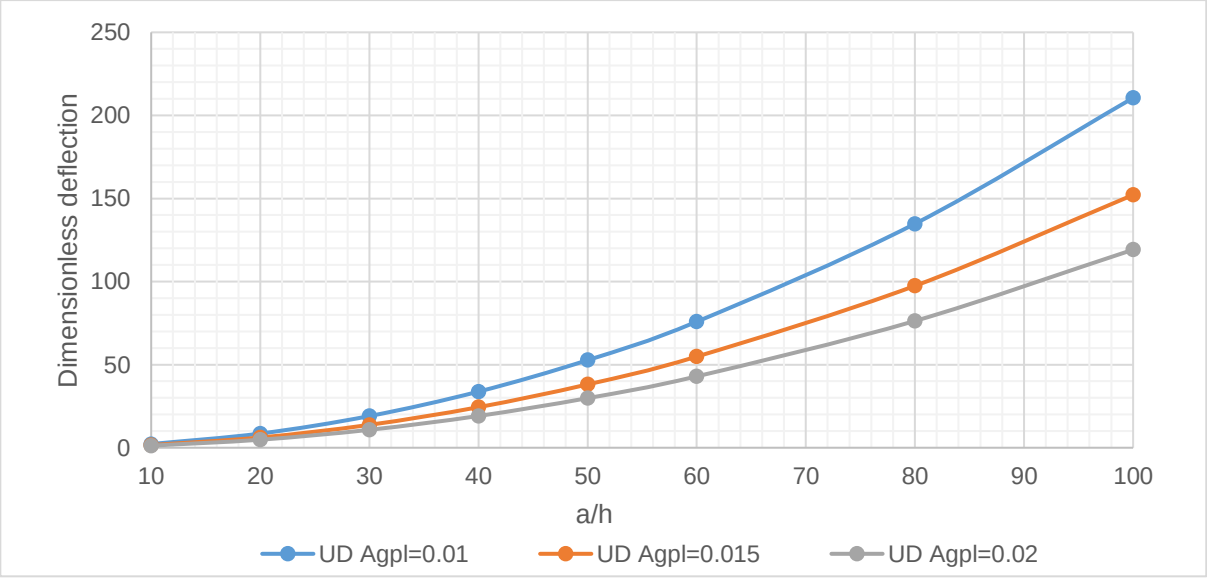

Figure 49: Variation of the central dimensionless deflection according to the a/h ratio of a square plate with different values of Agpl for UD pattern.

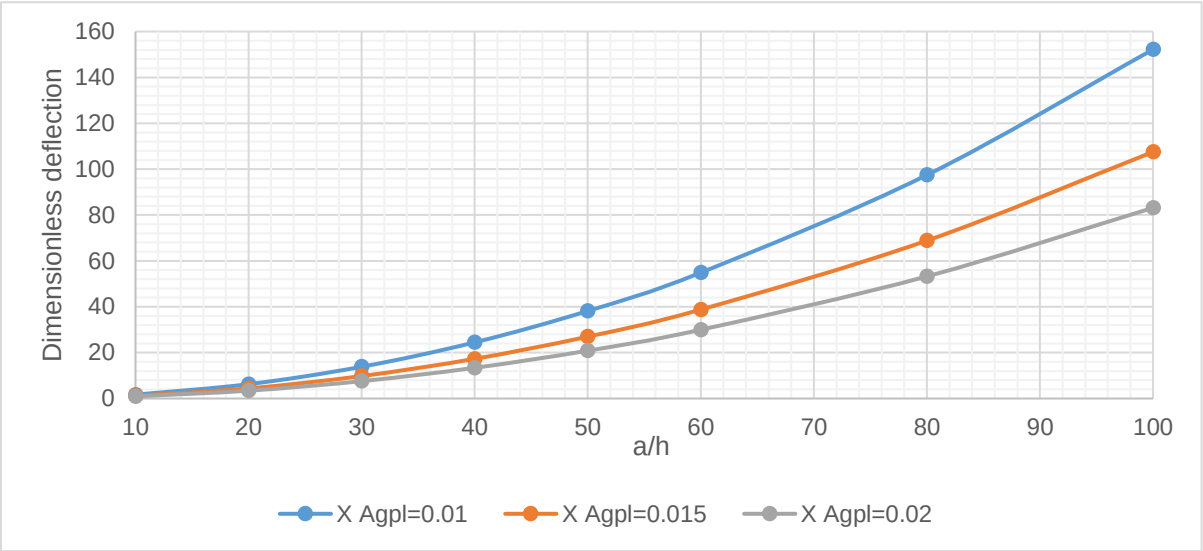

Figure 50: Variation of the central dimensionless deflection according to the a/h ratio of a square plate with different values of Agpl for X pattern.

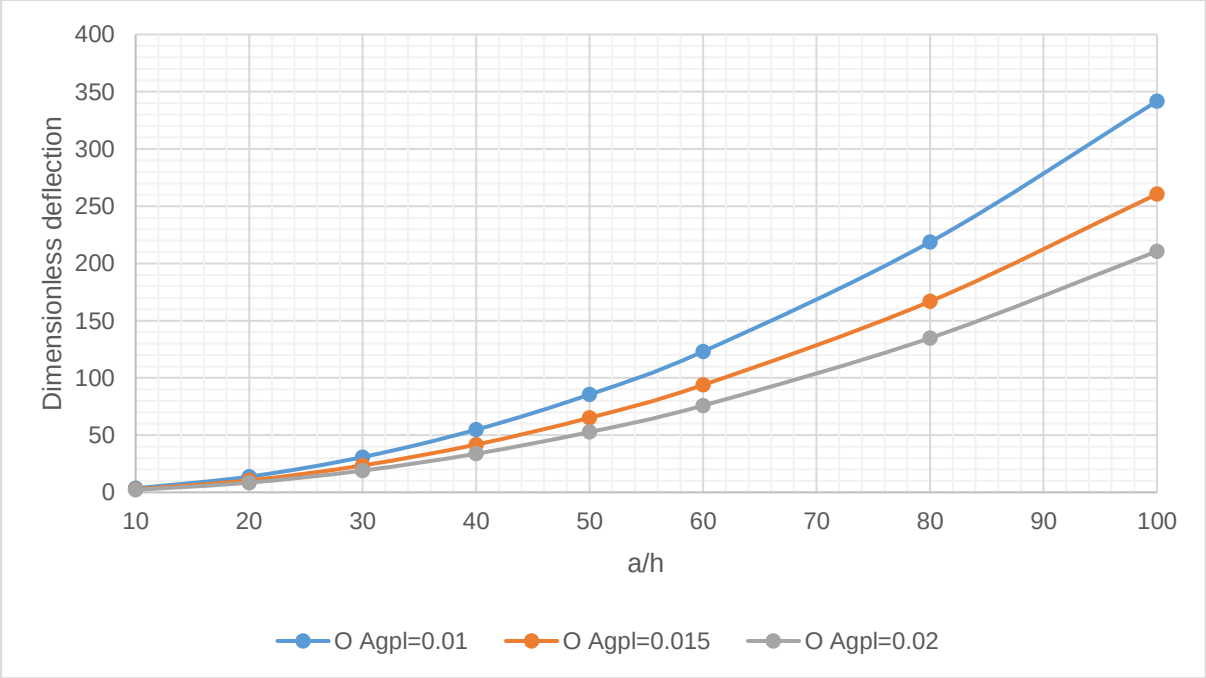

Figure 51: Variation of the central dimensionless deflection according to the a/h ratio of a square plate with different values of Agpl for O pattern.

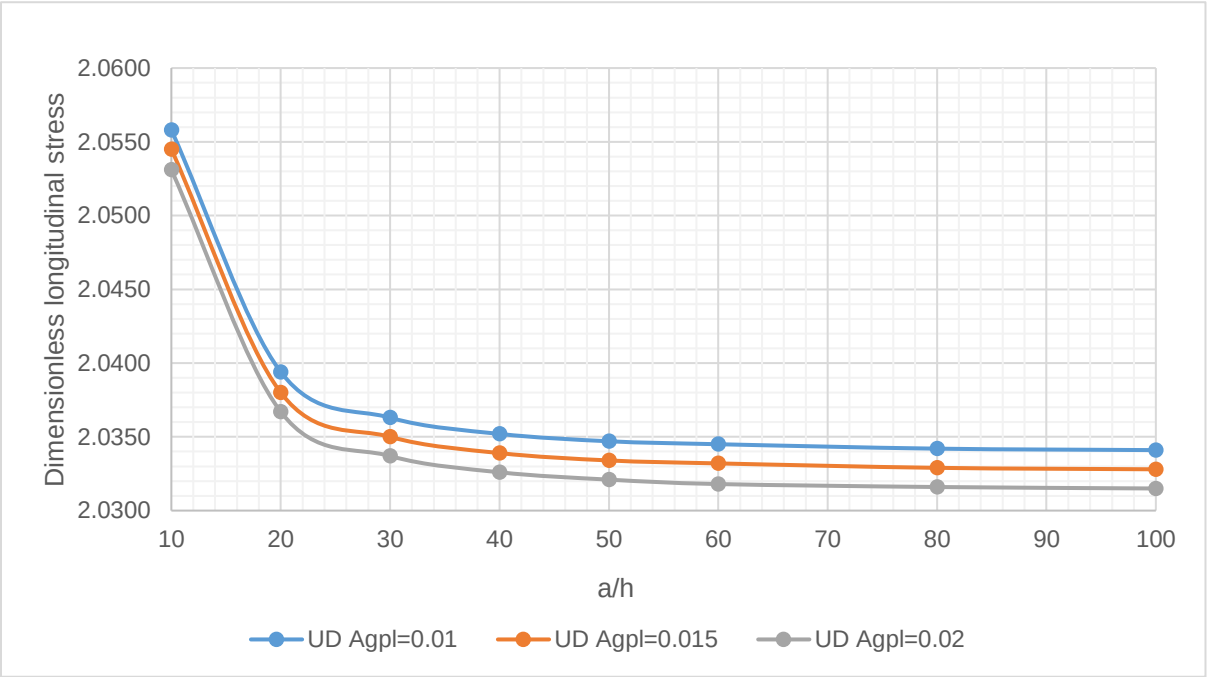

Figure 52: Variation of dimensionless longitudinal stress according to the a/h ratio of a square plate with different values of Agpl for UD pattern.

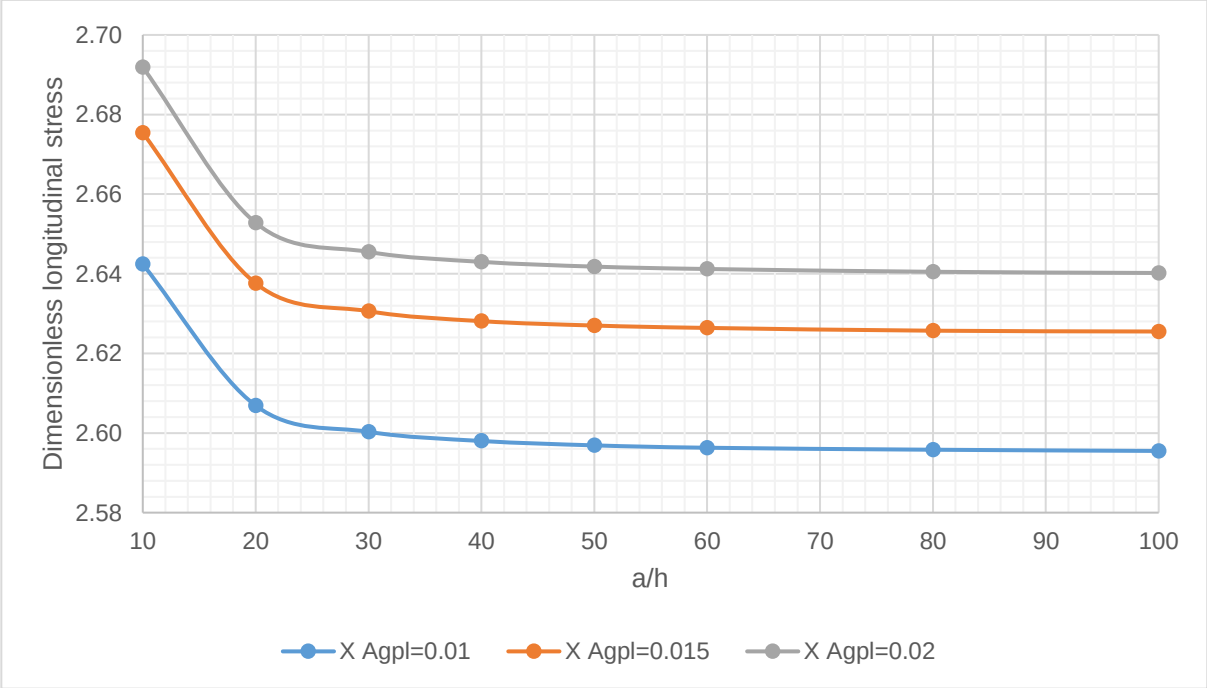

Figure 53: Variation of dimensionless longitudinal stress according to the a/h ratio of a square plate with different values of Agpl for X pattern.

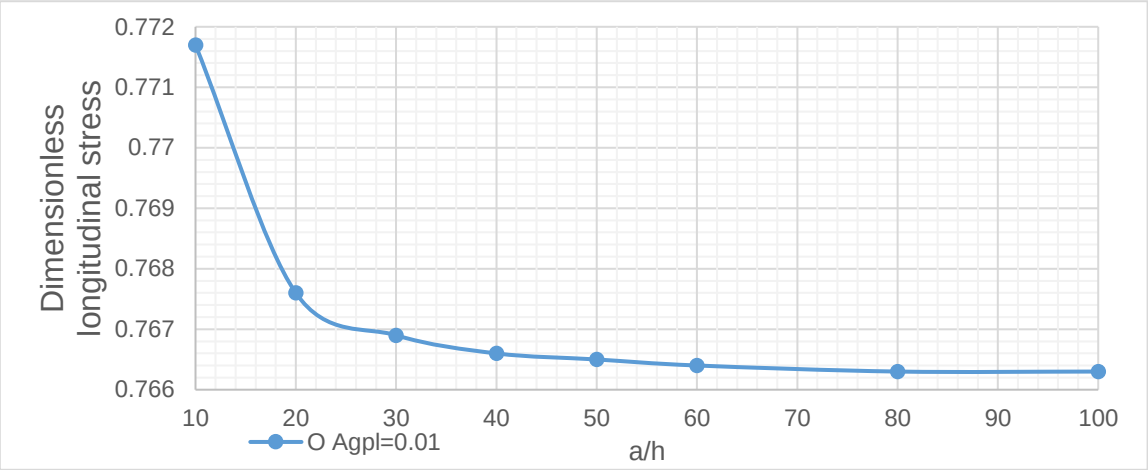

Figure 54: Variation of dimensionless longitudinal stress according to the a/h ratio of a square plate for O pattern Agpl=0.01.

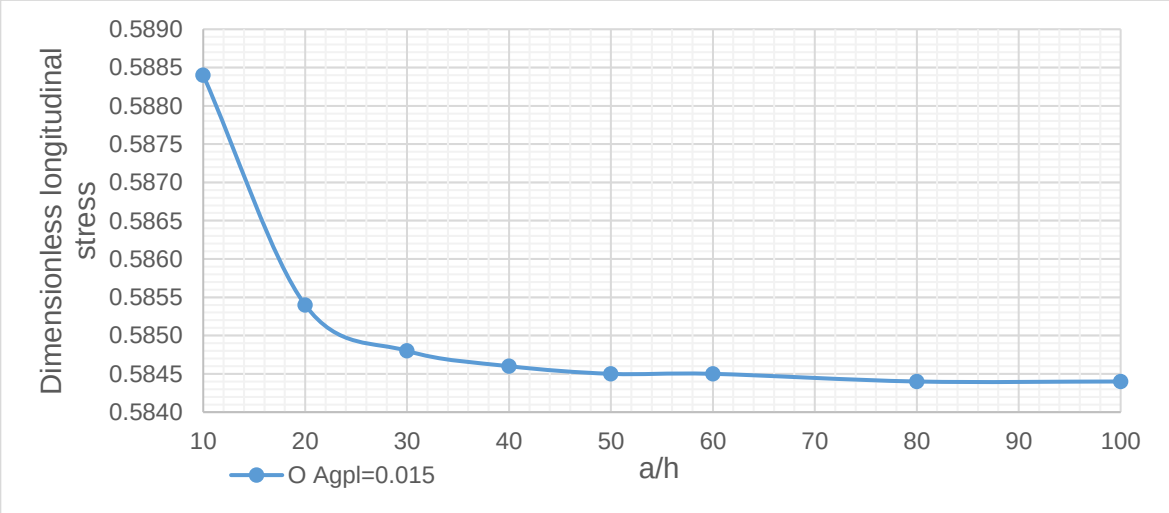

Figure 55: Variation of dimensionless longitudinal stress according to the a/h ratio of a square plate for O pattern Agpl=0.015.

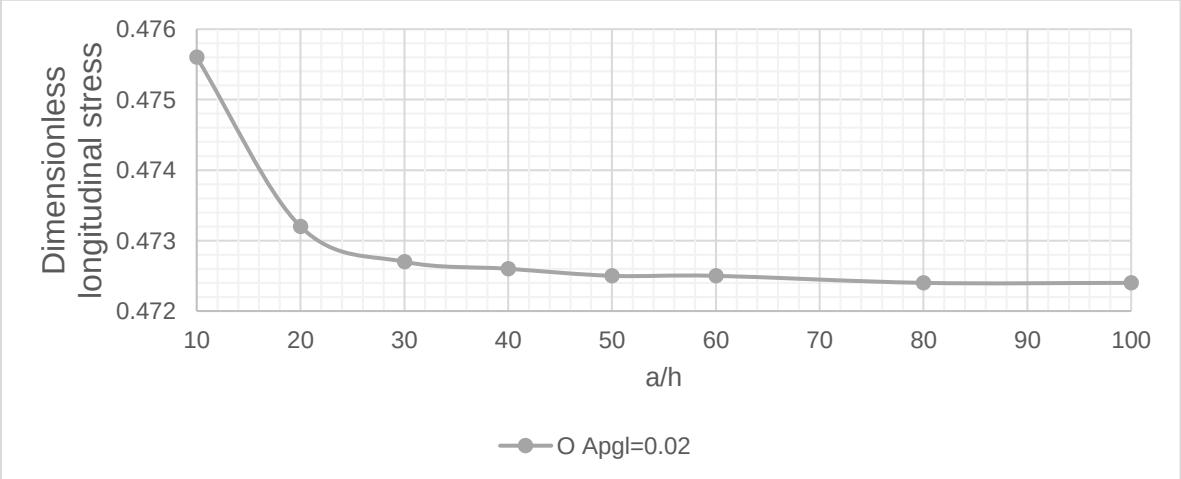

Figure 56: Variation of dimensionless longitudinal stress according to the a/h ratio of a square plate for O pattern Agpl=0.02.

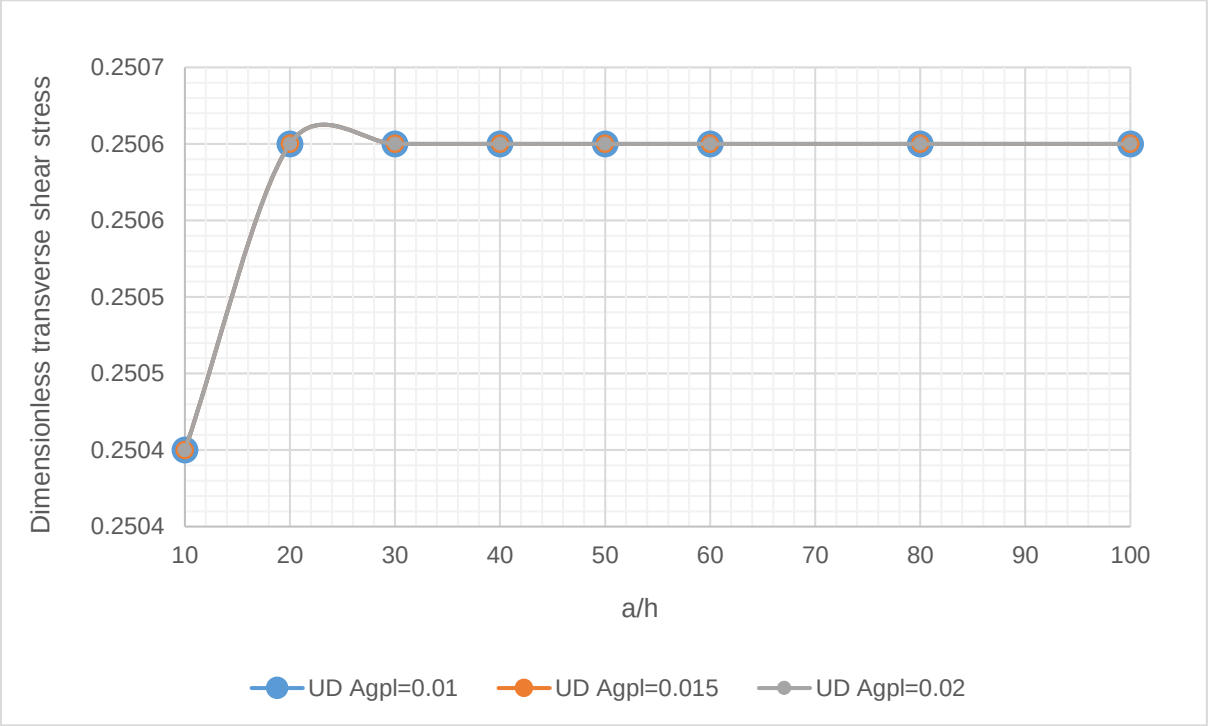

Figure 57: Variation of dimensionless transverse shear stress according to the a/h ratio of a square plate with different values of Agpl for UD pattern.

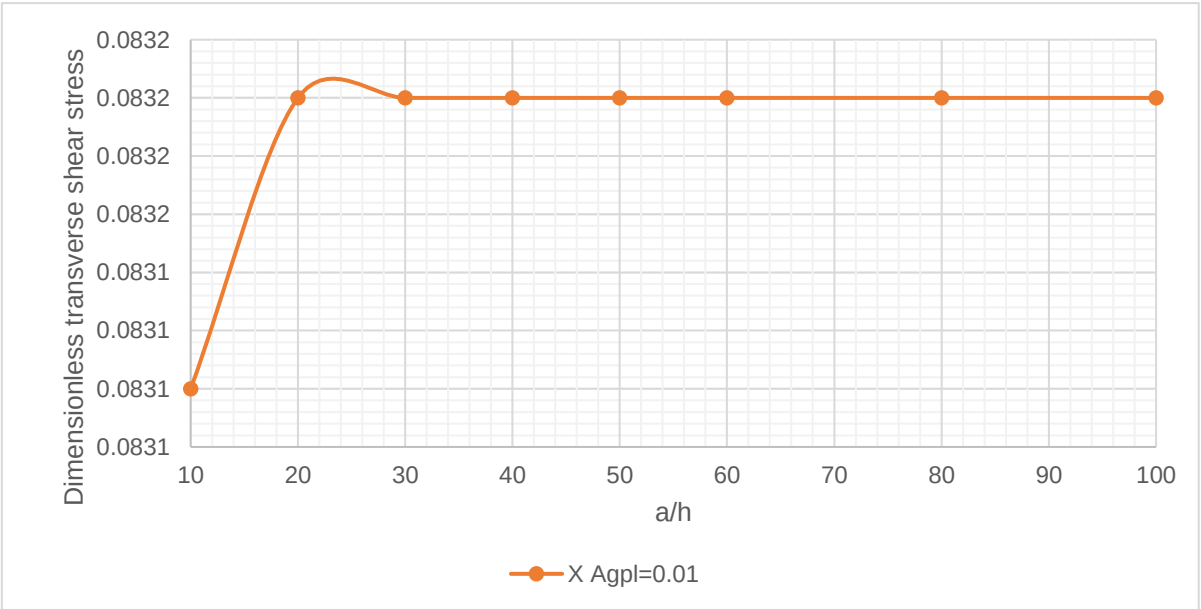

Figure 58: Variation of dimensionless transverse shear stress according to the a/h ratio of a square plate for X pattern Agpl=0.01.

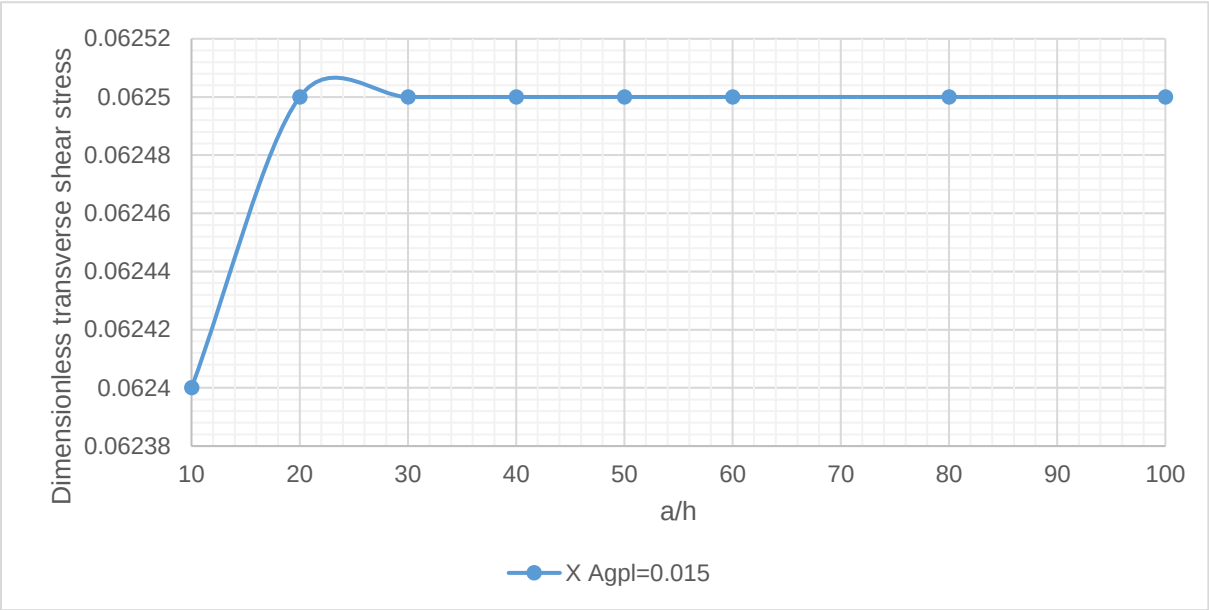

Figure 59: Variation of dimensionless transverse shear stress according to the a/h ratio of a square plate for X pattern Agpl=0.015.

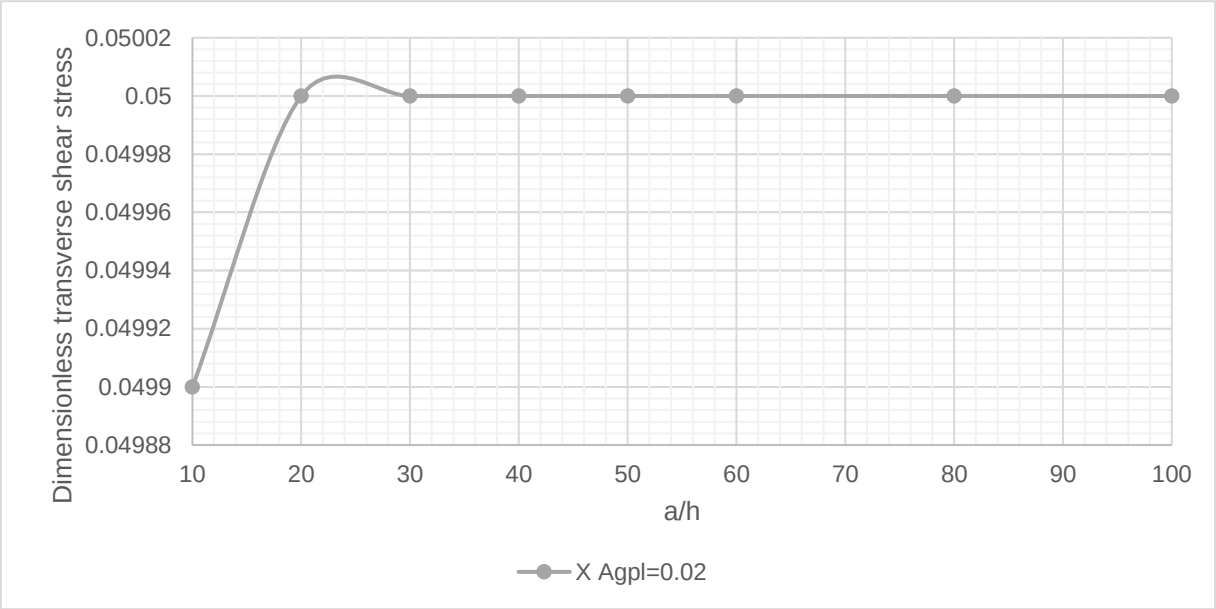

Figure 60: Variation of dimensionless transverse shear stress according to the a/h ratio of a square plate for X pattern Agpl=0.02.

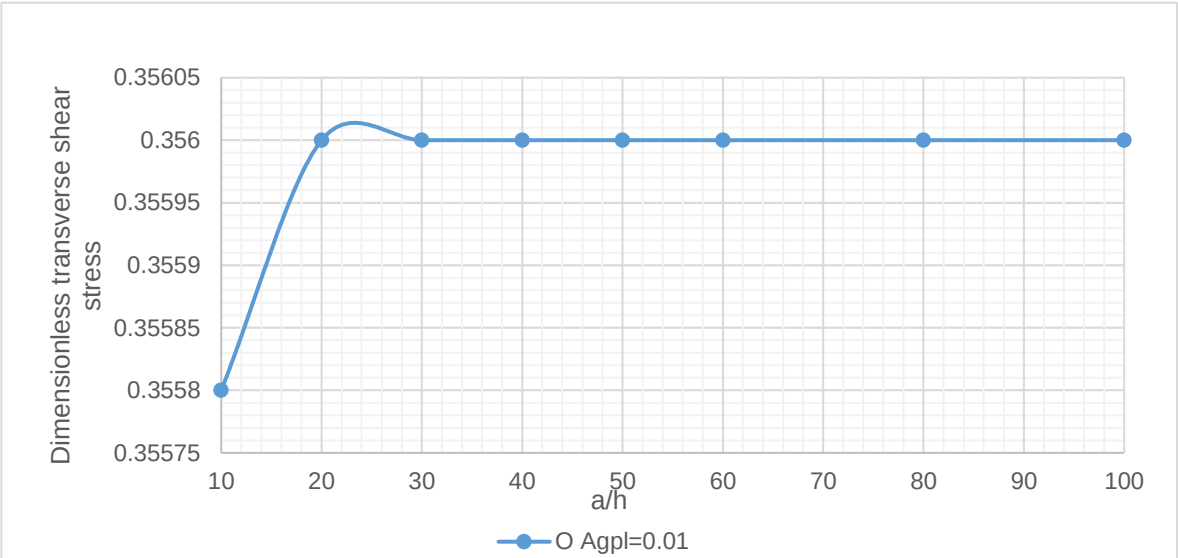

Figure 61: Variation of dimensionless transverse shear stress according to the a/h ratio of a square plate for O pattern Agpl=0.01.

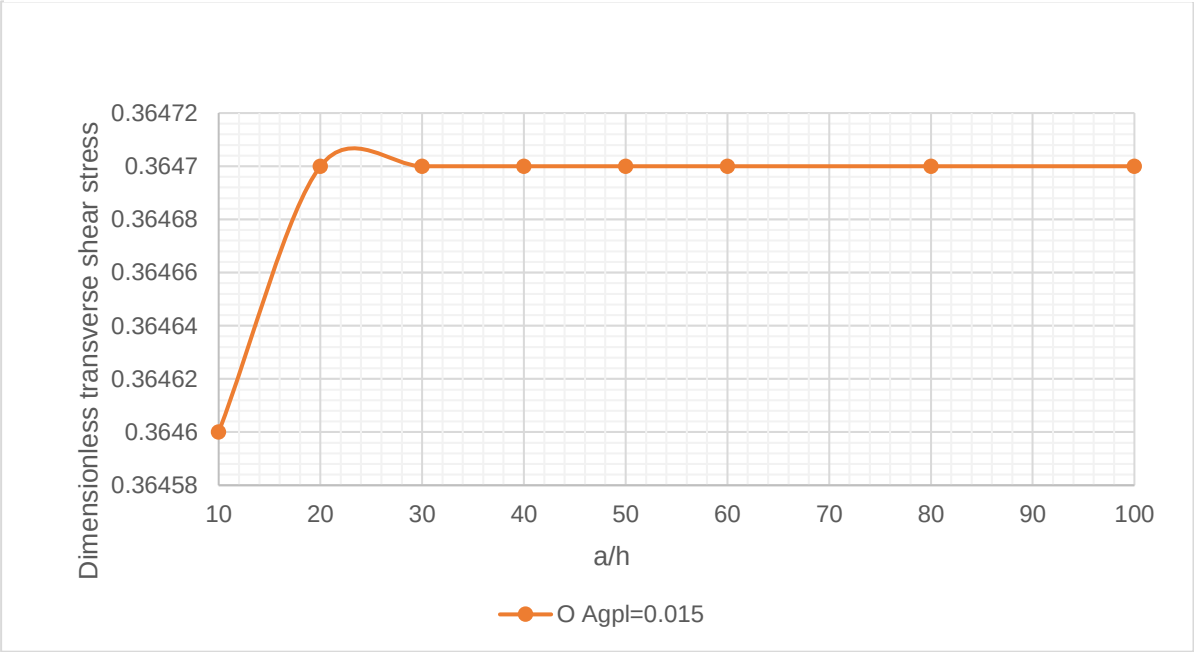

Figure 62: Variation of dimensionless transverse shear stress according to the a/h ratio of a square plate for O pattern Agpl=0.015.

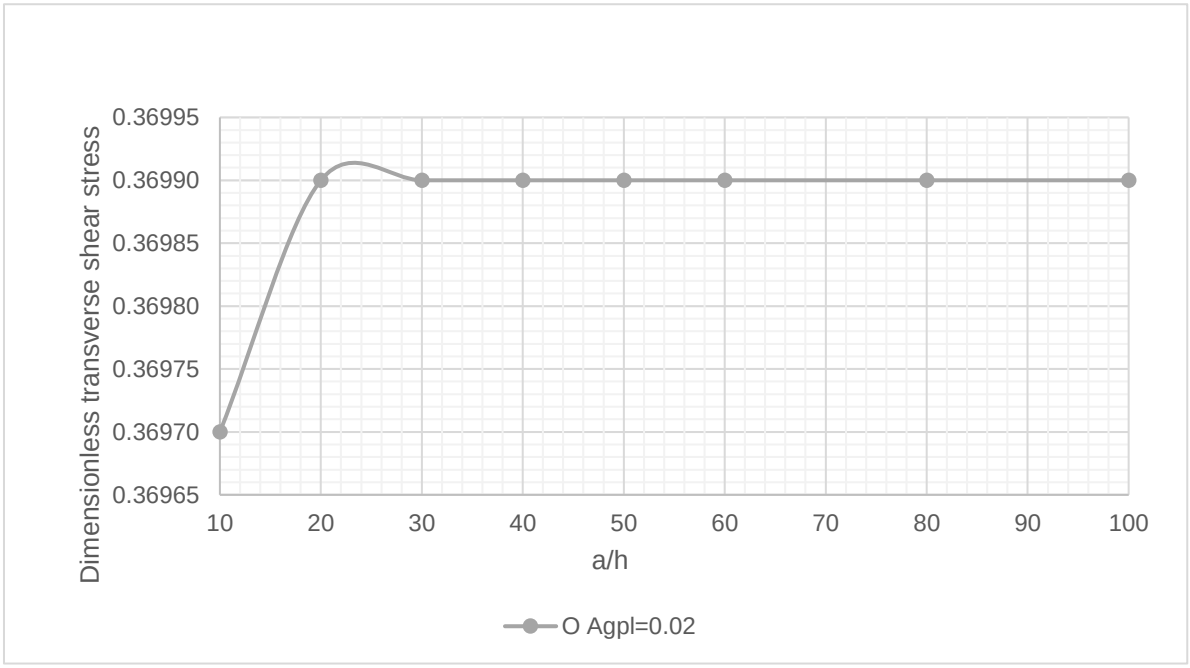

Figure 63: Variation of dimensionless transverse shear stress according to the a/h ratio of a square plate for O pattern Agpl=0.02.

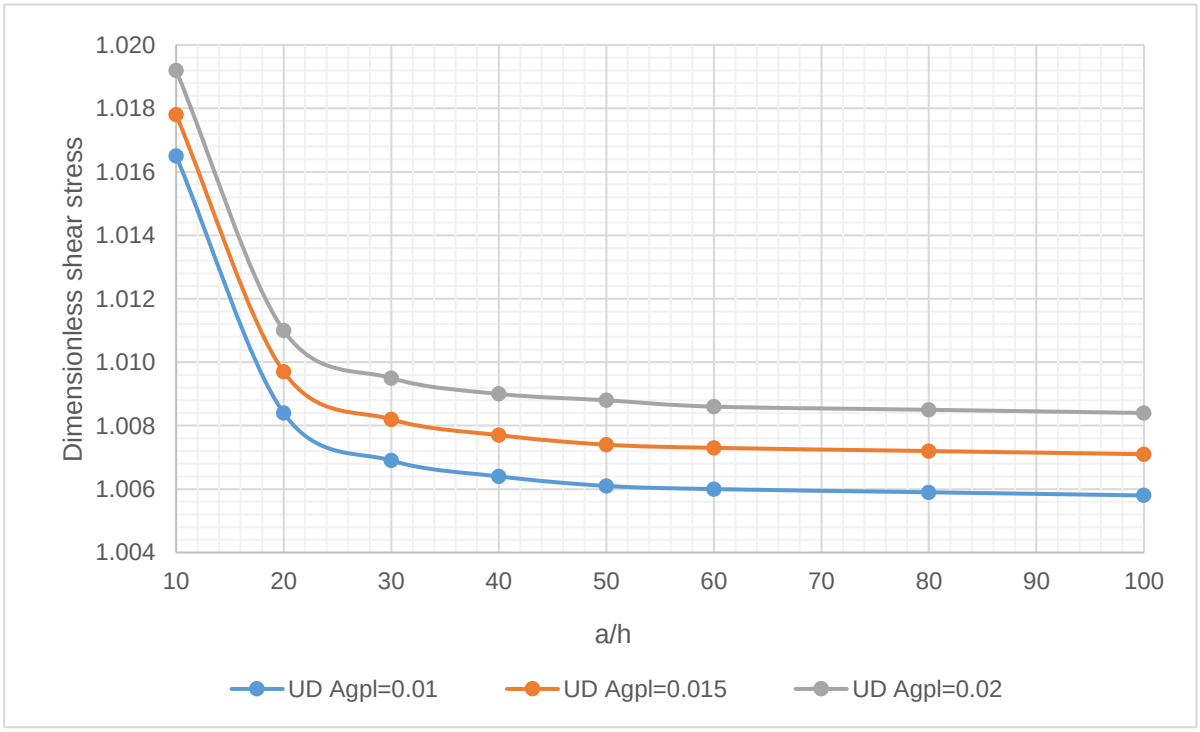

Figure 64: Variation of dimensionless shear stress according to the a/h ratio of a square plate with different values of Agpl for UD pattern.

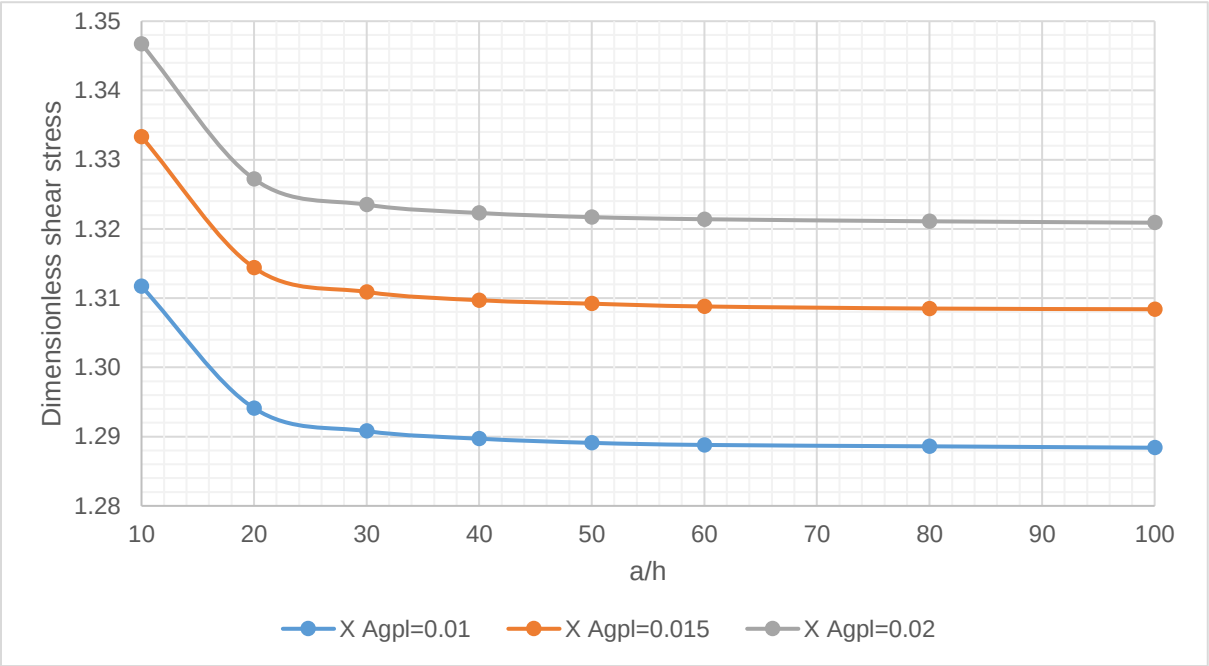

Figure 65: Variation of dimensionless shear stress according to the a/h ratio of a square plate with different values of Agpl for X pattern.

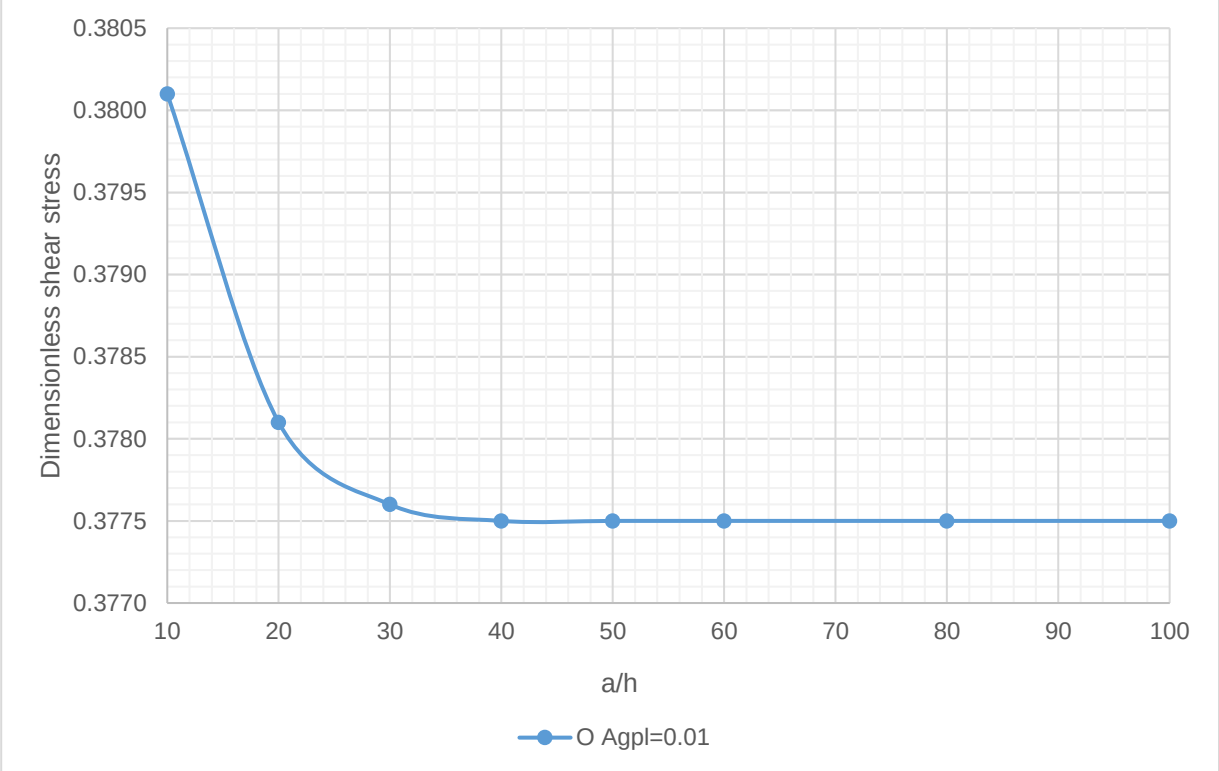

Figure 66: Variation of dimensionless shear stress according to the a/h ratio of a square plate for O pattern Agpl=0.01.

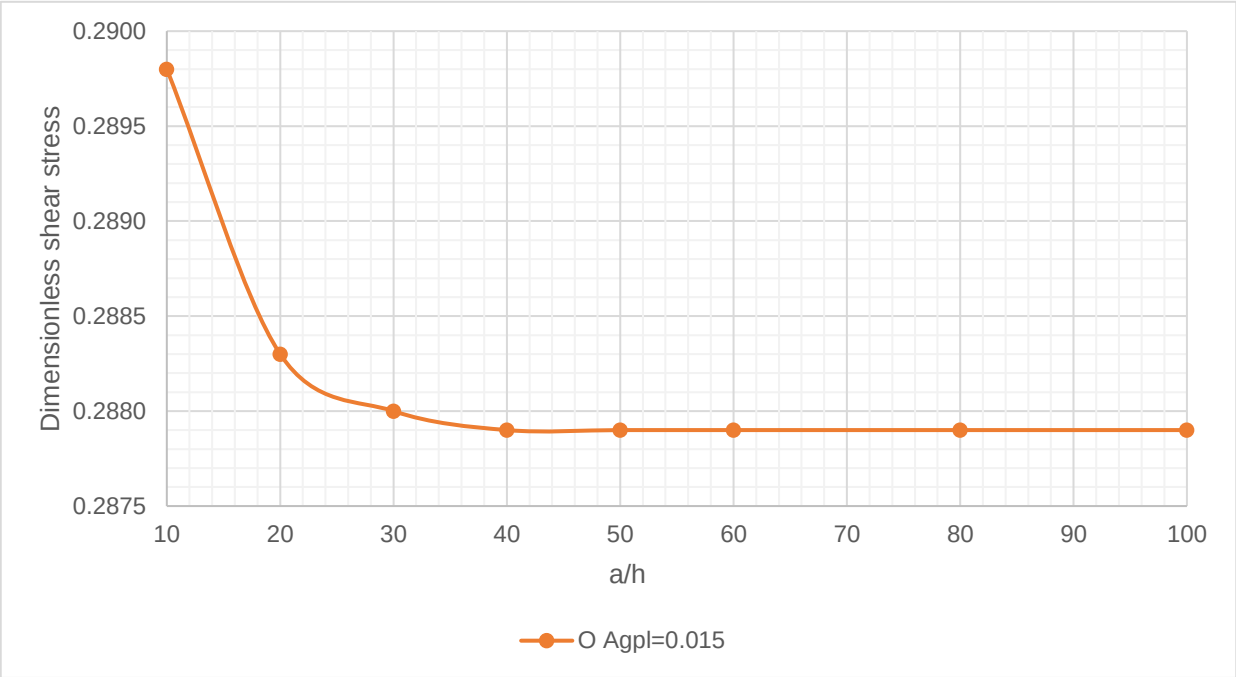

Figure 67: Variation of dimensionless shear stress according to the a/h ratio of a square plate for O pattern Agpl=0.015.

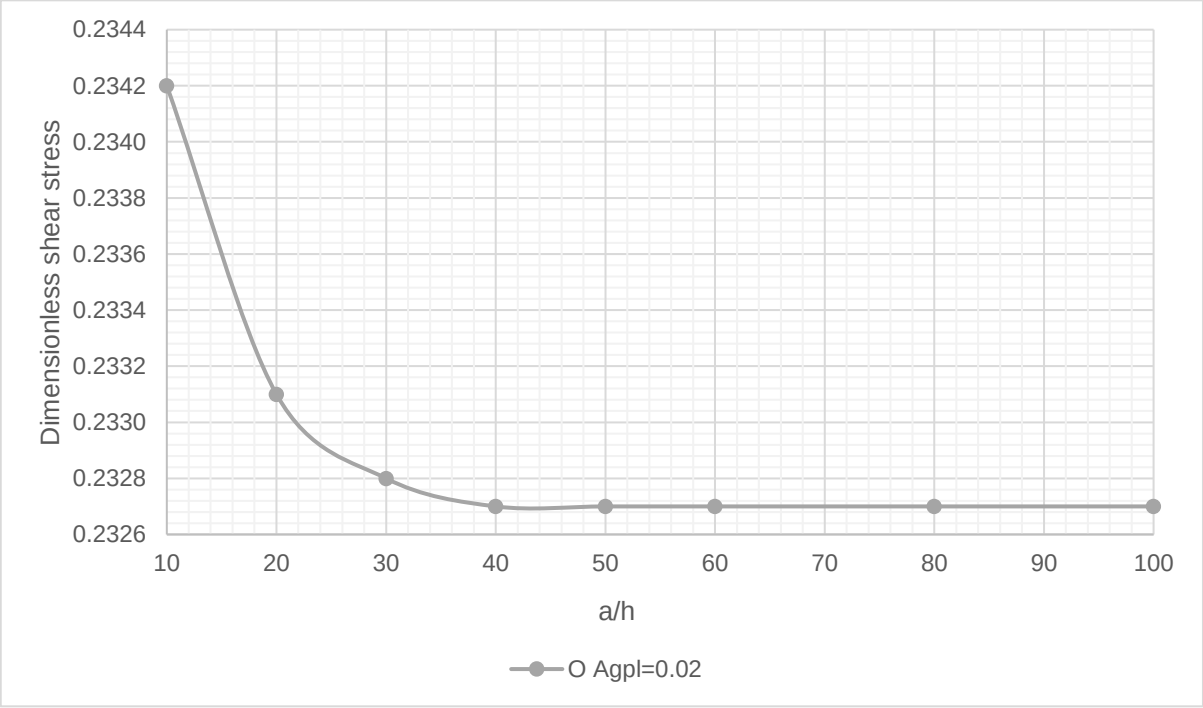

Figure 68: Variation of dimensionless shear stress according to the a/h ratio of a square plate for O pattern Agpl=0.02.

2.5 Flowchart of the principal coding steps:

Python programming language is used to solve the bending and buckling motion equations of a simply supported FG-GPLRC plate using the Navier method. The main steps involved in this process are summarized in the flowchart

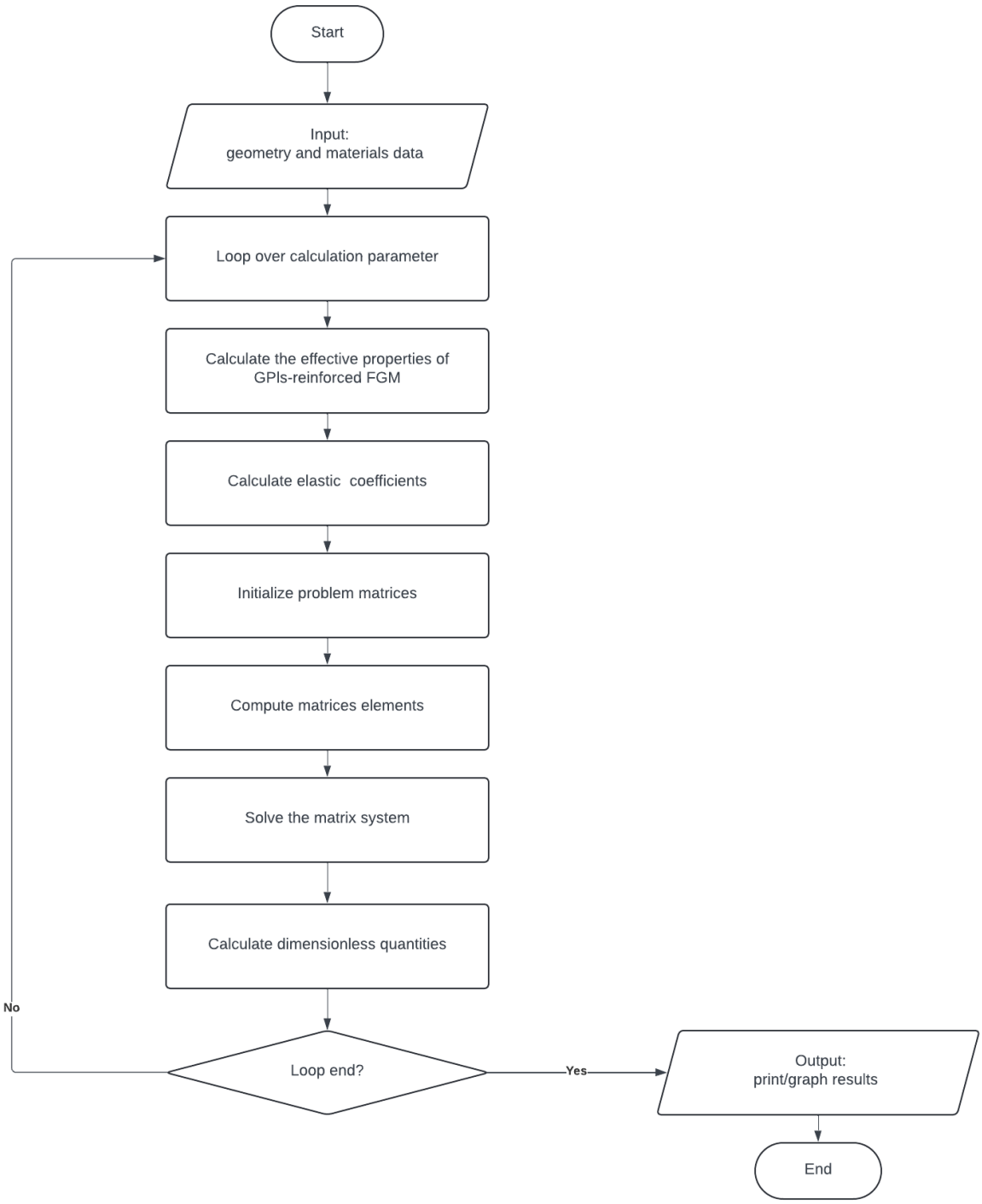

Figure 69: Python code flowchart.

3. Conclusion:

In this chapter, we focused on studying the bending and buckling behavior of different types of FG-GPLRC plates (Functionally Graded Graphene nano-Platelets reinforced composite) using the analytical method of Naiver. We estimated the mechanical properties based on the z position through the thickness using the extended mixing rule. Our approach involved using the higher-order shear deformation theory to approximate the two-dimensional displacement field. We validated our Python calculation code by comparing our results with published data and found good agreement. It's worth noting that our calculation code requires a smaller calculation volume compared to other methods such as the theory of 3D elasticity, the DQM method, or the finite element method. However, it's important to mention that our analytical method is only valid for simple supported plates.

We also highlighted the promising potential of GPLs in the industry as they serve as excellent candidates for reinforcing polymer composites and controlling buckling critical loads, displacements, and stresses. Their superior mechanical properties, including high strength and rigidity, make them advantageous for various applications.

GENERAL CONCLUSION:

The development of composite materials has brought about significant advantages, but it has also introduced challenges related to discontinuity of material properties at the interfaces. These discontinuities can lead to stress concentrations and interface problems, particularly in high temperature environments. Furthermore, the large plastic deformation of the interface can initiate and propagate cracks, ultimately leading to failure of the composite. To address these issues, Functionally Graded Materials (FGMs) have emerged as a promising solution.

FGMs are advanced composites with varying composition, microstructure, and properties, typically in the thickness direction. They offer a wide range of practical applications and represent a rapidly evolving field in science and engineering. However, the design and development of FGMs require specialized analysis tools tailored to their geometric and material specificities.

In this thesis, the focus is on studying the bending behaviors and buckling of an FGM plate reinforced by graphene nano-platelets. The analysis is based on the hyperbolic higher order shear deformation theory, with the assumption that the properties of the materials vary through the thickness. The plate is modeled as a multilayer plate, and the equations of motion for a simply supported plate are established using Hamilton's principle, which is based on the strain energy and the work of external loads.

The solution of the coupled differential equations is obtained using the analytical method of Navier to determine the stresses, displacements, and the critical load of buckling. A parametric study has been conducted to obtain numerous numerical results, which are presented in graphical form for better interpretation. These results have led to several important conclusions.

Overall, the study underscores the potential benefits of FGMs and highlights the need for continued research and development in this area. By addressing the challenges associated with conventional composite materials, FGMs offer the promise of enhanced performance and expanded application possibilities. Thanks to these results, several conclusions can be drawn:

- The reinforcement of composite plates with graphene nanoplatelets significantly affects deflection, stresses, and critical buckling loads.
- The impact of the volume fraction of graphene nanoplatelets on the displacements and stresses of moderately thick plates is more pronounced.
- We also observe general trends regarding the influence of the geometry of the FGM plate on its static behavior. Specifically, as the plate becomes relatively thinner (length-to-thickness ratio or width-to-thickness ratio), the deflection (w) increases. Additionally, as the (a/h) ratio (from moderately thick plate to thin plate) increases, the values of longitudinal and shear stresses decrease, whereas transverse shear stresses increase.
- The stresses and displacements of the plate are strongly influenced by the volume fraction of graphene nanoplatelets used as reinforcement. Indeed, as the volume fraction increases, the plate becomes more rigid and its deformation decreases. This observation holds true for moderately thick, thin, and even thick plates. However, the most influential parameter is the concentration of GPLs far from the mid-plane (surface-rich). Therefore, the distribution law of the volume fraction affects the stresses and the critical buckling load regardless of the plate's geometry. This effect diminishes as the plate becomes much thinner, where the concentration of GPLs near the upper and lower surfaces has a reduced impact.

Perspectives:

- Incorporating the Effect of Temperature: A valuable future direction would be to extend the study by considering the influence of temperature on the bending and stability of FGM plates reinforced with graphene nanoparticles. This approach would account for thermal expansion and variations in mechanical properties with temperature.

- Evaluating other Nanomaterials: Beyond graphene nanoparticles, it would be beneficial to evaluate other types of nanomaterials as reinforcements for FGM plates. This perspective would allow for a comparison of the effects of different nanomaterials, such as carbon nanotubes, nanofibers, and metal nanoparticles, on

the static and stability responses of the plates, aiming for optimal reinforcement design for specific applications.

- Exploring Different Boundary Conditions: Investigating the effect of various boundary conditions (clamped, free, simply supported, and their combinations) on the critical buckling load, stresses, and displacements for different types of GPLRC plates and beams.

- Examining Initial Defects: Studying the impact of initial defects (such as porosities and deformed surfaces) on the performance of the plates.

BIBLIOGRAPHY

[1] WEB SITE: https://www.history.com/topics/pre-history/stone-age.

[2] Britannica, The Editors of Encyclopaedia. "Bronze Age". *Encyclopedia Britannica*, 8 Feb. 2024, https://www.britannica.com/event/Bronze-Age.

[3] Valmik Bhavar et al 2017 IOP Conf. Ser.: Mater. Sci. Eng. 229 012021.

[4] Ning Zhang, Tahir Khan, Haomin Guo, Shaoshuai Shi, Wei Zhong, Weiwei Zhang, "Functionally Graded Materials: An Overview of Stability, Buckling, and Free Vibration Analysis", Advances in Materials Science and Engineering, vol. 2019, Article ID 1354150, 18 pages, 2019.

[5] El-Galy, Islam & Saleh, Bassiouny & Ahmed, Mahmoud. Functionally graded materials classifications and development trends from industrial point of view. SN Applied Sciences, 2019.

[6] Mahamood, RM, Akinlabi, ET, Shukla, M & Pityana, S 2012, Functionally graded material: An overview. in AM Korsunsky, L Gelman, A Hunter, SI Ao & DWL Hukins (eds), Proceedings of the World Congress on Engineering, 2012.

[7] Moussaoui sara ines, Etude de l'influence du renforcement en nano-plaquettes de graphène sur les fréquences de vibration libre d'une plaque FGM, université saad dahleb, blida.

[8] Lalitha A. Kolahalam, I.V. Kasi Viswanath, Bhagavathula S. Diwakar, B. Govindh, Venu Reddy, Y.L.N. Murthy,Review on nanomaterials: Synthesis and applications,
Materials Today: Proceedings,Volume 18, Part 6, 2019.

[9] WEB SITE: https://nanografi.com/blog/graphene-nanoplatelets-properties-and-applications/

[10] Cataldi P, Athanassiou A, Bayer IS. Graphene Nanoplatelets-Based Advanced Materials and Recent Progress in Sustainable Applications. Applied Sciences. 2018.

[11] Jiménez-Suárez, A. & Prolongo, S.G. Graphene Nanoplatelets. Applied Sciences. 2020.

[12] WEB SITE: https://www.graphene-info.com/graphene-structure-and-shape.

[13] WEB SITE: https://matmatch.com/learn/material/graphene.

[14] Urade, A.R., Lahiri, I. & Suresh, K.S. Graphene Properties, Synthesis and Applications: A Review. JOM 75, 614–630, 2023.

[15] WEB SITE: https://nanografi.com/blog/graphene-nanoplatelets-properties-and-applications/

[16] Peng C, Zhang X. Chemical Functionalization of Graphene Nanoplatelets with Hydroxyl, Amino, and Carboxylic Terminal Groups. Chemistry. 2021.

[17] Pham, Phuong. 21st Century Nanostructured Materials - Physics, Chemistry, Classification, and Emerging Applications in Industry, Biomedicine, and Agriculture, 2022.

[18] Hirlekar, Rajashree S., Manohar Yamagar, Harshal Garse, Mohit Vij, Vilasrao J. Kadam and Bharati Vidyapeeth. "CARBON NANOTUBES AND ITS APPLICATIONS: A REVIEW." 2009.

[19] WEB SITE: https://en.wikipedia.org/wiki/Nanomaterials.

[20] Anu Mary Ealia, S, Saravanakumar, M P, A review on the classification, characterisation, synthesis of nanoparticles and their application, IOP Conference Series: Materials Science and Engineering, 2017.

[21] Boggarapu, V., Gujjala, R., Ojha, S., Acharya, S., babu P, V., Chowdary, S., kumar Gara, D., State of the art in functionally graded materials, Composite Structures, 2021.

[22] Amale MAHI, ANALYSE ET ETUDE DES PLAQUES COMPOSITES FGM EN VIBRATIONS LIBRES, Faculté des Sciences de l'Ingénieur Département de Mécanique, UNIVERSITE SAAD DAHLAB DE BLIDA.

[23] Shaoyu Zhao, Zhan Zhao, Zhicheng Yang, LiaoLiang Ke, Sritawat Kitipornchai, Jie Yang, Functionally graded graphene reinforced composite structures: A review, Engineering Structures, 2020.

[24] ADIM Belkacem, THESE DE DOCTORAT LMD « Etude de la stabilité des plaques en matériaux composites : analyse et modélisation », Faculté des Sciences Appliquées Département de Génie mécanique, Université Ibn Khaldoun-Tiaret.

[25] Elishakoff I. Who developed the so-called Timoshenko beam theory? Mathematics and Mechanics of Solids. 2020.

[26] Cen, Song & Shang, Yan. (2015). Developments of Mindlin-Reissner Plate Elements. Mathematical Problems in Engineering. 2015.

[27] Tauchert, T.R. Energy Method, Anisotropic and Heterogeneous Plates. In: Hetnarski, R.B. (eds) Encyclopedia of Thermal Stresses. Springer, Dordrecht, 2014.

[28] Abualnour, Moussa & Abdelbaki, Chikh & Habib, Hebali & Abdelhakim, Kaci & Tounsi, Abdeldjebbar & Bousahla, Abdelmoumen & Tounsi, Abdelouahed. Thermomechanical analysis of antisymmetric laminated reinforced composite plates using a new four variable trigonometric refined plate theory, 2019.

[29] Jinan Ahmad Mostafa Al Shatnawi, Thesis of M.Sc. in Structural Engineering "FREE VIBRATION OF FUNCTIONALLY GRADED POROUS CRACKED PLATES", The Faculty of Graduate Studies Jordan University of Science and Technology.

[30] A. Mahi et al, A new hyperbolic shear deformation theory for bending and free vibration analysis of isotropic, functionally graded, sandwich and laminated composite plates. / Applied Mathematical Modelling 39, 2015.

[31] J.L. Mantari, A.S. Oktem, C. Guedes Soares, A new trigonometric shear deformation theory for isotropic, laminated composite and sandwich plates, International Journal of Solids and Structures, 2012.

[32] Touratier, An efficient standard plate theory, International Journal of Engineering, 1991.

[33] Ait Atmane, H., Tounsi, A., Mechab, I. et al. Free vibration analysis of functionally graded plates resting on Winkler–Pasternak elastic foundations using a new shear deformation theory. Int J Mech Mater Des, 2010.

[34] El Meiche, N., Tounsi, A., Ziane, N., Mechab, I. and Adda Bedia, E.A. "A new hyperbolic shear deformation theory for buckling and vibration of functionally graded sandwich plate", 2011.

[35] Sahoo R., Singh BN," A new shear deformation theory for the static analysis of laminated composite and sandwich plates", International Journal of Mechanical Sciences, 2013.

[36] Ambartsumyan S.A, Theory of anisotropic plate, Tech Publishing Co,1969.

[37] Shimpi, R.P., "Refined plate theory and its variants", AIAA Journal, 2002.

[38] Abdellah Hassaine and Amale Mahi, Effects of graphene-platelets reinforcement on the free vibration, bending, and buckling of porous functionally graded metal-ceramic plates, 2023.

[39] Bhaskar, K., & Varadan, T. K. Plates theories and their application, 2021.

[40] Ghandourah, E.E., Daikh, A.A., Alhawsawi, A.M., Fallatah, O.A., & Eltaher, M.A. Bending and Buckling of FG-GRNC Laminated Plates via Quasi-3D Nonlocal Strain Gradient Theory. Mathematics. 2022.